UNIVERSITÉ DE MONTRÉAL

DESIGN AND CONSTRUCTION OF A HIGHLY SENSITIVE COIL FOR MRI OF THE
SPINAL CORD

ALEXANDRU FOIAS

INSTITUT DE GÉNIE BIOMÉDICAL

ÉCOLE POLYTECHNIQUE DE MONTRÉAL

UNIVERSITÉ DE MONTRÉAL

ÉCOLE POLYTECHNIQUE DE MONTRÉAL

Ce mémoire intitulé :

DESIGN AND CONSTRUCTION OF A HIGHLY SENSITIVE COIL FOR MRI OF THE
SPINAL CORD

présenté par : FOIAS Alexandru

en vue de l'obtention du diplôme de : Maîtrise ès sciences appliquées

a été dûment accepté par le jury d'examen constitué de :

M. STIKOV Nikola, Ph. D., président

M. COHEN-ADAD Julien, Ph. D., membre et directeur de recherche

M. LAURIN Jean-Jacques, Ph. D., membre et codirecteur de recherche

M. NEAR Jamie, Ph. D., membre

DEDICATION

To my family

ACKNOWLEDGEMENTS

Firstly, I would like to express my sincere gratitude to my advisor Prof. Julien Cohen-Adad and my co-advisor Prof. Jean-Jacques Laurin for their continuous support during my graduate study and related research, for their patience, motivation, and immense knowledge. In addition, I would like to thank Julien Cohen-Adad for giving me the opportunity to join his laboratory and for providing me with an excellent atmosphere for doing research.

Besides my advisors, I would like to thank the rest of my thesis committee: Prof. Nikola Stikov, and Dr. Jamie Near, for their insightful comments and encouragement, which incented me to widen my research from various perspectives.

I thank my fellow hardware labmate Nibardo for the stimulating discussions and guidance throughout my research. Moreover, I would like to thank Sara, Benjamin, Gabriel and Tanguy for providing my constant support and feedback during my project.

Last but not the least, I would like to thank my family: my mother, my sister and to my grandmother for supporting me spiritually throughout writing this thesis and my life in general.

RÉSUMÉ

Un grand nombre de pathologies (sclérose en plaque, lésions, etc.) peuvent toucher la moelle épinière, des techniques non invasives de diagnostic tel que l'imagerie par résonance magnétique (IRM) sont généralement utilisées pour les dépister. Les antennes commerciales pour l'IRM sont conçues pour accommoder une large population, mais elles ne sont pas optimisées pour le rapport signal sur bruit (S/B).

L'objectif principal de ce mémoire a été de concevoir et de construire une antenne radiofréquence (RF) en réseau phasé avec six bobines en réception pour l'IRM de la moelle épinière cervicale chez des sujets humains. La configuration optimale de l'antenne avec six canaux a été déterminée à l'aide de simulations électromagnétiques pour modéliser l'antenne en réception. L'antenne a été conçue et construite pour s'ajuster au plus près du sujet humain tout en étant compatible avec l'interface du scanner IRM. Les performances de l'antenne ont été évaluées sur le banc à l'aide d'un fantôme, ainsi que dans l'IRM sur des sujets humains. Les résultats montrent une amélioration moyenne du rapport S/B par un facteur 2 par rapport à l'antenne commerciale. Cette amélioration permet d'avoir une haute résolution qui facilite la représentation des fins détails comme les petites lésions présentes dans la sclérose en plaques. De plus, la géométrie optimisée de l'antenne permet d'utiliser de hauts facteurs d'accélération (par exemple 3), réduisant considérablement le temps d'acquisition.

Pour conclure, l'antenne en réseau phasé avec six bobines pourrait servir à l'imagerie anatomique de haute résolution (0,3 mm dans le plan), l'IRM fonctionnelle (IRMf), IRM de diffusion et dans études par spectroscopie pour caractériser le métabolisme des tissus présents dans la moelle épinière et les sections inférieures du cerveau.

ABSTRACT

Spinal cord injuries affect a large number of people, therefore a non-invasive technique such as magnetic resonance imaging (MRI) can be used for diagnosis purposes. While current commercial coils are designed to fit a diverse population, they are not optimized for signal-to-noise ratio (SNR).

The major objective of this thesis was to design and construct a six-channel radio-frequency (RF) receive-only phased array coil for MRI of the cervical spinal cord in human subjects. The optimal configuration of the six-channel coil array was determined using electromagnetic simulations framework for modelling the array behavior in the receiving mode. The design and construction of the coil array were focused on offering a tight fit of the human subject, while being compatible with the scanner interface. The RF coil performances were evaluated at the bench using a phantom. Furthermore, it was validated in the MRI on human subjects. The results show an average improvement in SNR by a factor of two compared to the commercial coil. This enhancement enables higher resolution and therefore better depiction of small pathologies such as small lesions in multiple sclerosis. Moreover, the optimized geometry of the RF coil enables the use of aggressive acceleration factors (e.g., 3), which reduces significantly the acquisition time.

In conclusion, the six-channel coil array could be used in high resolution anatomical imaging (0.3mm in-plane), functional MRI (fMRI), diffusion tensor imaging (DTI) and spectroscopy studies for characterizing the metabolism of different tissues present in the spinal cord and lower brain sections.

TABLE OF CONTENTS

LIST OF TABLES

LIST OF FIGURES

LIST OF SYMBOLS AND ABBREVIATIONS

The list of symbols and abbreviations presents the symbols and abbreviations used in the thesis or dissertation in alphabetical order, along with their meanings.

EPI	Echo-Planar Imaging
FOV	Field-of-view
GE	General Electric
GRAPPA	GeneRalized Auto-calibrating Partially Parallel Acquisition
MR	Magnetic resonance
MRI	Magnetic resonance imaging
MRS	Magnetic resonance spectoscropy
NF	Noise figure
NMR	Nuclear magnetic resonance
PILS	Partially parallel Imaging with Localized Sensitivities
PLA	Polylactide
RF	Radio frequency
RL	Return loss
ROI	Region-of-interest
Rx	Receive
SE	Spin Echo
SENSE	SENSitivity Encoding
SMASH	SiMultaneous Acquisition of Spatial Harmonics
SNR	Signal-to-noise ratio
T1	Longitudinal relaxation
T2	Transverse relaxation
TE	Echo time
TR	Repetition time
Tx	Transmit
Tx/Rx	Transmit/Receive

CHAPTER 1   INTRODUCTION

The technology of magnetic resonance imaging (MRI) is based on the development of the unified theory of magnetism by James Clerk Maxwell in the 1960s. This discovery demonstrated that electromagnetic waves can penetrate matter and empty space. The physicists Felix Bloch and Edward Purcell discovered the nuclear magnetic resonance phenomenon in 1945, a discovery which led to winning the Nobel Prize in Physics in 1952 (Sherrow, 2007). The magnetic field applied to the human body induces resonance of the hydrogen atoms due to radio energy. Hydrogen is one of the most common elements of the human body, being present in various amounts in body cells and tissues. In 1970, MRI was first used as a medical diagnostic tool by Raymond Damadian, a medical doctor and research scientist. In 1972, Paul Lauterbur acquired the first MRI image and Damadian patented the first MRI machine (Damadian, 1972).

MRI has the advantage of not using ionizing radiation, while having a good spatial resolution. The imaging can be acquired in every direction or section with a high contrast, which offers a good distinction between the tissues. The information provided is specific to physiology such as vascularization, temperature, cardiac function. The disadvantages are the long acquisition time, the low signal-to-noise ratio (SNR) level, and the movement artifacts. Moreover, claustrophobia encountered by some patients can be mentioned as one of the limitations (Cohen-Adad, 2014).

1.1 MRI technology review

1.1.1 Basic principle

MRI is based on the nuclear magnetic resonance (NMR) phenomenon of atom nuclei, most commonly the hydrogen atoms (H^1) which are present in the tissue that needs to be imaged. The hydrogen atom has a nucleus with a single proton and an electron orbiting the nucleus. The proton has an intrinsic propriety called spin, which means that it rotates around its axis. Due to the combination of spin and electric charge, the proton is characterized by an angular momentum and a magnetic moment. The magnetic moment makes the proton behave like a small magnet, being affected by electromagnetic waves and external magnetic fields.

When an external magnetic field, B_0, is applied the spins align along the direction of the magnetic field lines (z-axis). In addition, the spins begin to wobble around their axis also known as

precession. The precession frequency is called Larmor frequency and is proportional to the applied magnetic field strength. The Larmor frequency is given by the following equation:

$$\omega_0 = \gamma_0 \cdot B_0 \qquad\qquad (1.1)$$

Where ω_0 is the Larmor frequency [MHz], γ_0 is the gyromagnetic ratio particular to the nucleus ($\gamma_{H^1} = 42.58\ MHz/T$), B_0 is the magnetic field strength [T].

One can excite the spins that precess around B_0 by sending an electromagnetic wave using an RF coil at the Larmor frequency, also known as the resonance condition. The spins will be tipped from the z-axis to the transverse plane, resulting in a net magnetization in the transverse plane. After the RF waves are turned off, the spins will tend to come back to the initial state (relaxation), thus emitting RF waves or MR signal (Weishaupt, Kochli, & Marincek, 2006). Two types of relaxation of the protons occur: longitudinal relaxation (T1) and transverse relaxation (T2). Figure 1.1 illustrates the MRI principle. Differences in hydrogen protons binding with the surrounding molecules result in T1 and T2 relaxation times significantly different between tissues.
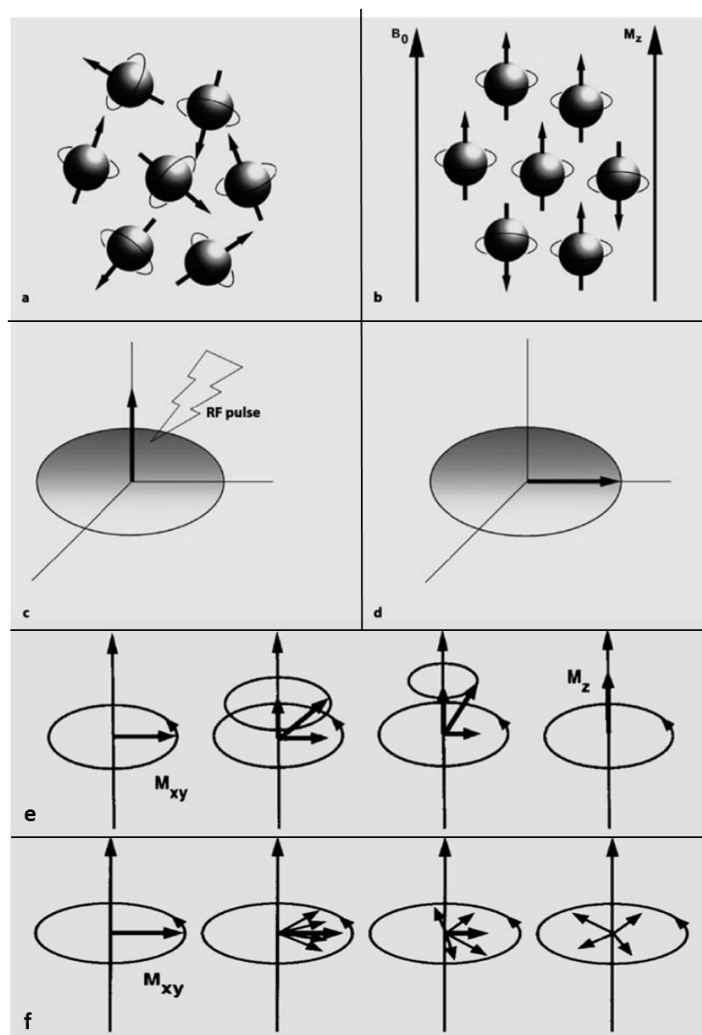
Figure 1.1- Illustration of magnetic resonance imaging principles.

(a) Spins rotate in random directions without any external magnetic field. (b) Spins align along the B_0 field inducing a longitudinal magnetization M_z and rotate at the Larmor frequency (e.g. 127 MHz for 3T). (c) An RF wave of 90 ° is applied, which has the effect of (d) phasing the spins of the proton and inducing transverse magnetization M_{xy} which precesses at the Larmor frequency. When the RF wave stops, the spins of protons will regain their stability by two relaxation processes (e) longitudinal relaxation, when the spins realign themselves to the field B_0 and which is characterized by the relaxation time T1, and (f) the transverse relaxation, that corresponds to the phase shift of the spins in the XY plane and which is characterized by the time T2 relaxation. Source: (Weishaupt et al., 2006)

– maximum gradient amplitude/rise time (Weishaupt et al., 2006). Note that gradient coils can also be used to encode water diffusion in diffusion-weighted imaging (Hagmann et al., 2006).

- **RF coils** – These coils are used for transmitting and/or receiving RF waves at (or close to) the Larmor frequency. They are categorized as transmit coils (Tx), receive coils (Rx) or transmit-receive coils (Tx/Rx). In addition, depending on the covered area the RF coils can be divided in volume coils and surface coils. The RF excitation is produced using the transmit coil usually applied over the entire volume using volume coils. The magnetic field produced by the RF coil is defined as B_1 field. The magnetic field generated by the transmit coils is noted B_{1+} , while the receive coil generates B_{1-} field. In the reception part of the magnetic resonance (MR) signal, the SNR has to be improved. The disadvantage of the volume coils is that they pick up more noise resulting in a SNR decrease. Therefore, surface coils are preferred in the receive mode due to the closer positioning with respect to the region-of-interest (ROI). The interactions between the transmit coil and the receive coil have to be limited due to the fact that both coils are tuned to the same frequency, otherwise the B_0 field profile can be altered.

- **Shim coils** – These coils are used to ensure homogeneous B_0 field within the region of interest through a procedure called "active shimming".

- **Electronic systems for controlling the transmission and reception of RF signals** – These systems consist of gradient amplifiers, RF electronics including receivers and transmitter control units, the pulse sequence computer and image reconstruction computer.

- **Control console** – Used for manipulating and controlling the system by the MRI operator. For example, the Siemens console is called "Syngo".

1.1.3 MRI acquisition

We distinguish two types of MR applications: (i) MR imaging (MRI), which consists of obtaining a detailed representation of the anatomy and (ii) MR spectroscopy (MRS), which consists of obtaining information about metabolic content within a specified ROI.

The spatial encoding and acquisition of an MR signal is achieved using gradient coils and RF coils, respectively. Let's look at an example of acquisition in the axial plane using a Spin Echo (SE) sequence. Firstly, the slice selection is made using a magnetic gradient along the z-axis. As it was mentioned before the magnetic field lines are oriented along the z-axis. Due to the change in the resultant magnetic field, the Larmor frequencies linearly changes along the z-axis. Therefore each slice perpendicular to the z axis will have its unique frequency. Moreover, if the frequency of the RF pulse excites only the protons within the desired slice, the other slices remain unaffected. The thickness of the slice is determined by the strength of the gradient and the bandwidth of the RF pulse. A thin slice is characterized by a strong gradient and a thick slice by a weak gradient. The position of the slice can be changed by changing the central frequency of the RF pulse (Weishaupt et al., 2006).

For MRI, after the slice has been selected, it has to be spatially encoded in order to obtain an image. The spatial encoding consists of two phases: phase encoding and frequency encoding. The spatial encoding is achieved by using additional gradients for x and y axis. The phase encoding is realized by applying a magnetic gradient along the y axis. The applied gradient will cause a phase shift linearly as a function of position along the y axis. The amplitude and duration of the phase encoding gradient will determine the resultant phase shift. Each line along the y axis will have a unique phase. The second stage of the spatial encoding is realized using the frequency encoding gradient. If the magnetic gradient is applied along the x axis, it will result in a change of Larmor frequencies along the axis. The received MR signal is a frequency spectrum. Each unique frequency will correspond to a column of the slice. Consequently, using the phase and frequency information for every point in the slice one can spatially localize every volume element also known as voxel (Weishaupt et al., 2006).

The temporal delay between repeated measurements is called repetition time (TR). The image quality depends also on the phase-encoding gradient. The acquisition time for SE sequences varies depending on repetition time, phase encoding steps, and number of averages. (Schoenberg, Dietrich, & Reiser, 2007).
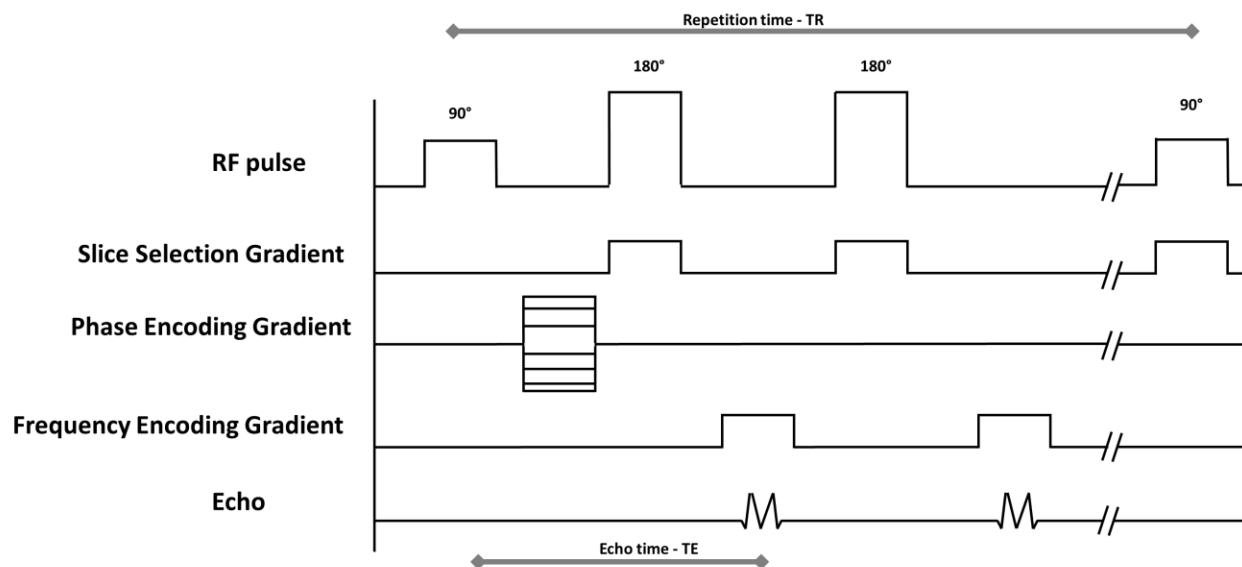
Figure 1.3- Illustration of simplified pulse sequence. Inspired from (Ballinger, 1996)

The MRI raw data is stored in a matrix also called "k-space", which represents the frequency distribution of the MRI data. The center of the k-space corresponds to low frequencies (contrast of the image) while the edge of the k-space corresponds to high frequencies (spatial resolution of the image). The image can be obtained by applying a 2D Fourier transform.

A basic pulse sequence including RF excitation, phase encoding and the frequency encoding of the slice is illustrated in Figure 1.3 .The amount of time between two consecutive RF excitation pulses is called repetition time (TR). Moreover, the echo time (TE) is defined as the time between the RF excitation pulse and the MRI signal sampling.

1.1.4 Parallel imaging

One limitation of the traditional pulse sequence is the acquisition time. A solution to reduce acquisition time is to use parallel imaging techniques.

Parallel imaging takes advantage of high density surface coil arrays. Since the acquisition time is dependent to the acquired number of phase-encoded echoes, it can be reduced if the k-space is under-sampled. A common problem in image reconstruction process is the aliasing. Aliasing is a common MRI artifact which occurs when the FOV is smaller than the imaged body part. In case of aliasing, the body part being imaged which is located outside the FOV will be project to the

other side of the image. A solution is to use the sensitivity profiles of the coils to mathematically reconstruct the image and remove aliasing. Consequently, the coil performance regarding the coil acceleration is related to the coil geometry also called the g-factor. From the parallel acquisition perspective, a lower g-factor offers better coil performances. The lowest g-factor is 1. A high g-factor is associated with reconstruction artifacts and lower SNR. Another characteristic of the parallel imaging techniques is the acceleration factor which is represented by the number of lines that are under-sampled with respect to the k-space.

A series of reconstruction methods that use the spatial information provided by the sensitivity profile of the receive coil array to substitute part of the phase encoding generated by the magnetic field gradients have been proposed. They include: SiMultaneous Acquisition of Spatial Harmonics (SMASH) (Sodickson & Manning, 1997), SENSitivity Encoding (SENSE) (Pruessmann, Weiger, Scheidegger, & Boesiger, 1999), Partially parallel Imaging with Localized Sensitivities (PILS) (Griswold, Jakob, Nittka, Goldfarb, & Haase, 2000) and GeneRalized Auto-calibrating Partially Parallel Acquisition (GRAPPA) (Griswold et al., 2002).

1.2 Rationale

The RF coil is an important component of the MRI system. It is used to transmit and receive MRI signal. The coil design has to be properly adapted to the ROI that needs to be imaged and the desired imaging protocol. Therefore, mechanical aspects such as coil element dimension and positioning or electronic aspects such as electronic component performances have an important impact on the coil performance (Keil, 2013).

The current thesis is focused on developing a RF coil for imaging the human cervical spinal cord. The spinal cord is an important component of the central nervous system and it occupies the upper two-thirds of the vertebral column (Gray, Goss, & Alvarado, 1973). The spinal cord assures the transmission of neural signal from the brain to the rest of the body, being responsible for three important functions: body sensation, automatic and motor control. These functions can be compromised (e.g., paralysis) in pathologies such as traumatic spinal cord injury, multiple sclerosis or cancer. This brings the rationale for imaging the spinal cord non-invasively with MRI. Having a coil that provides high SNR and low g-factor will enable higher spatial resolution and acceleration factors, which will in turn improve diagnosis.

1.3 Research objectives

The main objective was to design and construct a highly sensitive coil for proton imaging of the human cervical spinal cord at 3 Tesla (Larmor frequency: 123.2 MHz). The principal objective can be divided into specific objectives:

- To develop an electromagnetic simulation framework for the assessment of the magnetic field sensitivity profile for comparing different coil array geometries in order to determine the optimal configuration;

- To design and construct a receive-only coil including ergonomic support of the neck compatible with the Siemens Trio scanner infrastructure available at our research center;

- To evaluate the performance of the RF coil array at the bench using a water phantom; security recommendations will also be evaluated;

- To validate the coil on the MRI scanner using a water phantom and human subject.

1.4 Literature review

1.4.1 RF coils

1.4.1.1 Phased array coils

The design of high-density surface RF coils is an important research subject for many groups around the world since the beginning of the 1990s. The current literature review will be focused on a series of important aspects that have to be taken into consideration by the coil designer such as theoretical modelling of SNR, electromagnetic simulations of the sensitivity profile of the RF coil and finishing with different implementations of multi-channel phased arrays.

One of the most important principles used in the development of receive coils is the reciprocity theorem. This theorem which was initially formulated in antenna theory is stating that the characteristics of an antenna in the receiving mode can be obtained from the same antenna used in the transmitting mode (Neiman, 1943). Hoult and his associates (D.I Hoult & Richards, 1976) demonstrated that the magnetic field produced at a point in space by a unit current in a RF coil is proportional to the electromotive force induced in the coil by a magnetic dipole at the same point. Another research based on a series of bench experiments has provided the mathematical basis to derive the equations for the B_1 field generated by the RF coils. The purpose of knowing the field sensitivity profile is to correctly approximate the received signal in an NMR experiment (D. I. Hoult, 2000). Another group developed the reciprocity theorem for NMR which states that the sensitivity of NMR signal from a sample is proportional to the intensity of the magnetic field generated by the current circulation in the coil (D. I. Hoult & Richards, 2011). The experiment of Ackerman demonstrated that SNR can be improved by a surface coil close to the ROI of the sample (Ackerman, Grove, Wong, Gadian, & Radda, 1980). Consequently, SNR is influenced by the magnetic field intensity received by the coil. The key parameters for defining the quality of a MRI acquisition are the SNR and the acquisition time. The time of acquisition of a MRI image dataset can be reduced either by using faster gradients or by optimizing the receiving RF technique. The initial proposed optimization of the RF coil consisted of connecting multiple coils to form an array structure. The acquisition time decreased due to better spatial localization of the MRI signal.

To begin with, an initial optimization of the RF coils was the introduction of phased-arrays (Roemer, Edelstein, Hayes, Souza, & Mueller, 1990). Since then, the development of new arrays has pushed forward with an increased number of channels improving the sensitivity of the scanners. The advantages of having an array of coils are the increase of SNR and increased field-of-view (FOV) comparable with body imaging. In addition, the required scan time is reduced due to the number of channels and the optimized method of phase encoding. The approach used by Roemer et al. to optimize the SNR in a 3D volume consisted of comparing three different surface coil configurations: an 8-cm square coil, a single large 30x15-cm rectangular coil and a four element phased array made of 8-cm square coils. The computed SNR for the 4-channel linear spine array provided a SNR 2 to 3 times higher than a single channel rectangular coil for the same FOV at the same level of depth. Moreover, in the case of circular loop coils, the optimal SNR was achieved at a depth equal to diameter of the coil. High resolution spin-echo images of the thoracic and lumbar spine were acquired to demonstrate the phased array imaging viability. Another aspect discussed in the article was the problem of interactions among neighboring coils which can be limited by overlapping adjacent coil in order to reduce mutual inductance or by using low impedance preamplifiers decoupling technique. The distance between the centers of two co-planar circular loops for cancelling their mutual inductance was found to be 0.75 times their diameter, compared to 0.9 times for square coils. In addition, the authors proposed various image reconstruction techniques for determining weights for combining images or spectroscopic data such as sum-of-squares combination.

Using the framework developed by Roemer, in 1991 Hayes et al. (Hayes, Hattes, & Roemer, 1991) built a volume 4-channel phased array having two coils placed anterior and two coils posterior to the human pelvis. An SNR improvement of 80% was obtained for a single image using the array when compared with the body coil. Additional comparisons with two-channel phased array and a Helmholtz pair revealed similar results. Thus, the SNR improvement can be used to reduce the slice thickness and to reduce the number of excitations. Future research (Hayes, Dietz, King, & Ehman, 1992) was focused on the quantitative assessment of SNR in pelvic imaging conducted on water-filled phantom that simulated RF loading effects. The SNR produced by the longitudinal array was 2.3 to 3.1 times higher than the SNR offered by the body coil.

Depending on the ROI, a custom built RF coil can provide better performances than the commercial body arrays. For example, a two and four channel phased arrays for 1.5T General Electric (GE) scanner have been proposed by Wald (Wald et al., 1995) to increase the sensitivity and resolution of human brain cortex imaging. The main motivation for developing phased arrays is the lack of signal intensity uniformity over a larger area such as the human brain. The sensitivity of the coils at the surface of the cortex was 600% higher than the commercial head coil. In addition, the signal decrease with the depth which is characteristic to the size of the component coils can be problematic when an optimal view of different regions of the image is required. A solution to this problem is low pass filtering of the anatomical image by a phantom image. For SNR measurements, the method is similar to the one proposed by Hayes (Hayes et al., 1991) and implies the acquisition of two successive images of the phantom. The resultant SNR was calculated by the sum of the two images and the noise at the same given pixel in the image.

Another application of the phased arrays was a prototype cardiac 4-channel phased array receiver coil for 1.5T GE Sigma scanner. The array comprised of a 2-channel cylindrical array positioned on the chest and a separate 2-channel planar array positioned at the back (Constantinides, Westgate, O'Dell, Zerhouni, & McVeigh, 1995). The computed SNR over the heart region was 1.1 to 2.85 times higher than a commercial flexible coil. Another phased array developped on a 1.5T GE scanner for the assessment of atherosclerotic plaques in the carotid artery was implemented for obtaining high resolution images (Hayes, Mathis, & Yuan, 1996). The 2-channel silver-braid carotid phased array provided improved FOV, an enhanced adaptability to wide variations in patient anatomy and reduced susceptibility to motion artifacts better than the single channel circular commercial coil. The maximum array improvement compared to the 3-inch commercial coil was 37 %. The SNR of the image acquired with the carotid phased array was 93, being higher than the SNR of 80 generated by the commercial coil.

1.4.1.2 Simulations

A large number of research groups have focused their studies on developing an approach to numerically model the ultimate SNR. A series of experiments conducted on different body coil combinations at different intensities of the static magnetic field revealed that the intrinsic SNR is proportional to the B_0 field (Edelstein, Glover, Hardy, & Redington, 1986). The conventional approach to measure the SNR uses line integrals over the electric currents in the coils. A novel

method based on surface integrals over magnetic dipoles which cover the area enclosed by the coil offered newer perspectives (Jianmin, Reykowski, & Dickas, 1995). This method was used to derive the maximum SNR for an ideal receive array coil. The calculated SNR of the array was 35.8% higher than for single circular loop size-optimized and linearly polarized coil. When the sample noise is dominant, the intrinsic SNR for gradient-encoded imaging can be improved by minimizing the power deposition in the sample while maintaining a proper circularly polarized magnetic field at the ROI (Ocali & Atalar, 1998). The electromagnetic field optimization and intrinsic SNR maps obtained from simulations were compared to phantom image acquisitions. The results showed that overall performance can be improved if the electromagnetic field is focused on the ROI to compensate the skin effect which produces signal loss.

More electromagnetic field considerations related to the optimal intrinsic SNR were made by Ohliger et al. (Michael A Ohliger, Grant, & Sodickson, 2003). Their aim was to optimize the spatial encoding proprieties of the RF coil sensitivity profile instead of changing the geometry of the conductors. They proposed a protocol for obtaining an optimal coil sensitivity profile using plane waves simulations over an elliptic phantom for a given acceleration. The disadvantage of using higher accelerations for increased field strengths was the drop in SNR. The results show considerable advantages in terms of acceleration for high static magnetic field strengths when using 2D under-sampling of k-space. Another useful insight was the impact of the electrical conductivity of the sample on the use of surface coils for spatial encoding. The optimum achievable SNR profile was higher on the edges of the sample and lower in the center of it for 1.5T and 5T static field strengths.

Using a different approach, an important paper (Wright & Wald, 1997) is focused on the optimization of SNR of the receive coil by taking into account the efficiency of the phased array transmit coil. The benefit of using this approach is that the developed theory can be used also for developping transmit array coils. Using numerical simulations, multiple geometries of planar arrays of 2x2, 4x4 and 8x8 elements were compared to a single coil with similar size. Results show that the sensitivity profile is improved in the region near the array coil. In order to optimize the ratio of transmitted power, one can optimize the SNR in the receiver case and use the resultant weighting coefficients based on the reciprocity theorem.

The acceleration limit and its relation with the SNR was studied by Wiesinger et al. (Wiesinger, Boesiger, & Pruessmann, 2004). From SENSE parallel sensitivity encoding it is known that the SNR is inversely proportional to the geometry factor. One of the limitations of the SNR model is that it cannot be used for *in vivo* applications. The results show that the SNR performance was almost optimal when using low to moderate acceleration of geometry factors near 1. For higher acceleration, the exponential increase of the geometric factor decreased the achieved SNR. The behavior of the critical reduction factor was different depending on near and far field regimes. The critical reduction factor is independent of the static magnetic field and object size in the near field regime. In the case of far field, the factor is dependent on the object size and the B_0. For B_0 field higher than 7T the far field regime could be used for parallel imaging.

Furthermore, the same author proposes a method for approaching the ultimate SNR using finite coil arrays (F. Wiesinger, 2005). In order to evaluate the parallel imaging performance of finite arrays, the circular current distributions and theoretical SNR were compared. To render the calculations more realistic, coil sensitivity profile and noise receiver noise were taken into account in the SNR computations. The electrodynamic dependencies of SNR were the static field strength and the sensitivity profile of the coils. Multiple coil arrangements with various elements distributed around a spherical object which approximates the human head were compared. For the case of a static field of 1.5T, the configuration with 32 coils offered 4.6 times higher SNR than the 8 coil configuration.

Having a powerful tool for the electromagnetic simulations can help the developer to achieve the best coil configuration for its application. Full-wave numerical MoM analyses for evaluating the intrinsic SNR were purposed (Kumar & Bottomley, 2006; Kumar, Edelstein, & Bottomley, 2009). The experiments conducted using a circular loop coil configuration revealed that the noise related to the loop increases relative to the sample noise when the loop radius decreases. The noise figure (NF) of a 3cm diameter coil for a 3T static field was 0.8dB compared to 0.2dB for a 7T static field. In addition, strip detectors with length about 1.3 (+/- 0.2) times the depth of interest offered comparable results to loop coils with similar dimensions, the only difference was the characteristically different spatial distribution of the field from a loop.

1.4.1.3   Coil design

The parallelization of the receiver proved to enhance the SNR with the increased number of coil elements when compared to volume coils or single coils with the same covering area. In order to achieve the optimum SNR, the configuration of the coil array is important. Multiple papers focused on the coil design illustrate different approaches depending on the application. The next section will be focusing on the coil design for surface arrays. Depending on the region of interest and the desired scanning protocol, the designer has to decide the number of channel used in a receive phased array.

An article focused on the general design considerations of coil arrays for parallel MRI made a qualitative analysis from the theoretical and the practical point of view (Michael A. Ohliger & Sodickson, 2006). The qualitative analysis made on the spatial encoding using coil arrays offered a model for the emulation of the spatial harmonics and a solution for unfolding the aliased data. The numerical models were developed using SENSE and SMASH image reconstruction techniques. Depending on the particular image plane orientation, FOV and acceleration factor, the coil design has to be optimized in order to achieve the maximum SNR. For the cervical region, the authors suggest using an adaptive combination of coil array elements due to the degree of freedom in imaging multiple anatomical regions with the same coil array.

Another paper addresses the problem of maximum number of elements that is required to achieve high quality images and reduced acquisition time (Fujita, 2007). The emphasis on preamplifiers is made due to the fact that they play an important role beyond signal amplification. The preamplifiers are used for achieving the optimal SNR and to improve the performance of parallel imaging techniques in terms of proper decoupling between coil array elements. Important considerations have to be taken into account when designing the coil array to properly balance the spatial resolution (SNR) and the temporal resolution or the speed of acquisition for the desired clinical application.

In order to achieve a greater degree of flexibility of the coil design, a modular design of receive only arrays was proposed (De Zanche, Massner, Leussler, & Pruessmann, 2008). The difference of this approach is that the preamplifier board, matching and active detuning circuits are built in a circuit board for each coil. This type of configuration offers robustness to geometrical variations of coil loop arrangements being able to achieve reconfigurable coil arrays. The results illustrated

that the independent distribution of coils without overlap provides a reduced noise correlation between elements over the configuration with overlapped coils.

A 32-channel 3T receive-only phased-array head coil was developed for human brain imaging compatible with SENSE reconstruction technique (Wiggins et al., 2006). The coil elements were arranged in a helmet shaped having a soccer ball pattern of hexagonal and pentagonal symmetry. The quantitative evaluation of the SNR showed a 3.5 times improvement in the cortex compared to the 8-channel head coil. The array was able to achieve acceleration of four and five while providing high resolution brain images. Moreover, the coil array offered reduced g-factors for x and y accelerations.

In addition, a size optimized for five age groups for pediatric brain imagining consisting of 32 channels tight fitted to the coil-former was proposed (Keil, Alagappan, et al., 2011). The coil-former was designed using 3D MRI images for each group. The commercial coil used for brain imaging of infants is a birdcage coil. The highest SNR increase was observed in the neonate coil with up to 3.6 more within the brain cortex compared to the 32-channel coil for adults. The conclusion of the study was that the size and the fitting of the coil around the ROI is very important making possible sensitivity gains for accelerated brain imaging in infants.

The previously presented 32-channel coil for adults was compared with a 64-channel 3T receive-only coil placed in a similar holder (Keil et al., 2013). The split-former design of the holder makes the coil very ergonomic for the patient being suitable for every-day clinical use. The unaccelerated images offered 1.3 times more signal in the brain cortex for the 64-channel array. An acceleration of 4 times was achieved using the new coil, while maintaining a low noise amplification compared to the previous coil.

The high parallelization of the receive arrays was analyzed and reviewed in a recent paper (Keil & Wald, 2013). The aim was to present the theoretical and practical aspects for developing high density arrays based on the information obtained from theoretical modelling and experiments of the ultimate SNR. In order to build highly parallel arrays, the interactions between neighboring elements have to be reduced, thus circuits for achieving the proper level of preamplifier decoupling, taking into account the fact that the coil impedance needs to be matched to the required noise figure matching of the preamplifier. The suggested initial phase of the construction of a RF coil consisted of the complete 3D design of the coil housing and electronics, including

the cable routing and preamplifier mounting supports. The mass production of elements and the population of the coil former with all elements was found to be impractical .It is recommended to add individual loops and to assess their performance before adding additional loops. The next neighboring elements optimization was found to be the most consuming coil procedure, a test rig being necessary in order to detune all the other elements. Current parallel imaging techniques use higher numbers of detectors driven by sensitivity arguments. The individual sensitivity profile of each coil is used for spatial information during signal encoding step.

1.4.2 Coils for spinal cord
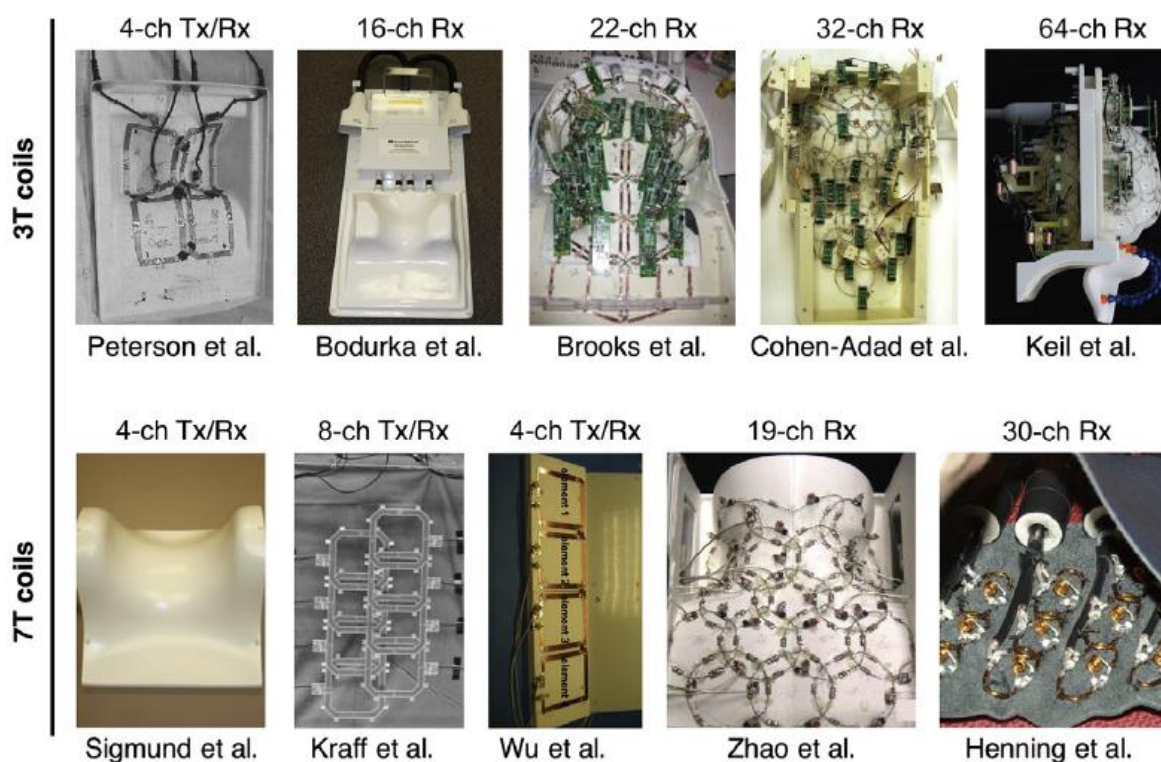
Figure 1.4- Pictures of spine array coils for 3 T (top) and 7 T (bottom). Source: (Cohen-Adad & Wheeler-Kingshott, 2014)

The following sections will review different coil configuration proposed for imaging the spinal cord in humans.

A head/neck coil with 16 independent channels combined to clusters was proposed for Siemens scanners (Reykowski, Hemmerlein, & Fischer, 2005). The design offered improved g-factors in different directions such as anterior-posterior, left-right and head-feet. Due to the modular design

of the channel combination, the coil can be combined with other matrix coils for extending the coverage area. The head area was covered by 12 elements with independent preamplifiers combined into 3 modes combiners. The neck region has 2 elements posterior and 2 anterior. The signals are combined in 2 modes matrices.

An optimized 16-channel receive-only array for cervical spinal cord imaging was proposed for a 3T General Electric scanner (Bodurka, Ledden, & Bandettini, 2008). The coil had a 4x4 arrangement of elements fixed on a rigid curved former. The loops had an elliptical shape of 8x6cm copper trace printed on a flexible substrate. The spacing between adjacent columns was adjusted to a ratio of 30% to improve the axial g-factors. Each element had an active detuning circuit and a passive detuning one, with additional baluns to cancel the common mode currents. The coil was initially validated using gradient echo imaging for phantom. Further validations were performed for human subject imaging using fast spin echo sequence with flow compensation and fat suppression and single shot echo-planar imaging (EPI) with SENSE. The results illustrate that the coil offered a large coverage from the brain visual cortex as low as the tenth cervical segment. The high resolution SENSE EPI capabilities offer the possibility of further fMRI investigation of the spinal cord.

An 8-channel Tx/Rx phased array coil composed of surface loop coils with a dimension of 12cm x 12cm was developed for spine imaging at 7T (Kraff et al., 2009). The coil was validated on 3 subjects by using 3D-FLASH sequence with an isotropic resolution of 0.57mm. The high spatial resolution illustrated the longitudinal ligaments or the venous drainage through the vertebral bodies. The g-factor for head-feet direction was reported 2.7 with an extended FOV of 40cm.

A high field application of the RF Tx/Rx coils for the spine imaging on a 7T GE scanner proposed using adjustable inductive decoupling between adjacent elements (Bing et al., 2010). Three Tx/Rx coils (12cm x 12cm with four channels, 12cm x 8cm with six channels and 12cm x 6cm with eight channels) were built and compared. The novelty was the adjustable inductive decoupling which offered -25dB decoupling between nonadjacent elements in different loading conditions. The four-channel array achieved g-factor of 2, 3 and 4 without important artifacts in the reconstructed image. The proposed coil was not fully optimized for the spinal cord imaging, therefore better shimming and the reduction of motion artifacts could provide better performances.

Another coil design was proposed for brain and cervical spinal cord imaging (Cohen-Adad, Mareyam, Keil, Polimeni, & Wald, 2011b). The 32-channel receive coil was optimized for a 3T Siemens scanner: 4 of the channel were used to image the neck region, 3 of them for the spine and the remaining were distributed in a soccer ball pattern to cover the brain. The temporal SNR obtained by the custom built coil was 2 times higher for the brain region and 1.8 times for the cervical spinal cord when compared to the commercial coil. In addition, the authors reported high resolution diffusion imaging of the spinal cord at 0.6x0.6x5 mm^3 using GRAPPA reconstruction without noticeable distortion.

A custom coil built for 3T Head/Neck/C-spine imaging was integrated with the spine coil to offer a large coverage and better accelerations (Keil, Biber, et al., 2011). The coil had 60 channels distributed in a hexagonal and pentagonal pattern. The coils were combined using low noise converters for multiplexing two channels onto a single output. The coil performances were compared with a 20 channels and a 32 channels coils. The 64-channel coil provided an improved SNR in the cervical region of 1.8 times than the 20-channel head/neck array. The sensitivity profile was slightly improved when compared with the 32 channel brain coil, especially in the cortex.

A 4-channel coil array for ultrahigh field was prototyped and compared with a standard 3T coil (Sigmund et al., 2012). The 7T array had an improved SNR by a factor of 3.5 in the cervical region than the 3T coil. The increased SNR made possible depiction of internal structures such as the nerve roots and rostral-caudal blood vessels. The SNR and the magnetic field distribution provided by the coil were estimated using the Kellman method (Kellman & McVeigh, 2005). The cross-sectional areas of gray/white matter obtained using 7T images were similar to reports from histology.

An ^{1}H MRS in the human spinal cord was developed and tested on healthy volunteers for a 7T field strength using RF shimming and travelling wave transmit approach (Anke Henning, 2012). The RF shimming was used due to the important susceptibility changes caused by the flow of cerebrospinal fluid and the respiratory motion of the patient. The transmit coil consisted of two radiative antennas fixed around the neck using a pillow filled with D_2O. A custom built 30-channel sensitivity optimized array was used for signal reception. Inner volume saturation, VAPOR water suppression and 3rd order FASTERMAP shimming were applied to improve the

spectra. The final spectra for the C2/3 levels of the spinal cord had limited artifacts such as lipid contamination, ghosting, baseline or phase distortions.

Another dedicated cervical spinal cord with 4-channel transmit and 19-channel receive was implemented for 7T scanner (Zhao et al., 2014). The elements were placed on a close-fitting coil former. The transmission performances efficiency and absorption rate were evaluated using B_1 field mapping and electromagnetic simulations. The SNR performances were compared with a 19 channels receive 3T neck array and 4-channel spine for 7T. The SNR was 4.2 times higher for the 7T array when compared to the 3T commercial coil. A higher acceleration was achieved using the 7T coil. Moreover, when compared to the 4-channel spine receive array for 7T, the SNR increased 1.5 times in the spinal cord. A spatial resolution of 0.3 mm was achieved in spinal cord imaging.

1.4.3 Synthesis of literature review

After reviewing the solutions proposed in the literature review, one can make some remarks and conclusions:

- There is a limited number of RF receive coils dedicated to the cervical region of the spinal cord, most of the available coils are covering the brain and the neck regions. These coils have a higher density for the brain, than for the neck region.

- The design of a RF receive-only coil has to be adapted to the anatomy to be imaged. Firstly, the coil former has to offer a high degree of comfort for the patient. Moreover, the distribution of the elements of the array has to be optimized in order to provide a large coverage, while producing uniform sensitivity profile.

- The recommended procedure for constructing an RF coil begins with electromagnetic simulations for determining the adequate loop geometry and alignment for the targeted area of imaging. Once the optimal configuration is found, one can start building the array using non-magnetic materials and low loss electronic components. Moreover, one can define the expected performance indicators for the bench measurements :

    o Tuning frequency: Considering the magnetic field generated by the scanner for 3T is 123.2 MHz.

o Q factor ratio should be as high as possible; consequently the coil losses should have smaller in the power losses (Keil, 2013; Kyle M. Gilbert & Menon, 2015).

o Active detuning: The amplitude difference between the maximum S_{21} when tuned and the minimum S_{21} when detuned should to be less -35dB (Keil, 2013; Kyle M. Gilbert & Menon, 2015).

o Geometric decoupling: the decoupling level between neighboring loops should be less than -12dB (Keil, 2013; Kyle M. Gilbert & Menon, 2015).

o Preamplifier decoupling: The amplitude difference between the maximum S_{21} when the preamplifier is replaced by a conjugate impedance and the minimum S_{21} when the preamplifier is connected should be less than -15dB (Kyle M. Gilbert & Menon, 2015).

CHAPTER 2   MATERIALS AND METHODS

2.1 Electromagnetic simulations

The first step in the construction of the RF coil was the development of electromagnetic simulations of various configurations in order to determine the optimal element configuration in terms of loop geometry and positioning.

2.1.1 MATLAB

The electromagnetic simulations were developed for the assessment of the magnetic field sensitivity profile and the SNR maps. For the robustness of computation, the proposed numerical simulations are based on the Biot-Savart law. The numerical simulations consider quasistatic electromagnetic conditions, integrating the Biot-Savart law along the path of a loop circulated by a steady current. The quasi-static conditions use static assumptions for computing the magnetic flux density and the magnetic vector potential. The electric field is computed assuming a time-varying field. Using the electric field of the coil, one can approximate the losses generated in the sample. The simplified estimation neglects the mutual coupling between the elements, thus considering ideal preamplifier decoupling conditions and wavelength effects. The proposed model does not enforce all boundary conditions on the fields, while providing proper results for applications in MRI and MRS (Wright & Wald, 1997). The resultant B_1 field for the combined array was determined using the sum-of-squares of individual field profiles of the elements.

2.1.1.1   Magnetic field sensitivity profile

The basis of the magnetostatics is a particular case of the Maxwell equations. The electric and magnetic fields can be generated and influenced by each other and by charges and currents (Lehner, 2008). The Maxwell equations for describing the magnetostatic conditions are listed below.

Table 2.1- Maxwell equations used in magnetostatics.

Name	Differential form	Integral form
Gauss's law for magnetism	$\nabla \cdot \boldsymbol{B} = 0$	$\oint_S \boldsymbol{B} \cdot d\boldsymbol{S} = 0$
Ampere's law	$\nabla \times \boldsymbol{H} = \boldsymbol{J}$	$\oint_C \boldsymbol{H} \cdot d\boldsymbol{l} = I_C$

Where ∇ is the divergence operator, **B** is the magnetic field density, the integral over a surface S with the surface element d**S**, **H** is the magnetic field intensity, **J** is the current density and the integral over a closed contour C with a segment element dl, I_c represents the current circulating through the loop.

Furthermore, one can establish a relation between **B** and **H** for vacuum conditions:

$$\boldsymbol{B} = \mu_0 \boldsymbol{H} \tag{2.1}$$

Where $\mu_0 = 4\pi \times 10^{-7} H/m$ representing the permeability of free space.

The objective of using the magnetostatic conditions is to characterize the magnetic field generated by different coil configurations. A formal method of calculating the magnetic field is using the vector potential **A**. Using the property that the divergence of the curl is equal to zero:

$$\nabla \cdot (\nabla \times \boldsymbol{a}) = 0 \tag{2.2}$$

The Gauss's law for magnetism in differential form can be written as:

$$\mathbf{B} = \nabla \times \boldsymbol{A} \tag{2.3}$$

If the current density **J(r)** has a complete description then the magnetic vector potential can be determined from the current:

$$\boldsymbol{A} = \frac{\mu_0}{4\pi} \int \frac{\boldsymbol{J(r)}}{\boldsymbol{r}} d^3 r \tag{2.4}$$

Where **J(r)** is the current density, **r** is the pointing vector from the coil to the observation point and the integral is over the whole volume of observation.

On the other hand, if we apply (2.3) to (2.4) we can write the Biot-Savart law. The Biot-Savart law describes the magnetic field generated by a steady current.

If one analyses the case of a small length element of wire, the resultant magnetic field is defined by:

$$dB = \frac{\mu_0 I}{4\pi} \frac{dl \times \hat{r}}{r^2} \qquad (2.5)$$

Where I is the steady current, μ_0 is the permeability of the vacuum, dl is the length element of the wire, $\hat{r}$ is the unit vector between the wire and the observation point.
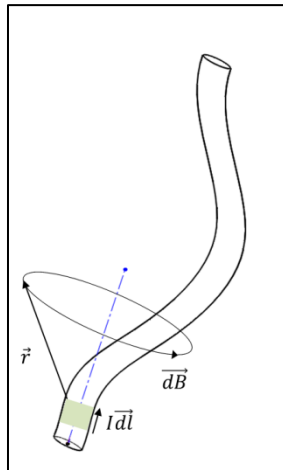
Figure 2.1- Geometry of the magnetic field of a current circulating a small element of wire.

Furthermore, the analysis of the magnetic field can be extended for a closed circular loop with the radius R. Figure 2.2 illustrates the magnetic field components $(\overrightarrow{dB_x}, \overrightarrow{dB_y}, \overrightarrow{dB_z})$ for a small wire element $\vec{dl}$ computed at the observation position defined by $\vec{r}$ on the axis of the loop is the pointing vector between the wire and the observation point.
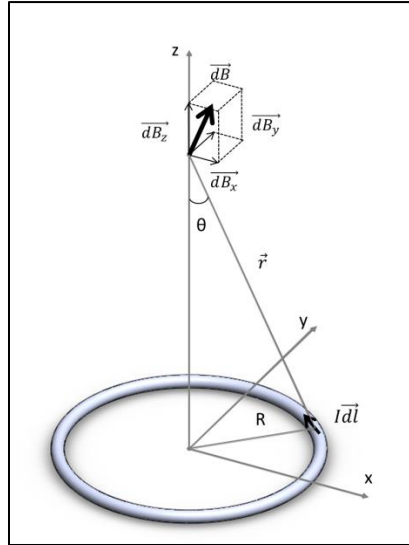
Figure 2.2- The magnetic field generated by a current loop segment on an arbitrary point on the center axis.

Using Biot-Savart law over a closed contour, it results:

$$\boldsymbol{B} = \int d\boldsymbol{B} = \frac{\mu_0 I}{4\pi} \int \frac{d\boldsymbol{l} \times \hat{\boldsymbol{r}}}{r^2} \tag{2.6}$$

This integral can be approximated by the summation:

$$\boldsymbol{B} \approx \frac{\mu_0 I}{4\pi} \sum \frac{d\boldsymbol{l} \times \hat{\boldsymbol{r}}}{r^2} \tag{2.7}$$

The approximation is valid when $d\boldsymbol{l}$ is small enough.

If we generalize the problem for a 3D Euclidian space, the components of $d\boldsymbol{l}$ and $\hat{\boldsymbol{r}}$ can be defined for each direction:

$$d\boldsymbol{l} = dl_x \hat{\boldsymbol{i}} + dl_y \hat{\boldsymbol{j}} + dl_z \hat{\boldsymbol{k}} \tag{2.8}$$

$$\hat{\boldsymbol{r}} = \frac{1}{r} [r_x \hat{\boldsymbol{i}} + r_y \hat{\boldsymbol{j}} + r_z \hat{\boldsymbol{k}}] \tag{2.9}$$

Where $r = \sqrt{r_x^2 + r_y^2 + r_z^2}$.

Due to the fact that we are working in a 3D space, the cross product can be written as:

$$dl \times \hat{r} = \begin{vmatrix} \hat{\imath} & \hat{\jmath} & \hat{k} \\ dl_x & dl_y & dl_z \\ r_x & r_y & r_z \end{vmatrix} = \frac{1}{r} \left[(dl_y r_z - dl_z r_y)\hat{\imath} + (dl_z r_x - dl_x r_z)\hat{\jmath} + (dl_x r_y - dl_y r_x)\hat{k} \right] \tag{2.10}$$

If we replace (2.10) in (2.7):

$$\boldsymbol{B} \approx \frac{\mu_0 I}{4\pi} \sum \frac{dl \times \hat{r}}{r^2} = \frac{\mu_0 I}{4\pi} \sum \frac{1}{r^3} \left[(dl_y r_z - dl_z r_y)\hat{\imath} + (dl_z r_x - dl_x r_z)\hat{\jmath} + (dl_x r_y - dl_y r_x)\hat{k} \right] \tag{2.11}$$

Since $\boldsymbol{B} = B_x\hat{\imath} + B_y\hat{\jmath} + B_z\hat{k}$, the solution for each direction is :

$$B_x \approx \frac{\mu_0 I}{4\pi} \sum \frac{1}{r^3}(dl_y r_z - dl_z r_y) = \sum dB_x \tag{2.12}$$

$$B_y \approx \frac{\mu_0 I}{4\pi} \sum \frac{1}{r^3}(dl_z r_x - dl_x r_z) = \sum dB_y \tag{2.13}$$

$$B_z \approx \frac{\mu_0 I}{4\pi} \sum \frac{1}{r^3}(dl_x r_y - dl_y r_x) = \sum dB_z \tag{2.14}$$

The magnitude of $\boldsymbol{B}$ is given by:

$$|\boldsymbol{B}| = \sqrt{B_x{}^2 + B_y{}^2 + B_z{}^2} \tag{2.15}$$

2.1.1.2 SNR

The magnetic field sensitivity profile provides important information about the magnetic field distribution of the RF coil. For a quantitative evaluation of the RF coil, SNR simulations provide useful insights regarding the mutual noise between the elements of the array. The SNR was computed using the method proposed by Roemer (Roemer et al., 1990). Aiming to construct a uniform sensitivity image, the SNR can be calculated as:

$$SNR = \sqrt{\boldsymbol{B}^T \boldsymbol{R}^{-1} \boldsymbol{B}^*} \tag{2.16}$$

Where **B** is the magnitude of the magnetic field and **R** is the mutual noise resistance matrix.

Since we have computed the magnetic vector potential and assuming a constant frequency, we can compute the mutual noise resistance matrix within a sample as (Roemer et al., 1990):

$$R_{ik} = \omega^2 \sigma \int A_i \cdot A_j \, d^3V \qquad (2.17)$$

Where $\mathbf{R_{ik}}$ is the mutual noise resistance between coil i and coil k, ω is the angular frequency, σ is the conductivity of the sample, the magnetic vector potentials $\mathbf{A_i}$ of coil i, respectively $\mathbf{A_j}$ of coil j and the integral is computed over the volume V.

2.1.1.3 Proposed configurations

The simulations were run for 4 distinct configurations:

- Configuration a: single channel circular loop with 6cm radius

- Configuration b: 2-channel array circular loop with 6cm radius

- Configuration c: 4-channel array with circular loop with 3cm radius

- Configuration d: 6-channel array with elliptical loop with 2.75cm x 3cm

These configurations were based on preliminary work, and account for the geometry of the neck. The elements were uniformly distributed in the lower half of 8cm cylinder. The radius of the cylinder is similar to the radius of the neck former (Figure 2.3). The suggested simulations are made in order to determine the optimal configuration for B_1 field penetration and SNR.
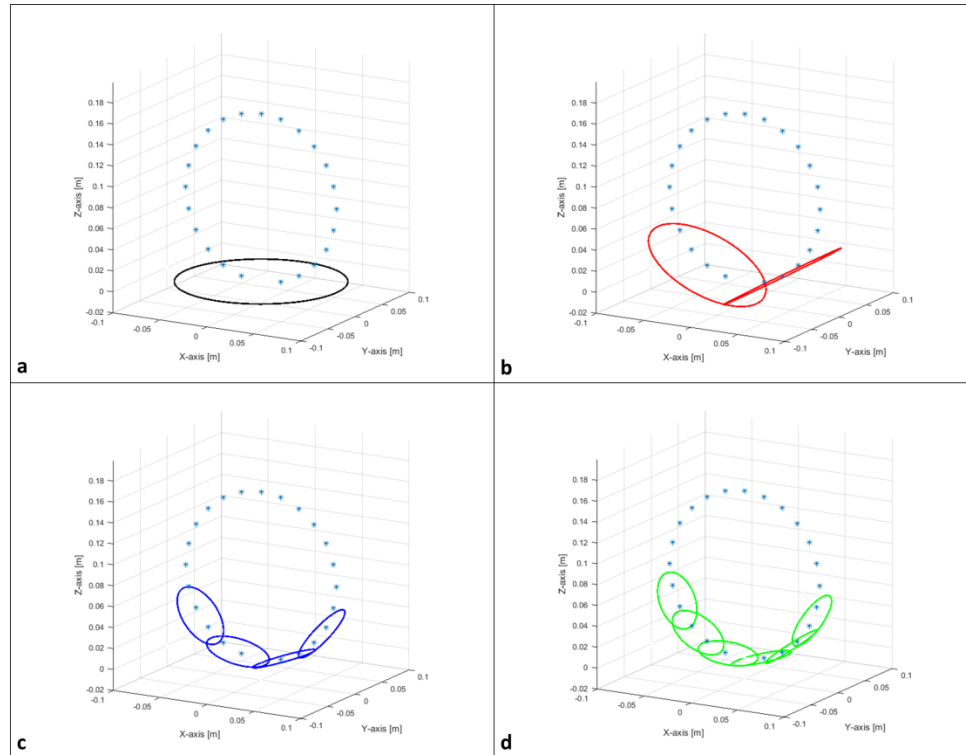
Figure 2.3- Distribution of coils around the former (blue circle). (a) Single channel coil array. (b) 2-channel coil array. (c) 4-channel coil array.   (d) 6-channel coil array.

The request for the B_1 field sensitivity profile and the SNR maps were computed for space defined by:

- X axis – inferior limit: -20cm; superior limit: 20 cm; step size: 0.1cm;

- Y axis – inferior limit: 0cm; superior limit: 0 cm; step size: 0.1cm;

- Z axis – inferior limit: 0cm; superior limit: 40 cm; step size: 0.1cm.

2.1.2 FEKO

2.1.2.1 Validation of MATLAB simulations

We propose a validation of the scripts developed in Matlab using commercial software for electromagnetic simulations based on the Method of Moments (MoM) (FEKO, Altair Development S.A. (Pty) Ltd, South Africa). Inspired from the configurations proposed by Roemer (Roemer et al., 1990) we evaluated the B_1 field sensitivity profile at 80mm depth for three different coil arrangements (Figure 2.4):

- Configuration a: 4 element array made of 8 cm circular coils;

- Configuration b: single element 8 cm circular coil;

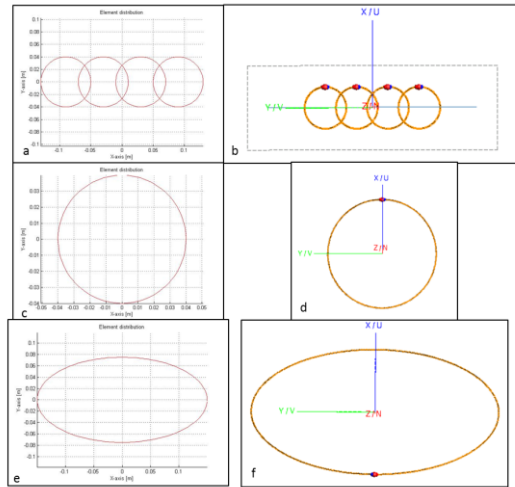- Configuration c: single large 30 x15 cm oval coil.

Figure 2.4- Configurations implemented for script validation. (a) Matlab configuration a. (b) FEKO configuration a. (c) Matlab configuration b. (d) FEKO configuration b. (e) Matlab configuration c. (f) FEKO configuration c.

The parameters used for defining the loops in Matlab scripts were:

- Frequency: 123.2MHz

- Current: 1 A

The field request had the following parameters:

- X axis – inferior limit: -20cm; superior limit: 20 cm; step size: 0.1cm;

- Y axis – inferior limit: 0cm; superior limit: 0 cm; step size: 0.1cm;

- Z axis – inferior limit: 8cm; superior limit: 8 cm; step size: 0.1cm.

For the simulations performed in FEKO, a series of adjustments had to be made to obtain the same conditions as in the Matlab ones. First, each individual loop was modelled using the required radius. Using a custom meshing for the simulations, we defined a wire diameter of 0.0006m (similar to AWG16 copper wire) and a wire segment length of 0.001m. A DC voltage source supplying 1V was placed at the middle of each loop.

For all configurations, a power scaling was necessary in order to achieve 1A current in each loop due to radiation losses. In configuration a, the total source power supplied without mismatch was 0.0132W. Furthermore, for configuration c the scaled power was 2.25W.

2.1.2.2 Proposed configurations

Further simulations of the B_1 magnetic field sensitivity profile were performed for further comparison with MRI tests.

A cylindrical phantom was modelled using the parameters presented in the table below.

Table 2.2- Phantom characteristics for FEKO.

Characteristics	Value
Radius	80 mm
Height	100 mm
Relative permittivity (ε_r)	36 F/m
Conductivity (σ)	0.73982 S/m
Mass density (ρ)	1030 kg/m^3
Loss tangent (tan δ)	0.657 dB/m

Each loop was modelled as a rectangle, including a voltage source, matching and tuning capacitor for achieving the required tuning and matching conditions (Figure 2.5). The loop was tuned using a capacitor (C_{tune}) to 123.2MHz and matched using capacitors (C_{match}) to 50 Ω. To facilitate the implementation of tuning and matching circuits a rectangular shape was preferred instead of an oval one. A voltage source providing 1V was implemented in each loop. The loop was placed at 3mm from the phantom, in order to mimic the thickness of the plastic former. The meshing was realized using surface equivalence method with triangles of 25mm, wire length of 5mm and wire segment length of 6mm.
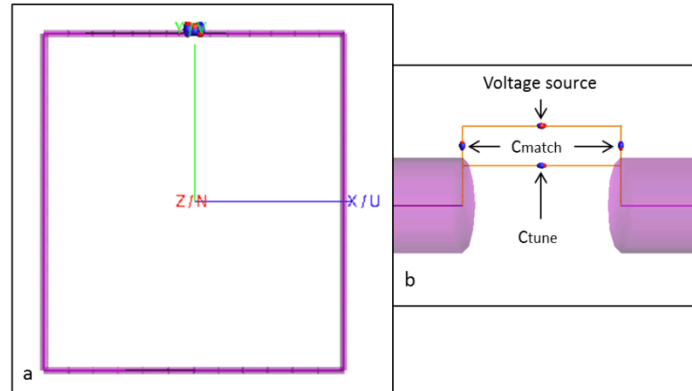
Figure 2.5- Loop definition FEKO. (a) Rectangular loop (width 50mm, height 56mm). (b) Zoomed view of the tuning circuit (C_{tune}) and matching network (C_{match}) powered by a DC voltage source.

To determine the optimal configuration, we proposed 4 array configurations (Figure 2.6): 1 loop , 2 loops, 4 loops and 6 loops made of loops with similar sizes as presented before (50x56 mm). For each configuration, we made a field request inside the phantom for the magnetic field intensity and a frequency response analysis of each loop.
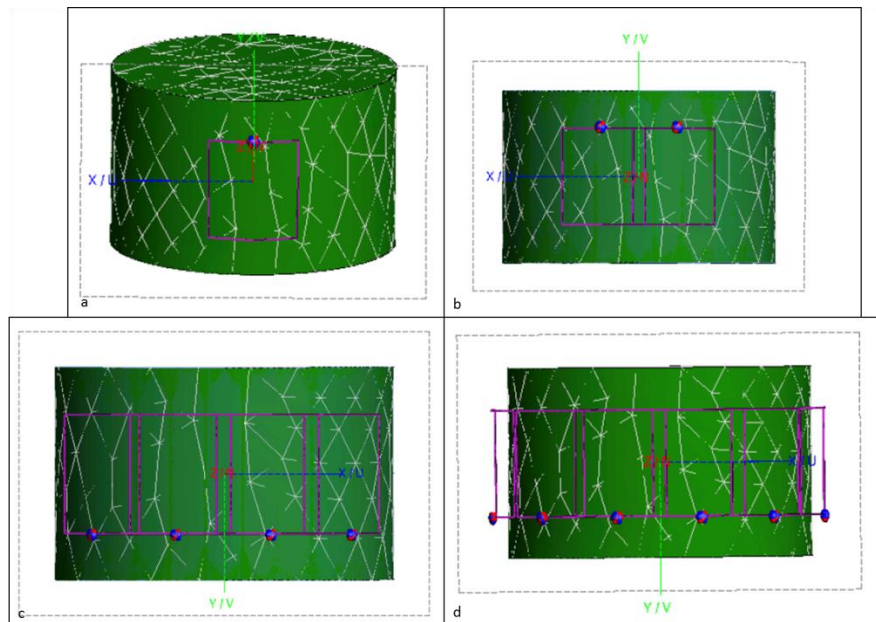

Figure 2.6- FEKO coil configurations. (a) Single rectangular coil. (b) Two - channel array. (c) Four-channel array. (d) Six-channel array.

2.2 Coil design

The coil design had two major sections the mechanical design and the electronic design.

2.2.1 Mechanical design

The first phase of the coil design consisted of creating a complete 3D model of the coil including a human phantom and the scanner interface. The mechanical design was developed using Solidworks (Version 2014, Dassault Systèmes S. A., Vélizy, France) and Sketchup (version 2014, Trimble Navigation Ltd., Sunnyvale, California, USA).

To begin with, a 3D model (Figure 2.7) obtained from MRI images was used to create a human phantom necessary for designing the neck former. The human model contained full anatomy of a human head and neck, including the brain and the spinal cord. The subject parameters corresponded to an average adult human (Nguyen, Simard-Meilleur, Berthiaume, Godbout, & Mottron, 2012). The final phantom had the following parameters:

- Dimensions of the head: 268.74 mm in height,181.20 mm in width;

- Dimensions of the neck: 138.74mm in width; At the C2-C4 vertebral levels, the center of the spinal cord located at 56mm inside the neck region. The diameter of the spinal cord is 12mm.
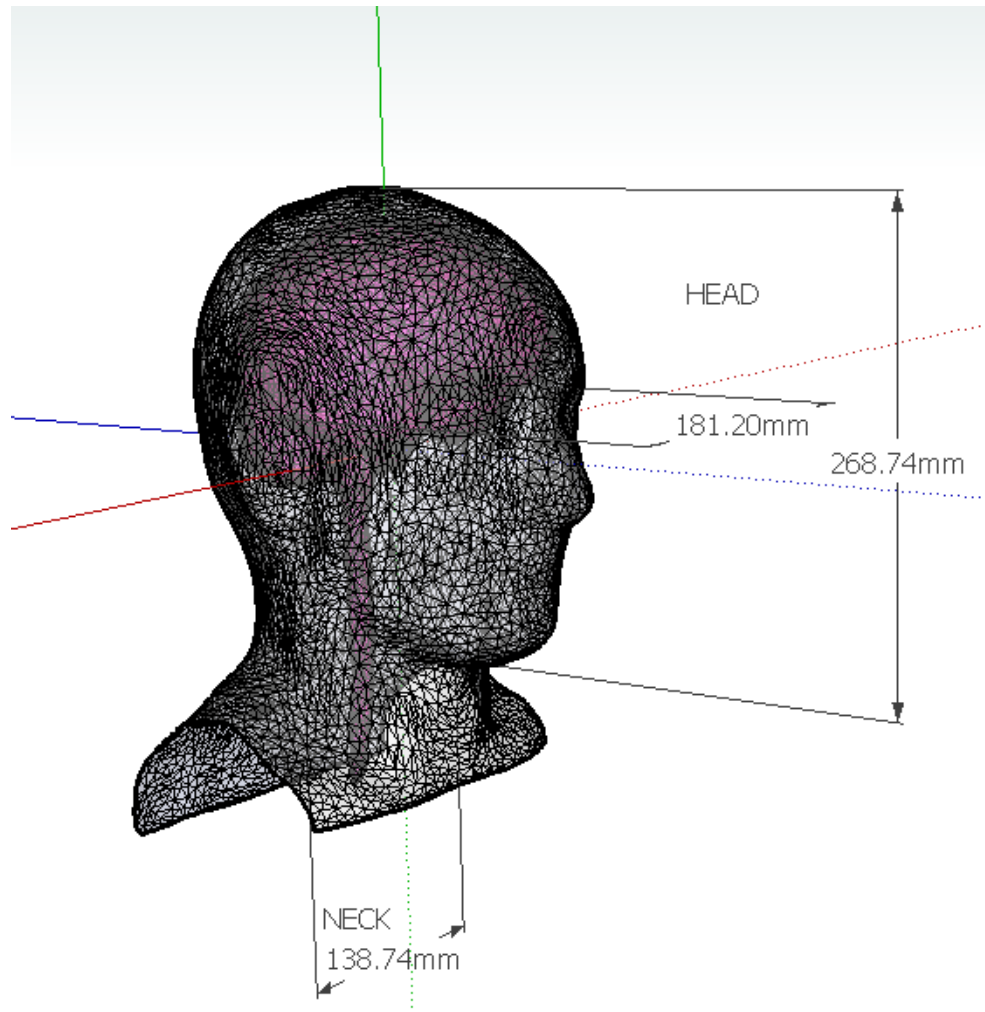
Figure 2.7- Human head and neck model obtained from MRI images. Source : (Cohen-Adad, Mareyam, Keil, Polimeni, & Wald, 2011a).

In order to accommodate a wide population the proposed neck holder had a diameter of 160mm (Figure 2.8). The neck holder has a length of 90 mm offering a full coverage of the neck starting from the lower brain as low as the C6 vertebral level. The cylindrical shape of the holder was printed using polylactide plastic. The neck former was tested on 5 individuals. The former was large enough to fit all the subjects.
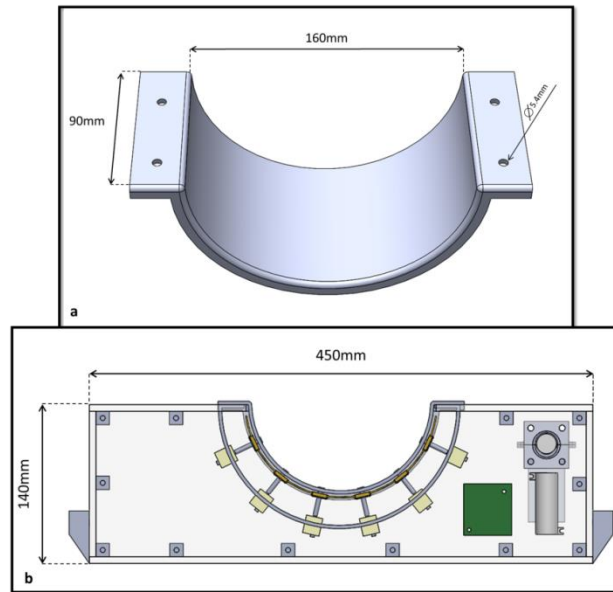
Figure 2.8– 3D model of coil housing. (a) Detailed view of the neck holder. (b) Detailed frontal view of the coil holder.

In addition, a 3D model of the patient table was used to develop the coil housing. The coil housing was designed to fit the patient table and to offer a high degree of comfort to the human subject. The RF coil is planned to be used by itself.

The neck former, the cable support and side fixing system were printed in polylactide (PLA) using a rapid prototyping three-dimensional printer (Big Builder Dual-Feed Extruder, 3Dprinter4U, Netherlands). The housing box is made of 5mm polycarbonate (Figure 2.9).
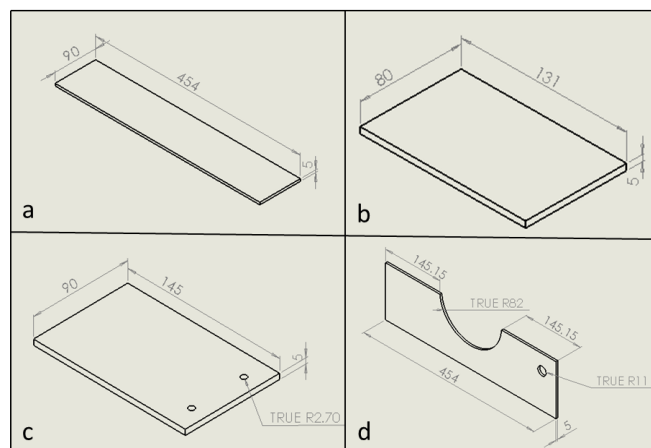

Figure 2.9- Isometric view of the coil housing parts. (a) Bottom panel. (b) Side panel. (c) Top panel. (d) Front panel. Dimensions given in mm.

Careful attention was paid to the mechanical stability of the complete structure (Figure 2.12). A side fixing system attached to the coil housing locks in place the coil on the patient table (Figure 2.11). Moreover, in order to limit the mechanical tensions in the output cables, the coil has a set of cable supports (Figure 2.10). One of the cables supports helps fixing the output cable of each preamplifier on a plastic ribbon structure. The second cable support is used to fix the main cable that connects the coil to the scanner.
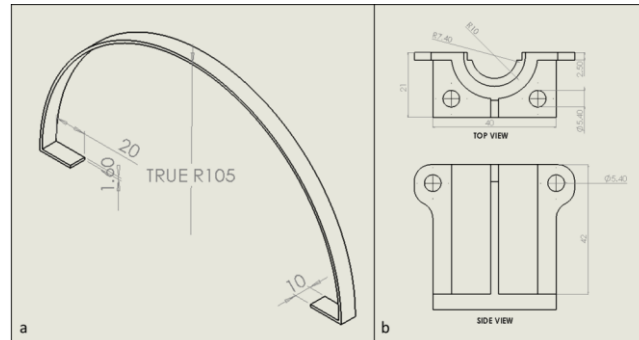

Figure 2.10- 3D model of the cable support. (a) Isometric view of the cable support for the preamp output. (b) Cable support for the MRI connector. Dimensions given in mm.
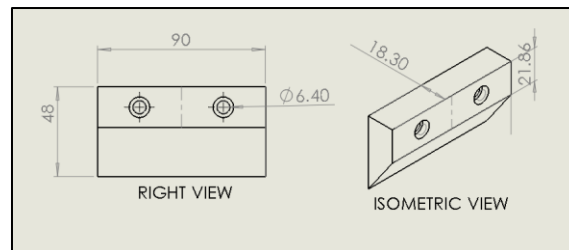

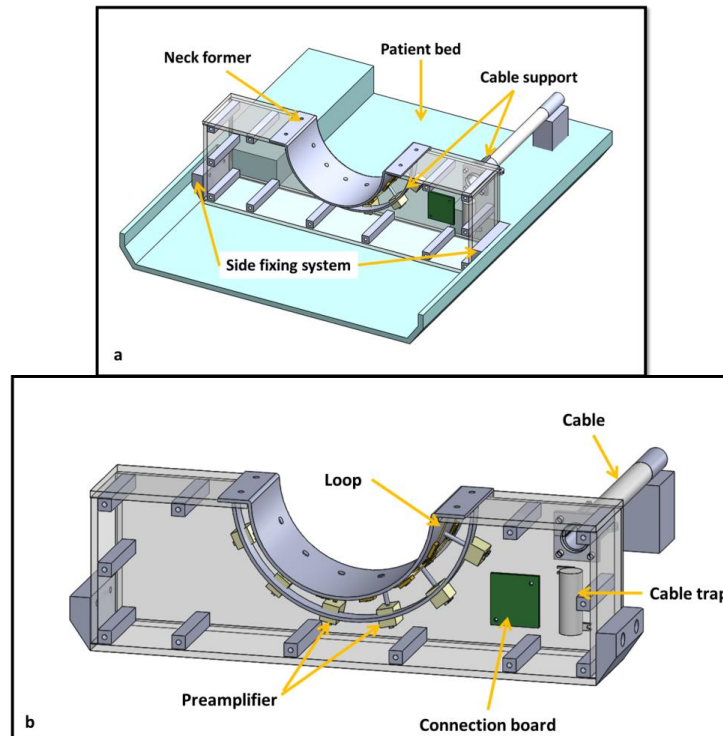Figure 2.11- Side fixing system. Dimensions given in mm.

Figure 2.12- Illustration of coil assembly. (a) 3D model of the coil holder and electronics mounted on the patient table. (b) Detailed view of neck coil including housing and electronics.

2.2.2 Electronic circuit design

2.2.2.1 Circuit parameters

Using the results of the electromagnetic simulations, the configuration that was built is formed of 6 elliptical loops with the following dimensions 27.5mm x 30mm in radius. Each loop was symmetrically divided in two sections. The coil can be regarded as a RLC circuit, consequently a series of discrete components had to be determined in order to achieve the proper performance objectives (Figure 2.13).
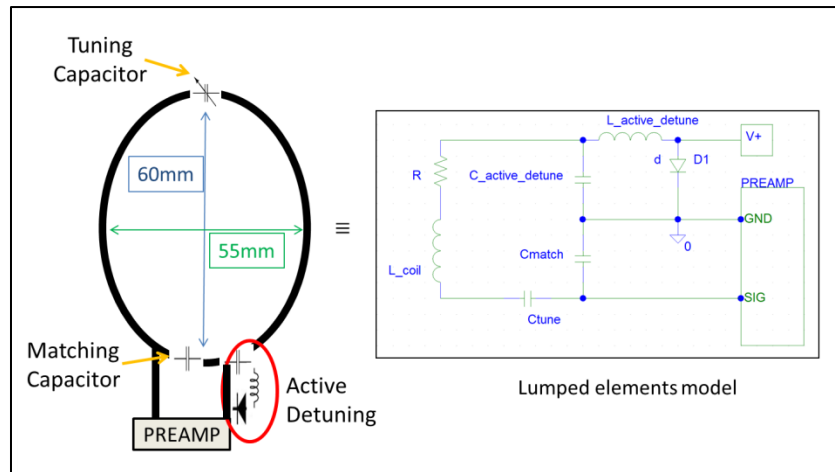
Figure 2.13 - Illustration of the elliptical loop and the equivalent lumped element model.

To begin with, the inductance of the loop was measured using the network analyzer performing a S_{11} measurement. The impedance of the loop was determined for two matching conditions: loaded with a water phantom and unloaded. The obtained touchtone file was exported for further use in circuit characterization.

Using electronic circuit design software (Advanced Design System (ADS) version 2015, Keysight Technologies Inc., Santa Rosa, USA) the impedance of the loop was approximated (Figure 2.14), resulting in an inductance of 179.12nH and a resistance of 2.7Ω for unloaded conditions and 4.3Ω for loaded conditions (Figure 2.15).
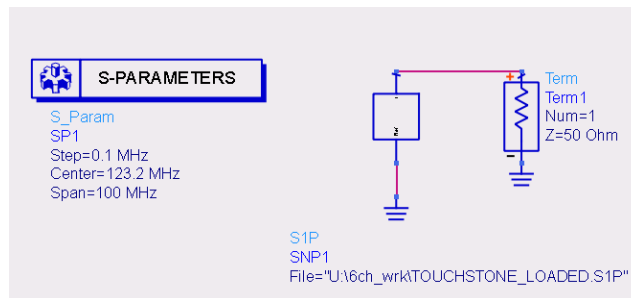

Figure 2.14– Screen caption impedance approximation using ADS.
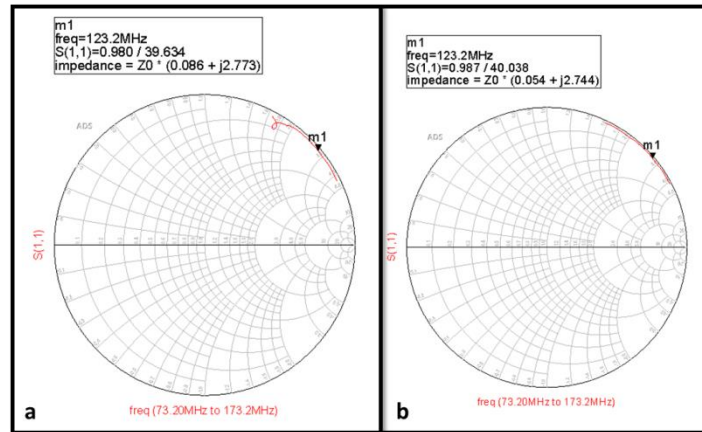
Figure 2.15- Impedance of the elliptical loop. (a) Loaded coil. (b) Unloaded coil.

2.2.2.2 Tuning

The coil can be regarded as an RLC circuit which has a resonant frequency (ω_0) when the resonant condition is satisfied:

$$LC\omega_0{}^2 = 1 \tag{2.18}$$

Where L is the inductance, C is the capacitance.

A complete model for the circuit was implemented in PSPICE (Cadence Design Systems, Inc., San Jose, California, USA) and ADS. Using the measured inductance of a loop, the capacitance value was simulated in order to satisfy the resonant frequency.

Figure 2.16- PSPICE circuit model for tuning frequency.

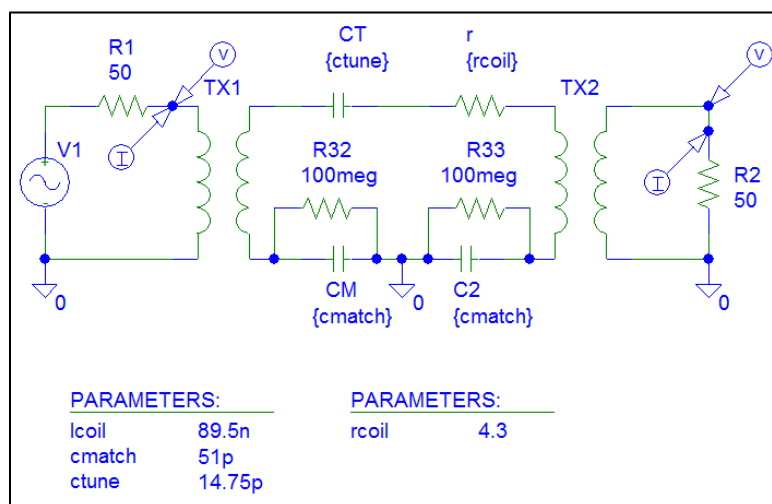The coil was modelled in PSPICE using distributed capacitance for tuning (Figure 2.16). The proposed circuit for the assessment of the resonant frequency replicates the behavior as a double loop probe measurement. The double loop probe is modelled as a series of transformers and a voltage source.

The coupling factor used in the transformers was 0.033. The return loss off the modelled double loop probe can be calculated using additional voltage and current probes.

The return loss is represented by the loss of power in the signal returned by a mismatch in the transmission line (Figure 2.17).
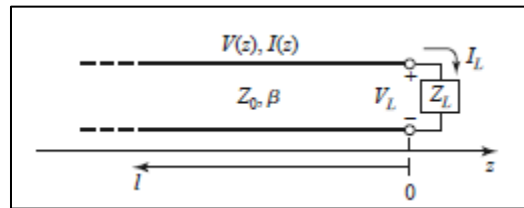
Figure 2.17- Transmission line terminated with a load impedance. Source : Pozar, 2009

Using the transmission line model the input return loss (RL) is defined as (Pozar, 2009):

$$RL = -20 \; |\Gamma| \; [dB] \tag{2.19}$$

Where Γ represents the voltage reflection coefficient.

$$\Gamma = \frac{V_o^-}{V_o^+} = \frac{Z_L - Z_0}{Z_L + Z_0} \tag{2.20}$$

In our case the voltage reflection coefficient of a S_{21} measurement can be written using the voltage and current information as:

$$\Gamma = \frac{V_o^-}{V_o^+} = \frac{V(R1) - R1 * I(R1)}{V(R2) + R2 * I(R2)} \tag{2.21}$$

In order to tune the elliptical loop to the desired frequency (123.2MHz) the value of the tuning capacitor was found to be 14.75pF. Moreover, the resultant return loss is illustrated below (Figure 2.18).

Figure 2.18- PSPICE screen shot of S_{21} measurement for the tuning frequency.

Using a similar circuit model, the frequency response was analyzed in ADS (Figure 2.19).

Figure 2.19- ADS model of tuning circuit.

In this case the required tuning capacitor was found to be 13.96pF, having a close value to the one obtained using PSPICE (Figure 2.20).
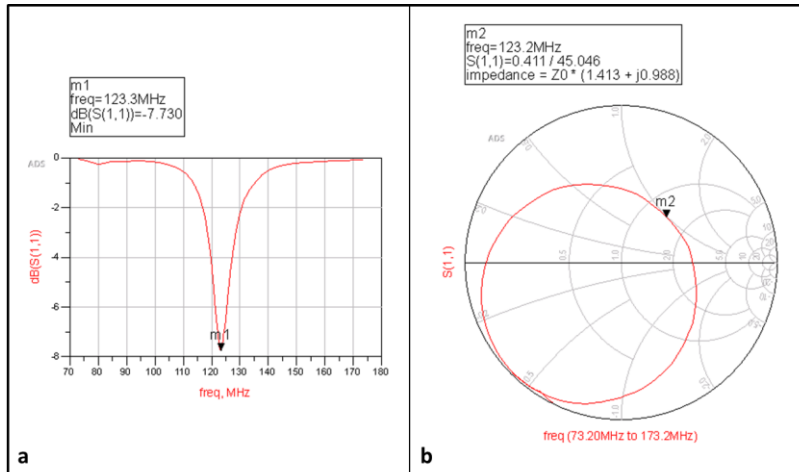
Figure 2.20- ADS screen shot of frequency response. (a) S_{11} linear plot. (b) S_{11} polar plot.

2.2.2.3 Impedance matching

The input impedance of the RLC circuit varies (Z_L) and it needs to be adapted to purely resistive characteristic impedance Z_0.
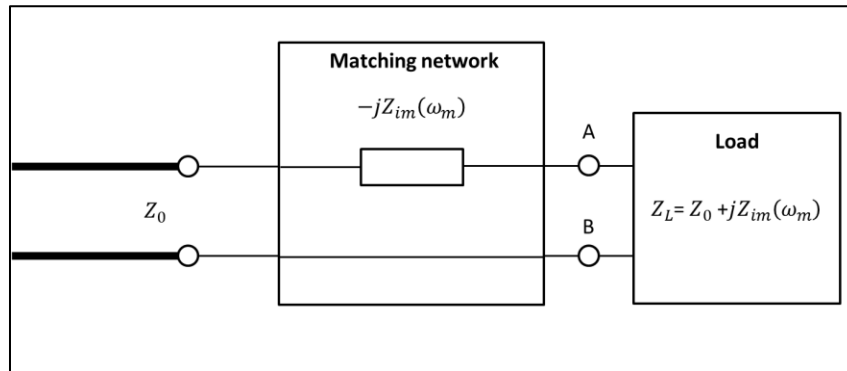

Figure 2.21- Block diagram illustrating impedance matching.

The impedance matching helps improving the signal to noise ratio of the system. A proper impedance matching ensures maximum power transfer between the load to Z_0 thus limiting the reflected power in the feed line. In order to satisfy the impedance matching conditions for a resonant frequency ω_m, the resistive impedance at port AB needs to be equal to Z_0 (Figure 2.21). In addition, if there is a reactive component at the given frequency, it has to be canceled by adjustable conjugate impedance (Pozar, 2009):

$$jZ_{match} = -j[Z_{im}(\omega_m)] \tag{2.22}$$

A series of strategies have been developed for improving the impedance matching such as capacitive coupling, inductive coupling or tapping point coupling (Mispelter, Lupu, & Briguet, 2006).

In our case, the impedance that needs to be matched (Z_0) was defined by the required input impedance for the effective noise impedance matching of the preamplifier. In the current design a low noise preamplifier MPB-123R20-00 (HI-Q.A. Inc., Canada) was used.

Table 2.3- Preamplifier specifications. Source: Preamplifier datasheet.

Parameter	Value	Unit
Center Frequency	123.2	MHz
Adjustable gain range (S21)	25 (min) to 32 (max)	dB
Input Z – Real (S11)	1.4 (typ) 1.6 (max)	Ohm
Input Z – Reactive Range (S11)	+j3 to +j32	Inductive Z
Noise Figure	0.5 (typ) 0.55(max)	dB
Current Consumption	<8	mA

The manufacturer recommends an impedance matching to the characteristic impedance in the range 50 to 200Ω without an important impact on the noise figure. Moreover, the input impedance has a reactive part which can be used for building the matching network, thus reducing the number of components.

In order to enhance the flexibility of fixing the circuit board, we have added a semi-rigid coaxial cable (UT-85C-FORM-LL, Micro-Coax Inc., Pennsylvania, USA) between the output of the coil and the preamplifier input. The length of the semi-rigid cable was 40mm and the measured inductance was 14.35nH having a short-circuit ending (Figure 2.22).
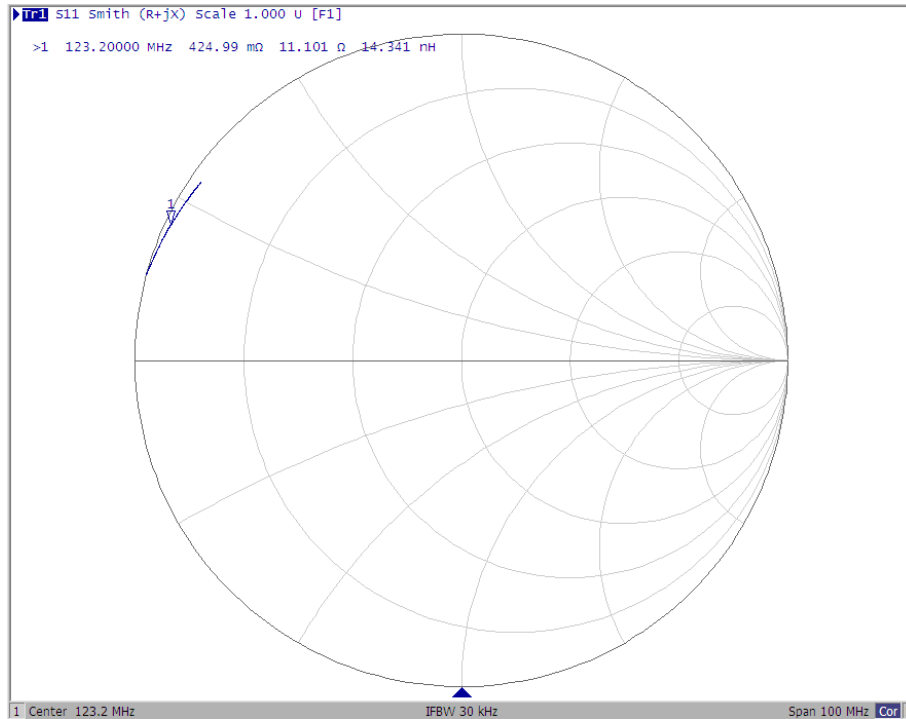
Figure 2.22- Coaxial cable S_{11} measurement for center frequency - 123.2MHz, span-100MHz.

2.2.2.3.1 Matching network

The matching network is based on an L-section or lumped matching network (Figure 2.23). The L-nework consists of two reactive elements used to match arbitrary load impedance to a transmission line with characteristic impedance Z_0. In order to determine the components for the L-network, the normalized load impedance has to be computed $z_L = Z_{coil}/Z_{preamp}$. In our case the normalized load impedance is located inside the 1+jX circle in the impedance Smith chart (Pozar, 2009). Consequently, the L-network contains a series reactive part and a shunt susceptance part.
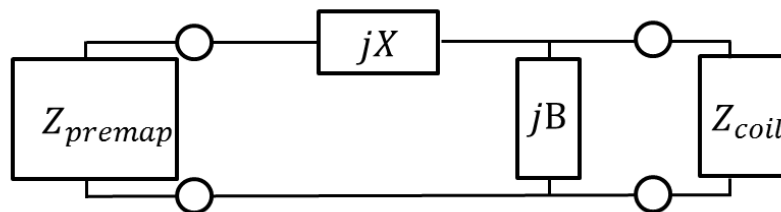

Figure 2.23- Lumped matching network for Z_{coil} inside the 1+jX circle of the impedance Smith chart. Source : (Pozar, 2009)

The characteristic impedance Z_{preamp} of the preamplifier varies from 50 to 200Ω. The proposed L-matching network was formed of a series coaxial cable which has a similar behavior as an inductor and a shunt capacitor in order to adjust the matching conditions (Figure 2.24). The length of the coaxial cable was empirically determined in order to satisfy the impedance matching condition.
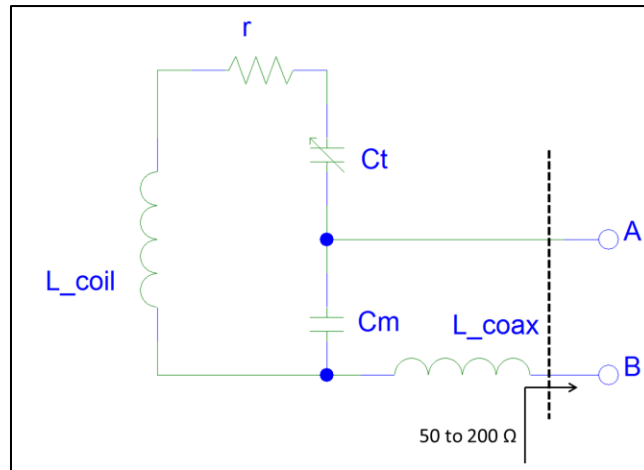

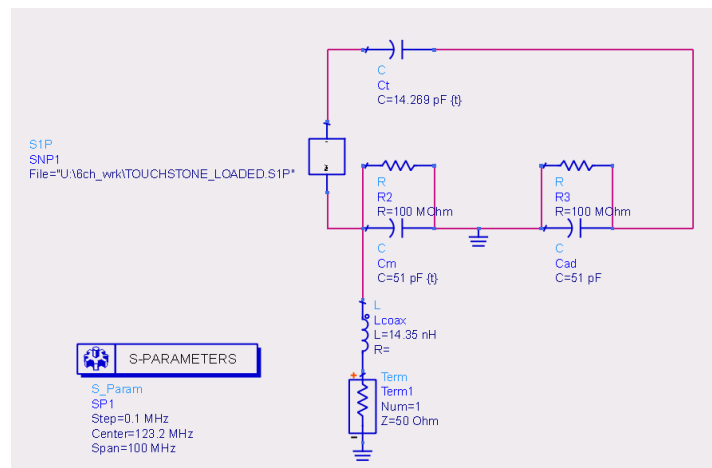Figure 2.24- Coil with impedance matching network.

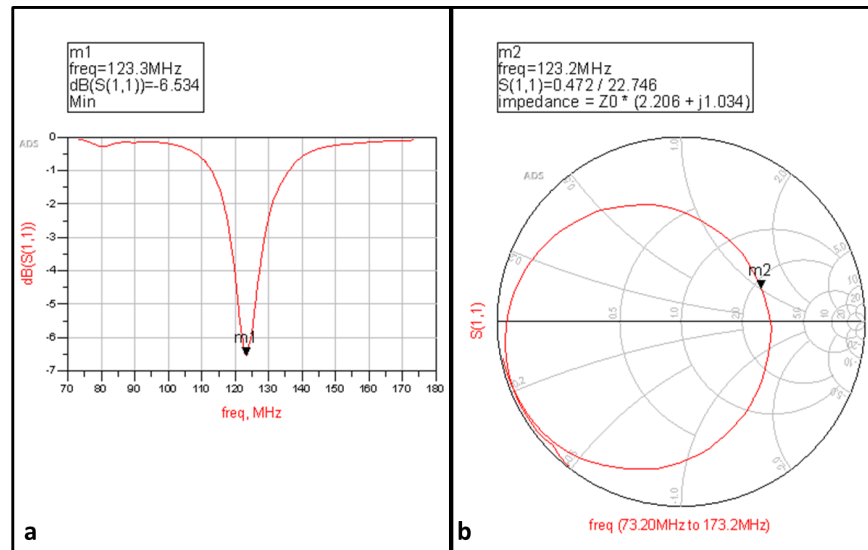Figure 2.25- ADS model of tuning and matching circuits.

Figure 2.26- ADS screen shot for frequency response of the matching circuit.

The values obtained for the matching network were 51pF for the shunt capacitor and 14.35nH for the series inductor (Figure 2.25). The impedance simulated at the output of the matching network was 110.3+51.7j Ω, which is in the required range (Figure 2.26).

2.2.2.4 Active detuning

2.2.2.5 Active detuning

During the transmit phase, the receive coil should not disturb the B_{1+} field. This can be achieved by limiting the currents which circulate in the coil induced by the transmit field to negligible levels. The current can be limited if the total impedance of the coil loop is very high. One way of presenting a high impedance of the coil during the transmit phase is to use an active detuning circuit (Figure 2.27).
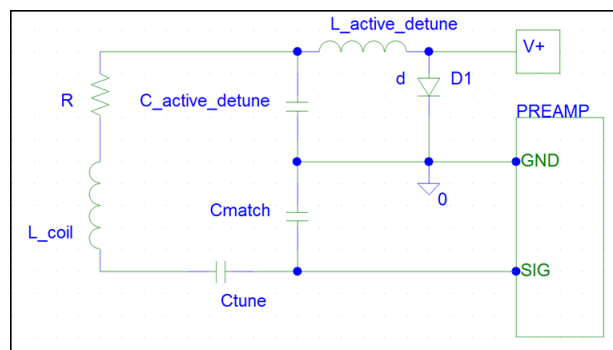

Figure 2.27- Active detuning circuit.

The active detuning circuit is composed of a capacitor in series with an inductor which forms a resonant circuit tuned to the Larmor frequency (123.2MHz). The circuit is controlled by a PIN diode which is activated during the transmit phase. When the PIN diode is forward biased, the resonant circuit will insert high impedance in series with the coil, thus blocking the current at the Larmor frequency. The high impedance prevents receiver circuitry damage and possible injury of the patient due to the use of high power pulses.

PSPICE simulations were used to determine the components of the active detuning circuit (Figure 2.28). The modelled circuit was based on the tuning circuit. Using the values obtained for tuning and matching the coil, the active detuning circuit consists of an inductor of 32.65nH and a capacitor of 51pF.
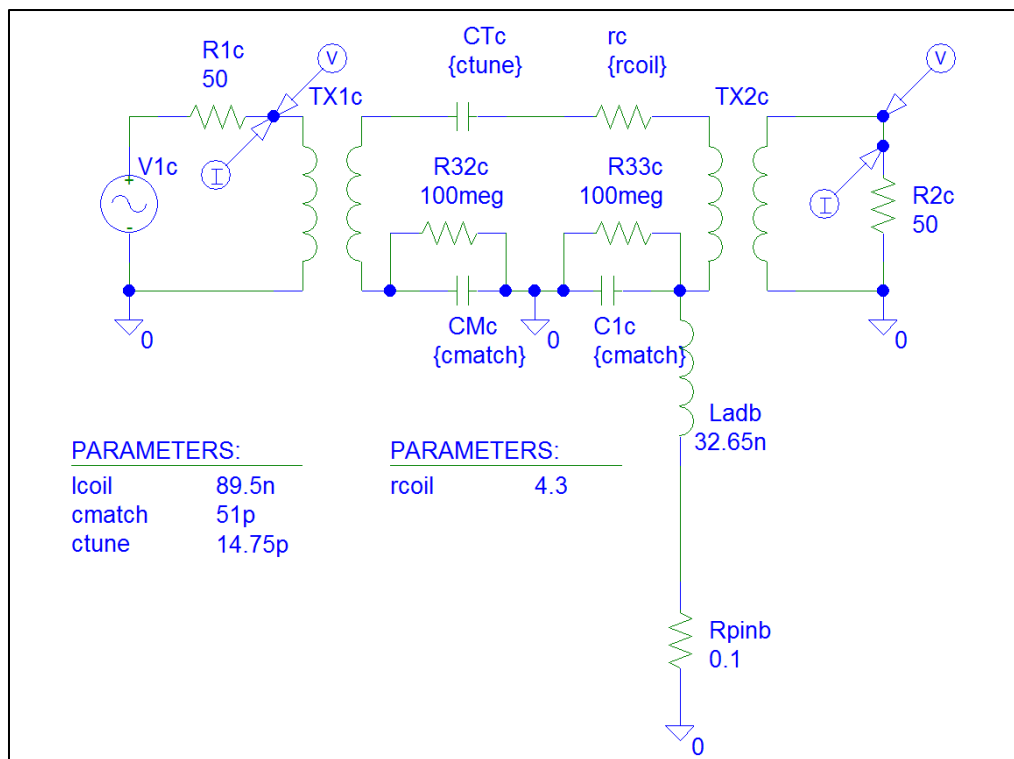

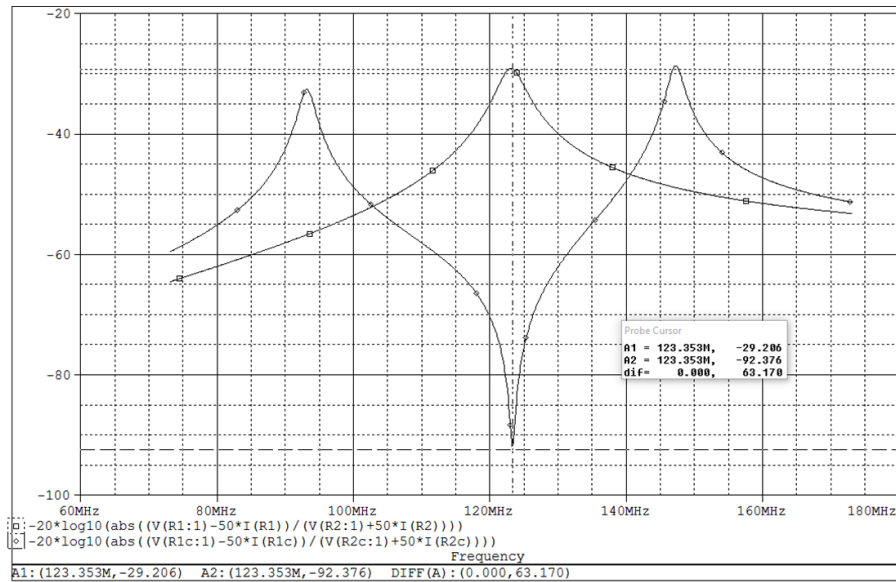Figure 2.28- PSPICE model of active detuning circuit.

Figure 2.29- PSPICE screen shot of S_{21} measurement of active detuning response.

The active detuning level represents difference between the maximum S_{12} when the coil is tuned and the minimum S_{12} when the coil is detuned (Figure 2.29). The purposed circuit provides a difference of -63.17dB, which corresponds to the values from the literature i.e. <-35 dB (Keil, 2013; Kyle M. Gilbert & Menon, 2015).

2.2.2.6 Inductive decoupling

The coil elements of an array depending on their positioning will have different levels of coupling. Coupling between coil elements will cause signal crosstalk, thus reducing the uniqueness of the signal sensitivity profile. Depending on the source which generates the coupling, it can be divided in resistive coupling, capacitive coupling and inductive coupling (Riccardo Lattanzi, Ryan Brown, & Kaveh Vahedipour, 2015).

The resistive coupling is described as the resistance between two elements caused by electric field through the sample volume characterized by a specific conductivity (σ).

$$R_{ik} = \int_{sample} \sigma(r)E_i(r) \cdot E_k(r)dv \qquad (2.23)$$

Where $\sigma(r)$ represents sample conductivity, E_i is the electric field generated by coil i, E_k is the electric field generated by coil k, *dv* is the sample volume.

The inductive coupling (Figure 2.30) is a result of the magnetic field interactions of neighboring coil loops. Due to the currents which are circulating in the loops, a magnetic field is produced. Two neighboring loops act as a transformer presenting a mutual inductance. This type of interaction causes changes in frequency response and degrades their sensitivity profile. The inductive coupling between two coils can be approximated using the coupling coefficient (k) varying from 0 e.g. no inductive coupling and 1 e.g. maximum inductive coupling. (Smythe & Smythe, 1950)

Furthermore, one can express the coupling coefficient (k) as:

$$k = \frac{M}{\sqrt{L_1 L_2}} \tag{2.24}$$

Where M represents the mutual inductance expressed in Henry.
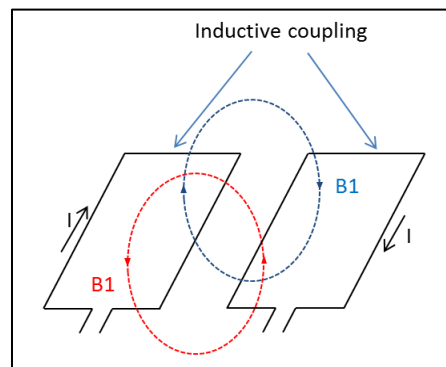
Figure 2.30- Illustration of inductive coupling between neighboring loops.

Depending on the loop geometry, the inductive coupling can affect the SNR of the array. (Roemer et al., 1990). In case of adjacent loops, the overlapping between them can be adjusted in such a way that the mutual inductance is reduced to zero. Depending on the geometry of the loop, a critical overlapping ratio was determined empirically (Roemer et al., 1990) (Figure 2.31).
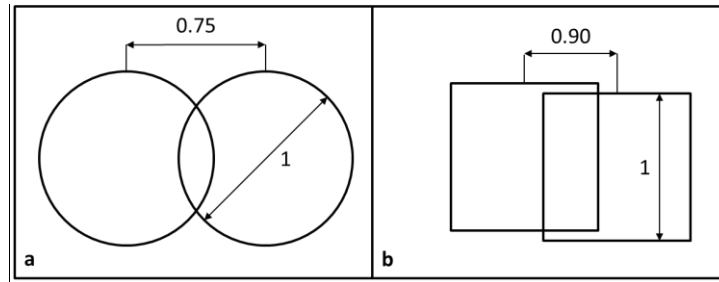
Figure 2.31- Critical overlapping for reducing the mutual inductance. (a) Circular loops configuration. (b) Square loops configuration. Source : (Roemer et al., 1990)

In our case, the loops were carefully overlapped to minimize mutual inductance having a ratio close to 0.75 times the coil diameter between neighboring elements.

2.2.2.7 Preamplifier decoupling

On the other hand, the inductive coupling between non-adjacent loops can be controlled by using preamplifiers. Using this method the current circulating in the loop is limited, thus the inductive coupling is reduced despite the presence of residual mutual inductance.
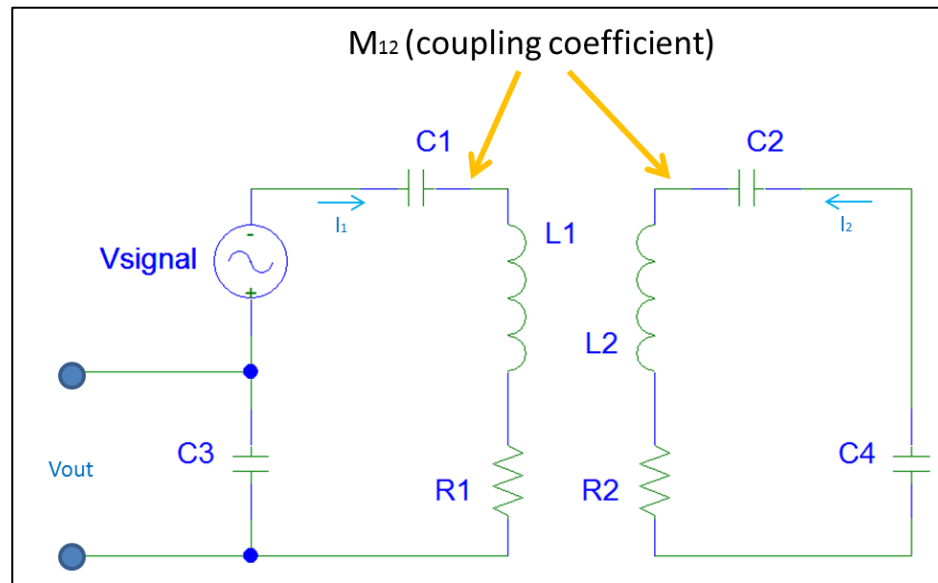

Figure 2.32- Illustration of inductive coupling.

If one wants to characterize the signal at the output of coil 1 (Figure 2.32):

$$V_{out} = V_{signal} - \left(R_1 + i \left(\omega L_1 - \frac{1}{\omega C_1} \right) \right) I_1 + i\omega M_{12} I_2 \qquad (2.25)$$

Since the M_{12} has already been reduced, to cancel the inductive coupling, one imposes $I_2 = 0$. This can be achieved using the preamplifier decoupling technique (Figure 2.33).
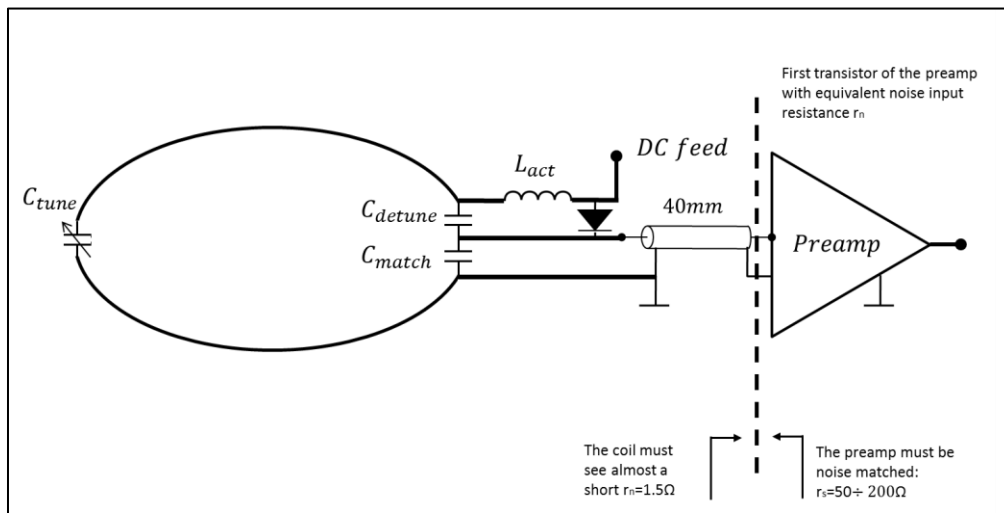

Figure 2.33- Preamplifier decoupling - impedance matching.

The design of the impedance transformation network between the coil and the preamplifier has an important role in achieving the preamplifier decoupling. Firstly, the coil has to see small impedance towards the preamplifier, equivalent to the input resistance of the preamplifier. On the other hand, the impedance seen from the preamplifier towards the coil has to be equal to the impedance required for the proper noise matching. The step-up network (C_{match} and the semi-rigid coaxial cable) creates a series resonance, which will create a short-equivalent, thus blocking the current from flowing in the coil. Having a reduced current circulating in the loops during the reception phase will ensure that the noise and MRI signal are not coupled between other elements.

The assessment of the preamplifier decoupling was initially validated using PSPICE simulations (Figure 2.34). The implemented circuit has taken into account the model of the coil including the coaxial cable and a complete model of the preamplifier. An impedance matching network was implemented in the model of the preamplifier considering the fact that the impedance presented before the first transistor is at the order of 1kΩ. The decoupling level achieved was -31.59dB (Figure 2.35).
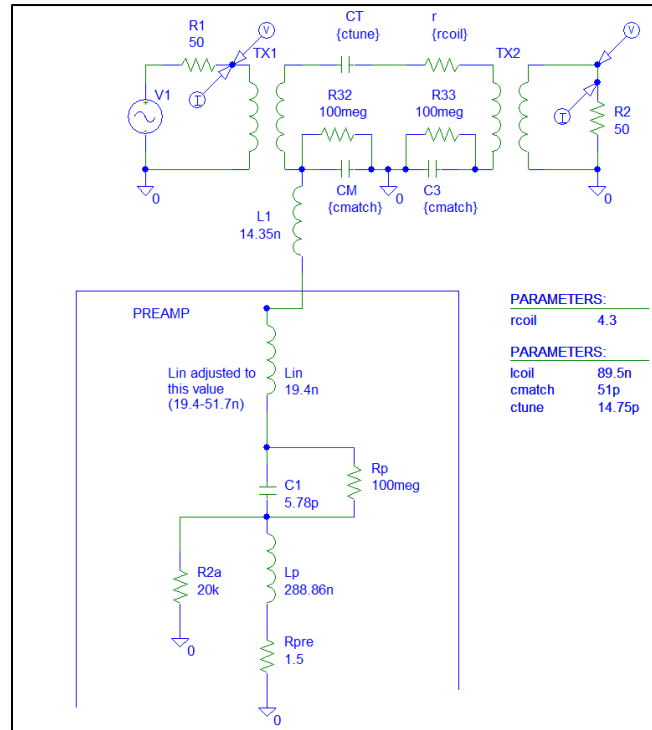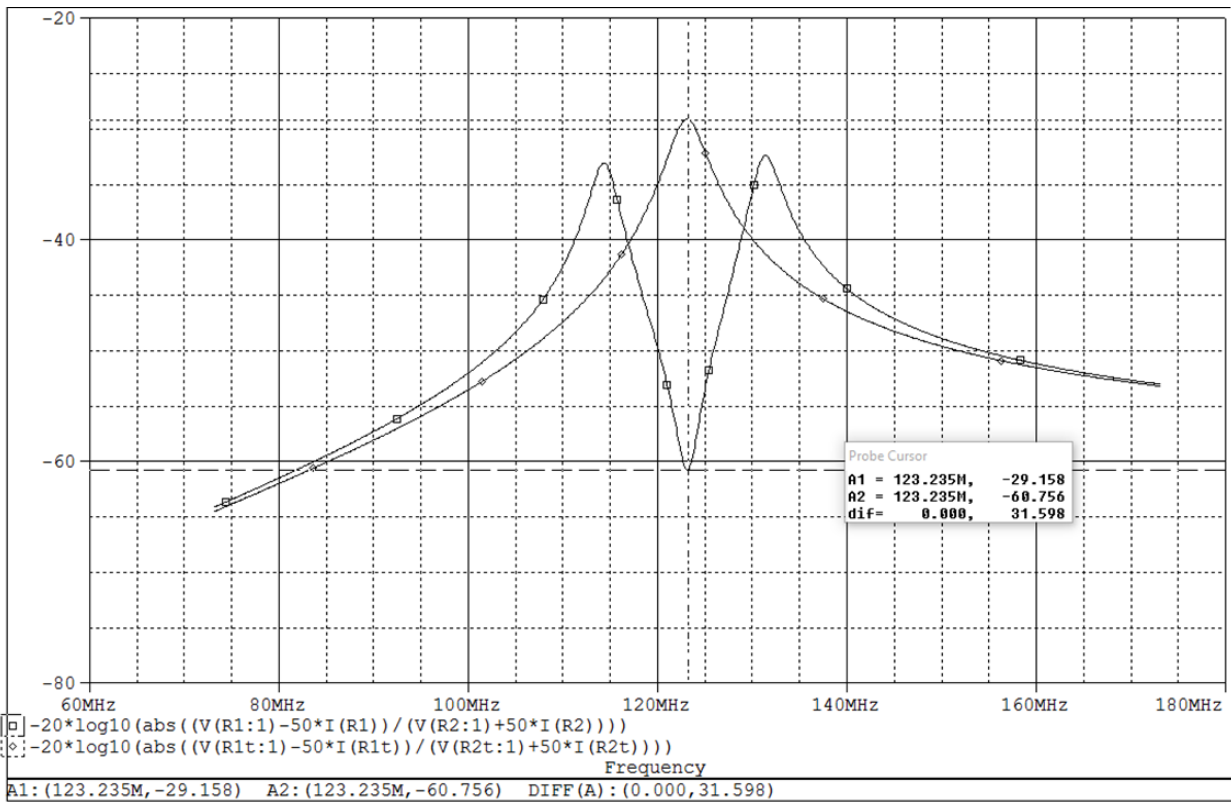
Figure 2.34- PSPICE model of preamplifier decoupling circuit.

Figure 2.35- PSPICE screen shot of S_{21} measurement for preamplifier decoupling.

The preamplifiers were placed outside the FOV to avoid the RF losses due to induced current in the preamplifier socket and the conductive components of the preamplifiers, thus degrading the receive performances. Each preamplifier was mounted at 2 cm from the coil former using a screw fixing system for the preamplifier board. Moreover, all preamplifiers were properly oriented with respect to the B_0 field direction in order to minimize the Hall effect within the transistors of the preamplifier (D. Hoult & Kolansky, 2010; Lagore, Roberts, Fallone, & De Zanche, 2011; Possanzini & Boutelje, 2008).

2.2.2.8 PCB design

All electronic circuits were printed on circuit boards (PCB) using RO4350 substrate (Rogers Corporation, Connecticut, USA). This substrate was preferred due to its low loss tangent, which is an important characteristic for RF circuits. Each individual loop had two printed circuit boards. The first one hosted the matching and the active detuning circuit. The second board was used for installing the preamplifier socket (Figure 2.36). The output of all channels were linked to the MRI connector using a connection board. The connection board provides the DC feed lines, which are protected using a low pass filter used for separating the RF from the DC (Figure 2.37). In addition, the footprints for the resistors necessary for the coil code are hosted in the left side.
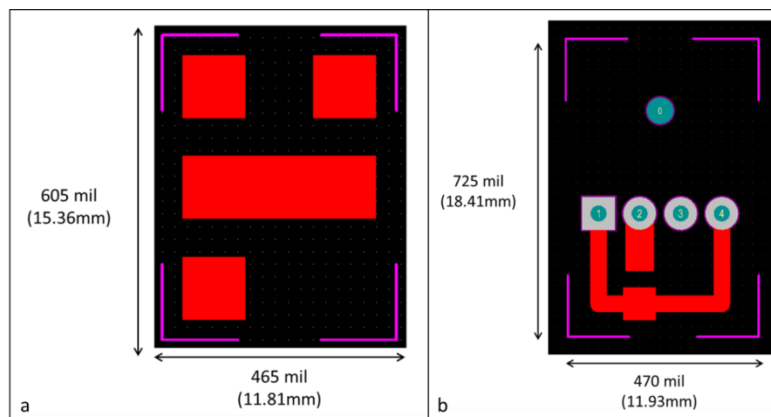

Figure 2.36- PCB design. (a) The PCB used for matching and active detuning circuit. (b) Preamplifier socket board.
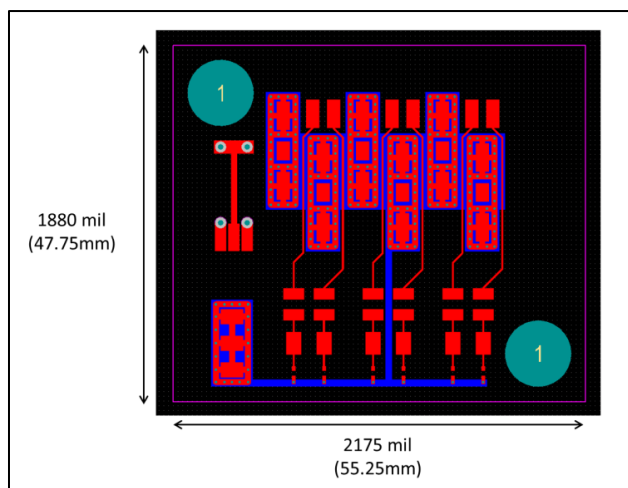
Figure 2.37- PCB design for the connection board.

2.2.2.9 MRI connector

The array is connecting to the MRI scanner using a custom plug. The Siemens Trio scanner has 6 plugs offering 32 receive channels and 1 transmit channel independent from the body coil (Figure 2.38).
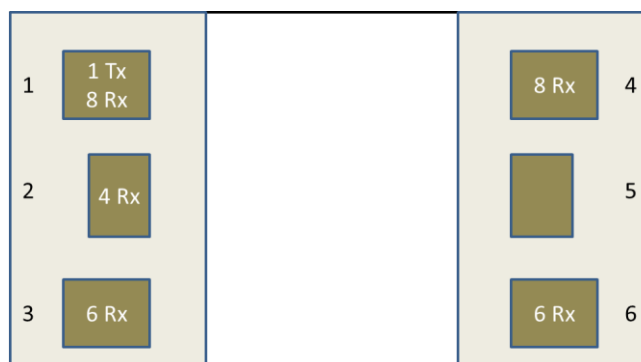
Figure 2.38- Schematics of the patient table with the plug disposition.

For a good mechanical fixation of the cable, the plug number 4 was chosen.

The connector installed on the patient is a female plug. The connector mounted on the cable has a male ending. A 6-channel cable was used to connect to plug 4. The male connector has individual pins for every pin diode signaling, a common ground for each two pin diodes, RF output for each channel and additional pins used for coil coding.

The coil code was realized with non-magnetic resistors. The coil code is required by the system in order to recognize the type of coil connected. The manufacturer of the MRI scanner, in this

case Siemens, provides unique coil codes for custom build coils. The code is composed of 2 symbols coded in HEX format using different ranges of resistance for each value.

The outputs of every channel are connected on the connection board with the main cable. In order to isolate the DC current used for feeding the PIN diodes from the RF signals, a low pass filter is implemented in the feeding network of the diodes.

A cable trap is used in the cable plug to cancel the common mode currents circulating in the exterior shield of the coaxial cables. The common mode currents can cause interactions in the RF transmission system. The cable trap is formed of an inductor with a capacitor in parallel. The inductor is realized using the shielding of the connection cable. A high voltage ceramic capacitor is used to form the cable trap.

2.2.3 Water phantom

A water phantom was built for simulating the loading conditions of the coil. The dielectric properties of the phantom mimic the parameters of an average human body tissue. The recipe of the phantom was obtained using an online calculator (Advanced MRI section, 2015) based on a study on the characterization of a dielectric phantoms for high-field used in magnetic resonance imaging applications (Duan et al., 2014). The dielectric parameters are controlled using salt for conductivity and sugar for permittivity. The mixture for the phantom was placed in a 2L plastic bottle.

Table 2.4- Phantom recipe and characteristics.

Gel characteristics	Value
Conductivity [S/m]	0.7
Permittivity	50
Resonance frequency [MHz]	123.2
Temperature [°C]	24

Ingredients	
NaCl[g]	140.126
Sugar [g]	1655.105
Water [g]	970
Estimated conductivity [S/m]	0.699
Estimated permittivity [F/m]	50
Estimated final volume [ml]	2008.678
Estimated density [g/l]	1306.88
Estimated heat capacity [(J/g)/K]	2.631

2.2.4 Coil Performance on Bench

The loops were made of AWG16 tin-plated copper wire. Each loop had 2 symmetric arches to facilitate the assembly of multiple loops. Eddy currents in the surrounding elements were avoided using wire loops instead of circuit board material (Kumar et al., 2009). The discrete electronic components had the values obtained from the electronic circuit design simulation. A list of the installed components can be found in the table below.

Table 2.5 - Discrete components of the implemented loops.

Item description	Model number	Company
Non-magnetic chip capacitors	11-510-J-1000-S	Voltronics, Corp., Salisbury, Maryland,USA
Non-magnetic variable inductor	164-02A06L	Coilcraft, Inc., Cary Illinois, USA
Non-magnetic variable capacitors	BFC2808-11229	Vishay XXX Malvern, Pennsylvania, USA
PIN diode	MA4P4002B-402	M/A-COM Technology Solutions, Lowell, Massachusetts, United States

Semi-rigid coaxial cable	UT-85C-FORM-LL	Micro-Coax Inc., Pennsylvania, USA
Preamplifier socket - Connector Receptacle 4 Position 0.100"	0022152046	Molex, Inc., Lisle, Illinois, USA
50 Ohms, MCX Plug, Vertical PCB	73415-2450	Molex, Inc., Lisle, Illinois, USA

Five coil characteristics were optimized for each single coil elements on the bench: element tuning, element matching, element detuning, geometric decoupling and preamplifier decoupling. Setup for the bench measurements consisted of:

- A set of double loop pickup probes with a diameter of 15 mm and 30mm (Figure 2.39); The overlapping between the two loops was adjusted in order to achieve a decoupling level of less than -60dB;

- Support for the double loop pickup probe;

- Network analyzer (E5061B, Agilent Technologies, Santa Clara, California, USA).

Figure 2.39- Double loop probes. (a) 30mm. (b) 15mm.

Prior to all measurements, the network analyzer was calibrated using a calibration for the following parameters:

- Center frequency: 123.2MHz

- Spanning: 100MHz

For a high level of accuracy, the calibration kit was custom built using the same model of BNC connector that was planned to be used throughout all the tests. The kit is composed of a short ending, open ending and a 50Ω load ending (Figure 2.40).
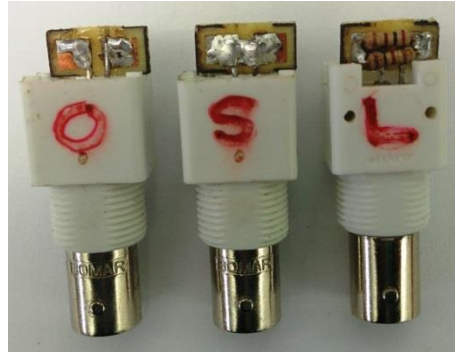

Figure 2.40- Custom built calibration kit. O - open termination. S - short termination. L - 50Ω load termination.

In order to smooth the dynamic of the data measurements, an averaging with a factor of 16 was performed.

Prior to assembling all the channel of the array, a single channel was constructed and characterized for tuning frequency, quality ratio, active detuning, noise matching and preamplifier decoupling.

The preamplifier was selected in order to satisfy the limitations imposed by the scanner manufacturer (Siemens): typical gain of 27dB, supplied preamplifier voltage 10V ± 0.5V, maximum allowed current: n times 70mA for an n-element connector.

Test rig

The assessment of the array was made using a test rig, which mimics the coil plug socket configuration in the MRI scanner (Figure 2.41). The test rig disposed of 32 individual channels with analog signal control. Each channel had a PIN diode controlled by a switch, in order to simulate the transmit/receive phase. The PIN diodes are forward biased with 100mA and reversed biased (-30V) during the reception phase. In addition, a power supply of 10V feeds the preamplifiers. The output of each channel had a BNC connection to provide access to the output signal of the preamplifier.
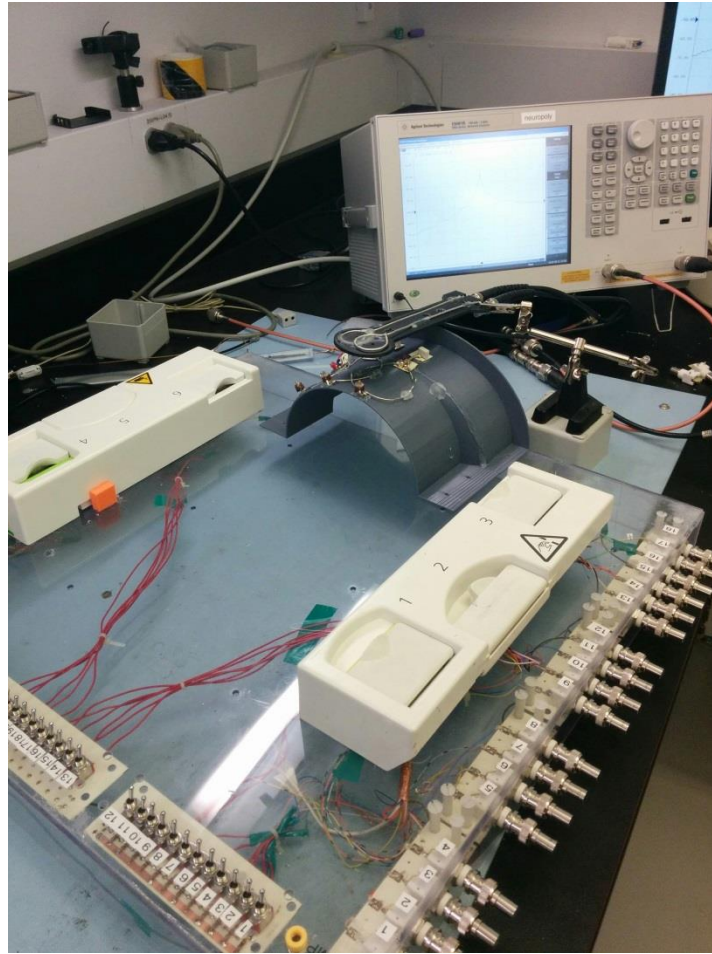
Figure 2.41- Experimental setup: test rig, double loop probe, network analyzer.

2.2.4.1 Tuning and matching

After populating all the elements, the detuning circuits were activated so that only the assessed element remains active. To begin with, the individual loops were tuned to the Larmor frequency (123.2MHz) using variable capacitor C_{tune}. The coil was matched to the required impedance by removing the preamplifier from its socket.

Using the double loop probe fixed using a support at a distance of 1", an S_{21} measurement was performed for loaded and unloaded conditions. The loaded condition is defined by fixing the coil on the coil former and placing the water phantom on it. The resonant frequency (123.2MHz) of the loop was adjusted using the variable capacitor to fine-tune. Maximum peak of the S_{21} is represented by the coil's resonant frequency.

2.2.4.2   Q Ratio U load/unload

The quality factor of a RLC circuit represents the ratio between the energy stored in the circuit and the energy dissipated due to dissipation losses per cycle (Ellis, 2006). The ratio between loaded and unloaded conditions provides estimation for dissipation losses due to sample and to the coil. The most important factors which affect the Q ratio are the coil geometry and the dielectric parameters of the loading. Using the network analyzer, the Q factor spectrum is computed as the ratio between the central frequency to the -3dB bandwidth (i.e. the width of the half maximum of S_{21}).

$$Q = \frac{f_0}{\Delta f} \qquad (2.26)$$

Where f_0 is the central frequency, Δf is the -3dB bandwidth.

For all the S_{21} measurements, a distance of 1" was kept between the double loop probe and the assessed loop using a support. The Q-measurements were performed for an isolated loop i.e. without a coaxial cable or preamplifier.

2.2.4.3   Active detuning

The active detuning was measured for 2 different situations (Figure 2.42). In the first case, the coil was ended with a 50Ω load and the PIN diode is reverse biased. Secondly, the PIN diode was forward biased, thus the loop was detuned. The active detuning represents the difference the first situation response (the peak in S_{21}) and the second one (the deep in S_{21}).
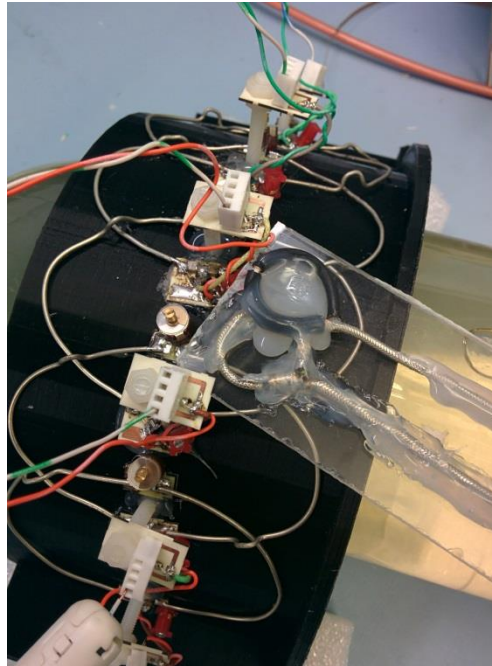
Figure 2.42– Active detuning procedure using double loop probe (all elements detuned)

2.2.4.4 Geometric decoupling

As presented before the geometric decoupling is an important characteristic of the array. Depending on the tuning and matching conditions, the level of coupling between neighboring elements can change. The decoupling was assessed using S_{21} measurement with the cables directly connected to the preamplifier sockets of the two loops. As in the previous cases, channels that were not measured were detuned. The loops were slightly moved and also the wire arches were bent to adjust de decoupling level. The S_{21} measurement was performed having the two coils tuned and matched to 50Ω.

2.2.4.5 Preamplifier decoupling

Having the coil connected on the test rig, we used a double loop probe for a S_{21} measurement using the network analyzer. A distance of 1" between the assessed loop and the pickup probe was kept unchanged during the measurements.

The preamplifier decoupling was assessed using two different matching conditions. The first measurement was made disconnecting the preamplifier and connecting a conjugate impedance of the coil impedance in the socket. In our case, the conjugated impedance was 150Ω. The frequency response shape was similar to the one for the assessment of the frequency adjustment.

For the second measurement, the preamplifier was connected and fed with the required voltage (i.e. 10V, 100mA). The preamplifier decoupling represents the difference between the two responses: the maximum S_{21} peak for the first measurement and the dip in S_{21} for the second one.

Furthermore, the stability of each preamplifier was measured using a S_{21} measurement. A single loop probe was used for exciting each element of the array being connected to the first channel of the network analyzer. The preamplifier output of the tested channel was connected to the second channel of the network analyzer.

A power scaling of -30dB was made to avoid the saturation of the preamplifier. Moreover, an averaging of the displayed data with a factor of 16 was performed in order to smooth the response.

2.2.5 Coil Performance in MRI

The 6-channel coil was developed and tested on a 3-T scanner with 32 receive channels (Trio, TIM System, Siemens Healthcare, Erlangen, Germany) with 40 mT/m maximum amplitude gradient strength and a maximum slew rate of 200 mT/m/ ms (Keil, Alagappan, et al., 2011). Human subjects were scanned after obtaining the review by the institution's ethics committee. The developed coil was compared with a commercially available 4-channel neck array (Siemens) comprised of 2 posterior elements and 2 anterior elements fixed on a detachable paddle. The signals from the 4 elements are combined into 2 physical channels.

2.2.5.1 Phantom imaging

2.2.5.2 SNR maps

To assess SNR, FLASH images of the phantom were acquired in axial and sagittal planes, acquisition time 46.23s, acquisition matrix 384x384, flip angle 10°, slice thickness 5mm, bandwidth 200Hz/pixel. Body coil was used for transmit. Noise covariance information was acquired using the same pulse sequence but with no RF excitation (voltage set to 0).

The computation of the SNR maps is based on the noise-covariance-weighted root sum-of-squares of the individual channel images (Kellman & McVeigh, 2005; Roemer et al., 1990). The ROI was defined at the C4 vertebral level of the spinal cord.

To compare the commercial coil with the custom built coil, the average of SNR was computed in an ROI approximately centered on the spinal cord region.

2.2.5.3 Noise correlation maps

The noise covariance matrix calculations $\Psi_{i,j} = < n_i \cdot n_j^* >$ are based on the SENSE methodology (Pruessmann et al., 1999), where n_i and n_j are the complex noise covariances of the ith, respectively jth coil. Information acquired without RF excitation with the following parameters acquisition matrix 384x384, flip angle 10°, slice thickness 5mm, bandwidth 200Hz/pixel. The final noise correlation was computed using the noise covariance information:

$$\Psi_{i,j}{}^{corr} = \Psi_{ij}(\Psi_{ii} \cdot \Psi_{jj})^{-1/2} \tag{2.27}$$

Where Ψ_{ij} is the noise covariance between coil i and coil j, Ψ_{ii} is the noise covariance of coil i with itself, Ψ_{jj} is the noise covariance of coil j with itself (Keil, Wiggins, et al., 2011).

2.2.5.4 Human subject validation

An adult human subject (male, 26 y.o.) was scanned to assess the sensitivity profile of the custom built neck coil, after the authorization of the institution's human research committee and the informed consent obtained from the subject.

An initial set of images were acquired using 2D FLASH imaging gradient echo in axial cut with 5 mm thickness centered on the C4 vertebral level with the following parameters: TE=6ms, TR=30ms, acceleration R=2, acquisition matrix 384x384, FOV 192*192 mm, bandwidth 200Hz/voxel, voxel size 0.5x0.5x5 mm^3. The whole-body coil was used for RF excitation. The commercial coil was compared to the custom built coil.

An additional set of 2D FLASH gradient echo images was acquired to assess the acceleration capabilities of the custom built coil with the following parameters: TE=12.56ms, TR=539ms, acceleration R=3, acquisition matrix 320x320, FOV 160x160, bandwidth 260Hz/voxel, voxel size 0.5x0.5x5mm^3 , acquisition time 2:17min. The contrast dynamic range of the images acquired with the two coils was compared.

Dynamic spinal cord imaging

Another human subject was used to acquire a set of dynamic images with pulse Ox gating using the following parameters: TE=3.25ms, TR=249ms, flip angle10°, acquisition matrix 256x208, FOV 178x220, bandwidth 407Hz/voxel, voxel size $0.85x0.85x6mm^3$, cardiac number of images 4, acquisition time 8.93 second. These images were used for observing the spinal cord motion at high temporal and spatial resolution, for different phase of the cardiac cycle.

CHAPTER 3   RESULTS

3.1 Simulations

3.1.1 Matlab

Using the developed MATLAB scripts, 4 configurations were characterized:

- Configuration a: single channel circular loop with 6cm radius

- Configuration b: 2 channel array circular loop with 6cm radius

- Configuration c: 4 channel array with circular loop with 3cm radius

- Configuration d: 6 channel array with elliptical loop with 2.75x3cm

Using the theory aspects presented in section 2.1, the request for the B_1 field sensitivity profile and the SNR maps were computed for space defined by:

- X axis – inferior limit: -20cm; superior limit: 20 cm; precision: 0.1cm;

- Y axis – inferior limit: 0cm; superior limit: 0 cm; precision: 0.1cm;

- Z axis – inferior limit: 0cm; superior limit: 40 cm; precision: 0.1cm.

The ROI in the XZ plane was defined using the human phantom to:

- X axis: inferior limit: -20 mm; superior limit: 20mm;

- Z axis: inferior limit: 40 mm; superior limit: 80mm.

Figure 3.1 illustrates the B_1 sensitivity profile comparison of the proposed coil configurations. The sensitivity profiles dynamic range is common for all four configurations between 0 to 2E-05 Tesla. In order to compare the configurations in the ROI, the field penetration was simulated for a distance of 80 mm from the coil. Figure 3.2 shows that the best field penetration at this level is achieved by the configuration b, having higher field intensity than the other configurations.

The computed SNR maps using equation (2.16) of the four configurations are displayed in Figure 3.3. Analyzing the SNR maps, one can conclude that an increased number of channels provides higher SNR around the border of the phantom and in the ROI. Furthermore, configuration d

offers higher SNR than all the other configurations in the ROI for along the x-axis at a distance of 50mm from the coil (Figure 3.4).

To conclude, configuration d composed of 6 elliptical loops (2.75x3 cm) offered the best SNR performance in the ROI.
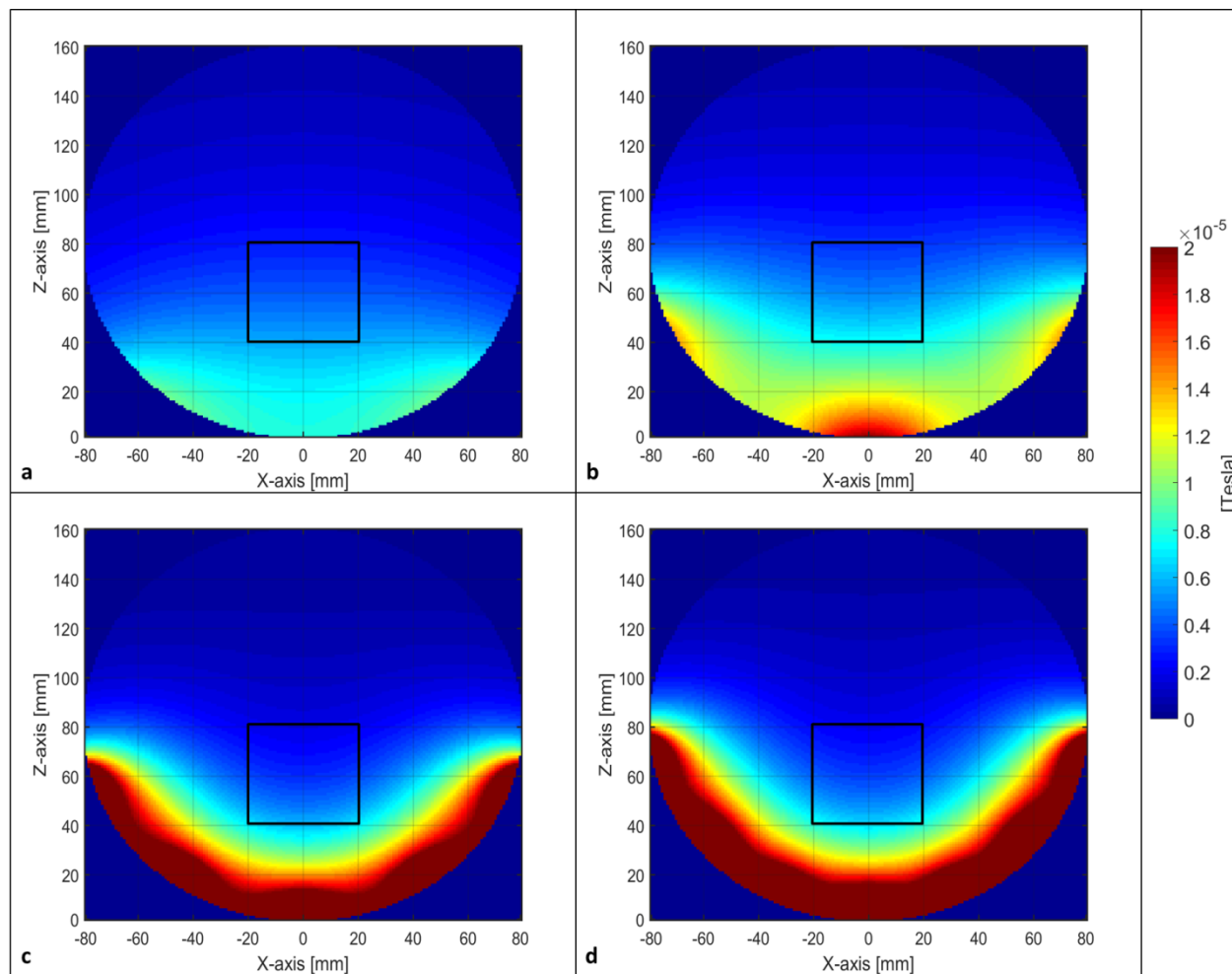

Figure 3.1- B$_1$ field sensitivity profile simulations for one loop (a), two loops (b), four loops (c) and six loops (d).
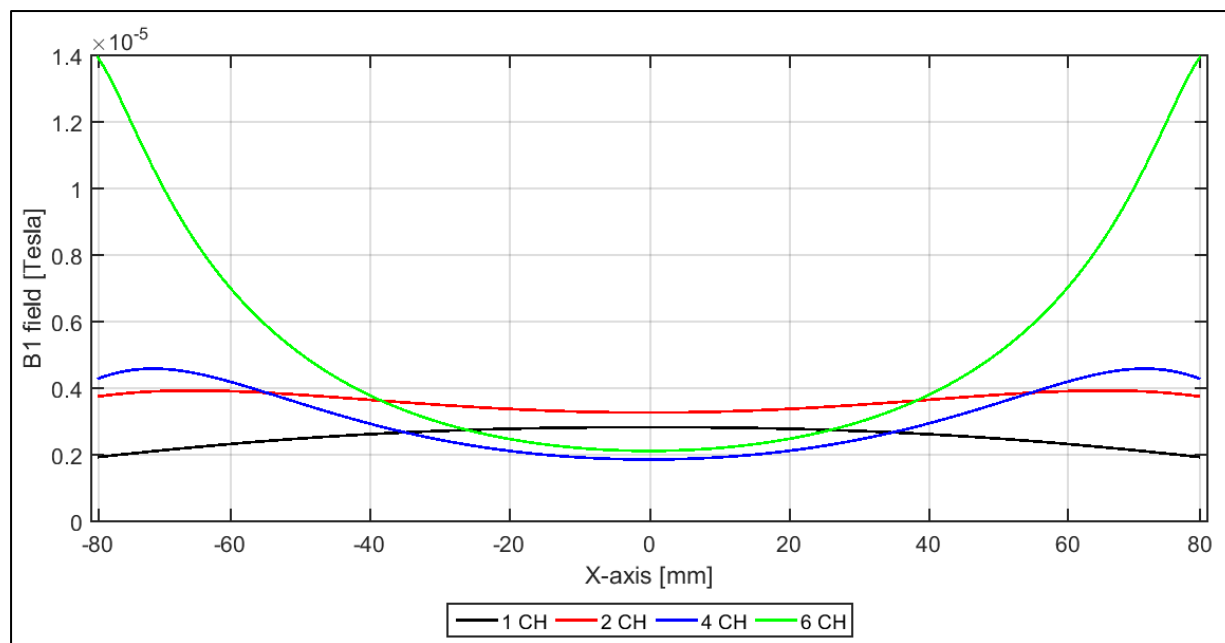
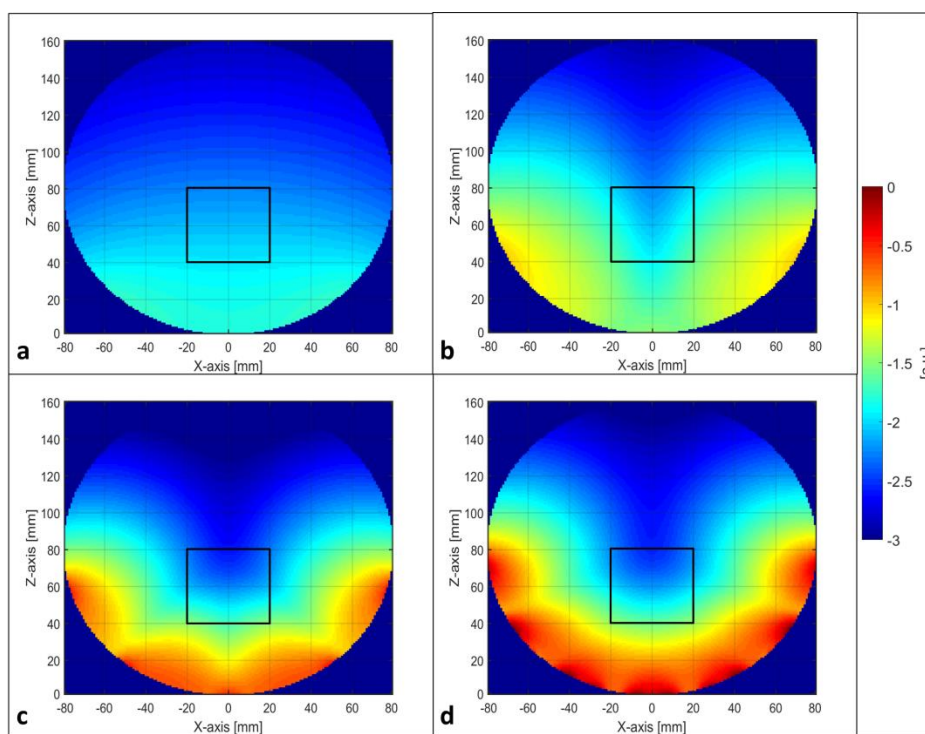Figure 3.2- B$_1$ field sensitivity profile for Z=50mm.

Figure 3.3- Relative SNR simulations for one loop (a), two loops (b), four loops (c) and six loops (d).
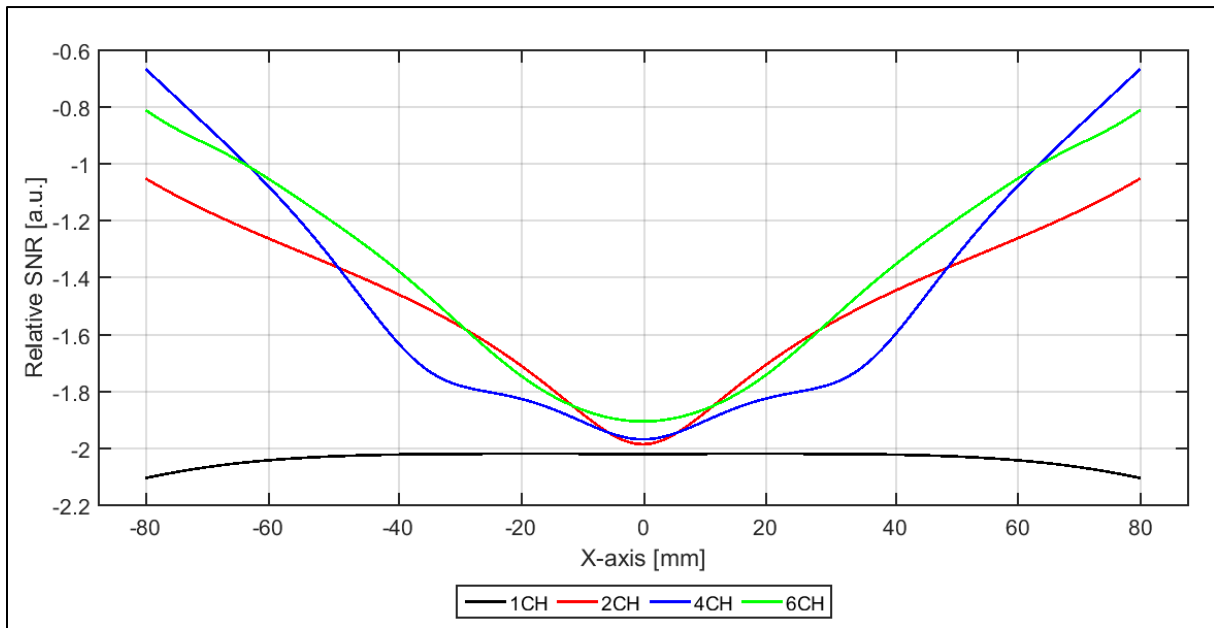
Figure 3.4- Relative SNR for Z=50mm.

3.1.2 FEKO
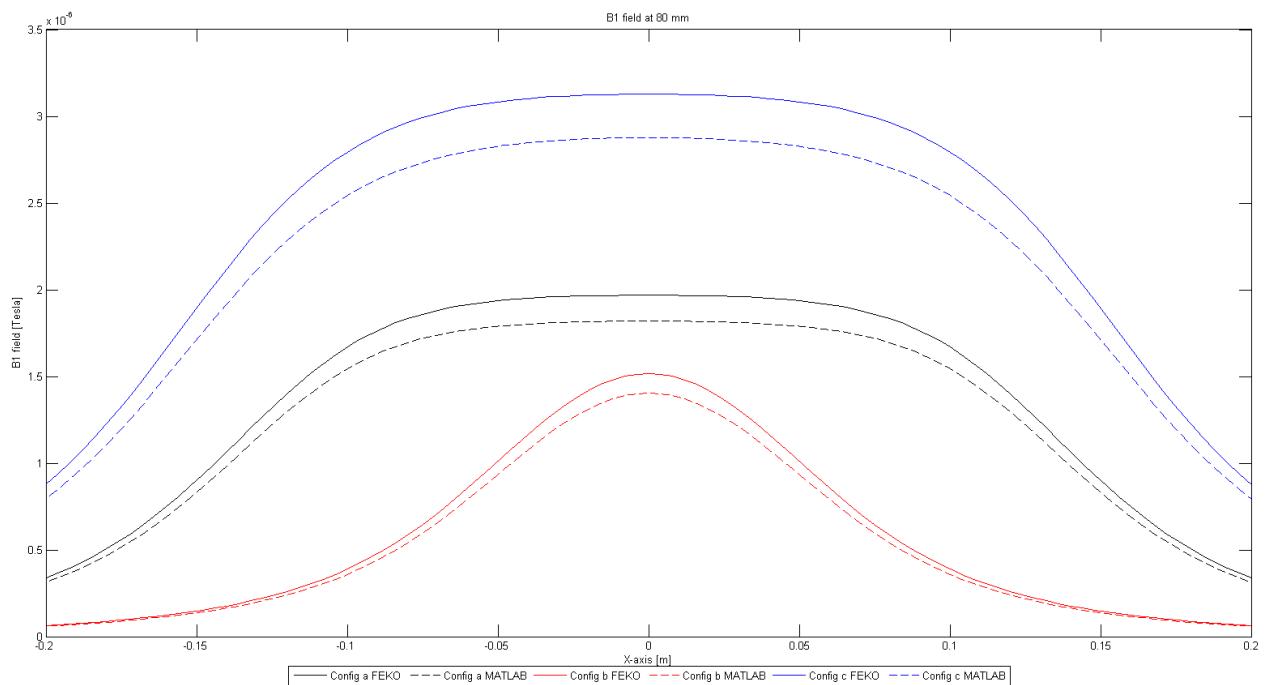
Figure 3.5- MATLAB script validation

Figure 3.5 shows the B1 field sensitivity profile computed using the developed electromagnetic simulations and the using FEKO software. The plot illustrates that the results by the MATLAB

scripts have a similar trend to the results obtained from FEKO. The average standard deviation between the MATLAB scripts and the FEKO simulations are illustrated in the table below.

Table 3.1- Comparison MATLAB-FEKO

Configuration	Average standard deviation
A	5.34%
B	2.19%
C	10.70%

The magnetic field intensity profile of a single rectangular loop is illustrated in Figure 3.6. The field profile is similar to the profile obtained in the Figure 3.1. (a). Moreover, the frequency response (Figure 3.7) obtained using a S_{11} parameter extraction shows a resonant frequency of 123.2MHz with an amplitude of -23.21dB.
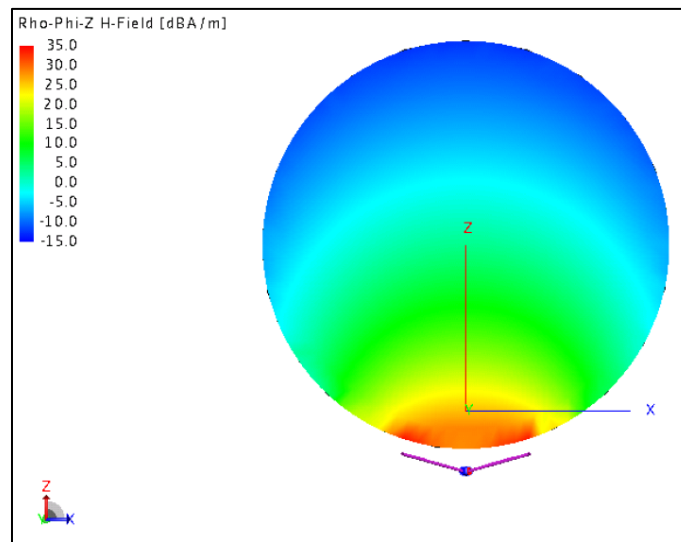
Figure 3.6- Magnetic field intensity profile for a single rectangular loop.
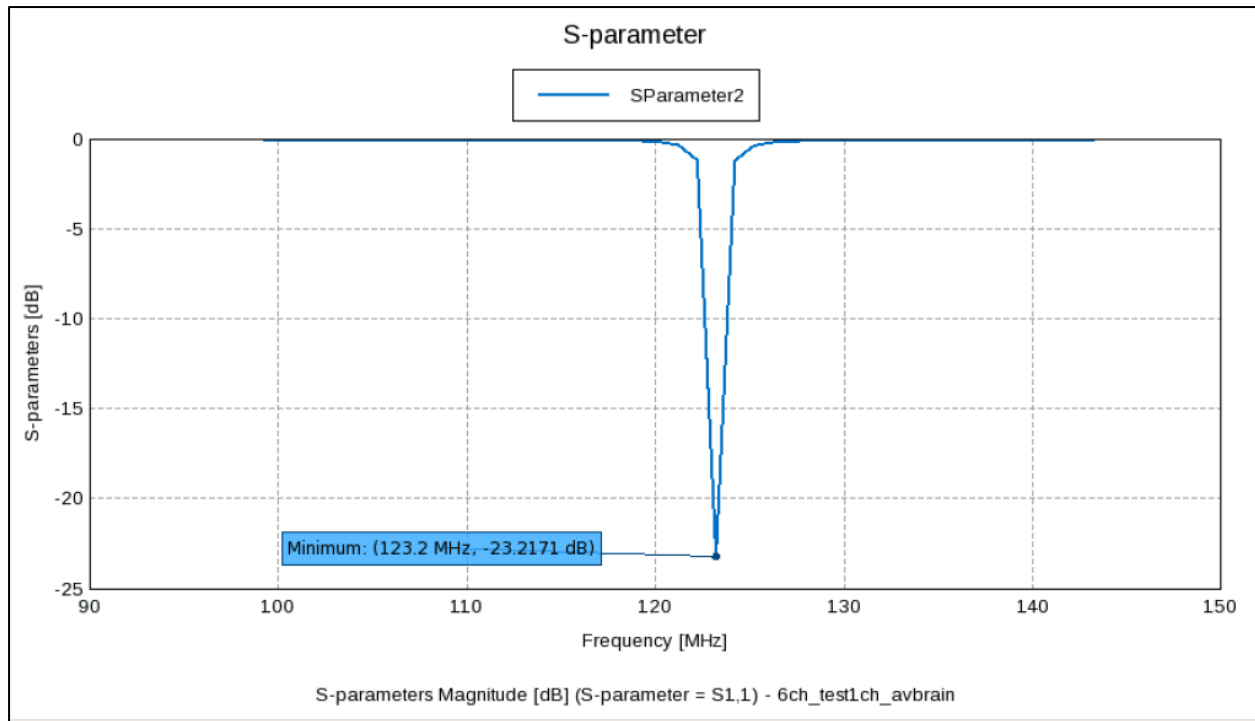
Figure 3.7- Frequency response for a single rectangular loop.

The magnetic field intensity profile of the second configuration composed of two rectangular loops is illustrated in Figure 3.8. Both loops had a resonant frequency of 123.2 MHz, with an amplitude of -21.21 dB for the first channel and -24.15dB for the second channel (Figure 3.9). The overlapping between the loops was adjusted obtaining a decoupling level (Figure 3.10) between the two channels of -8.8dB.
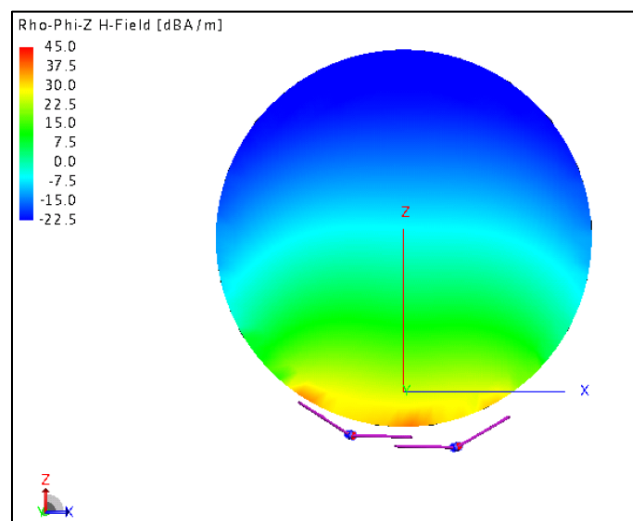

Figure 3.8- Magnetic field intensity profile for a two rectangular loops array.
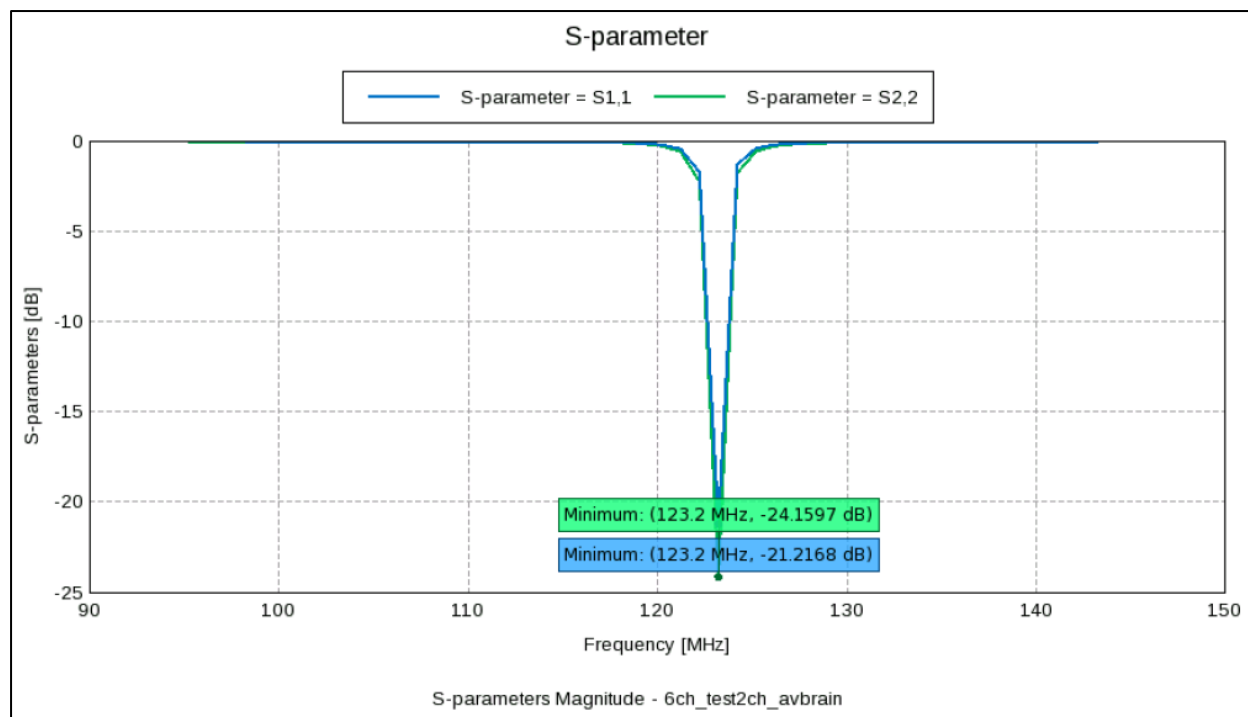
Figure 3.9- Frequency response for a two rectangular loops array.
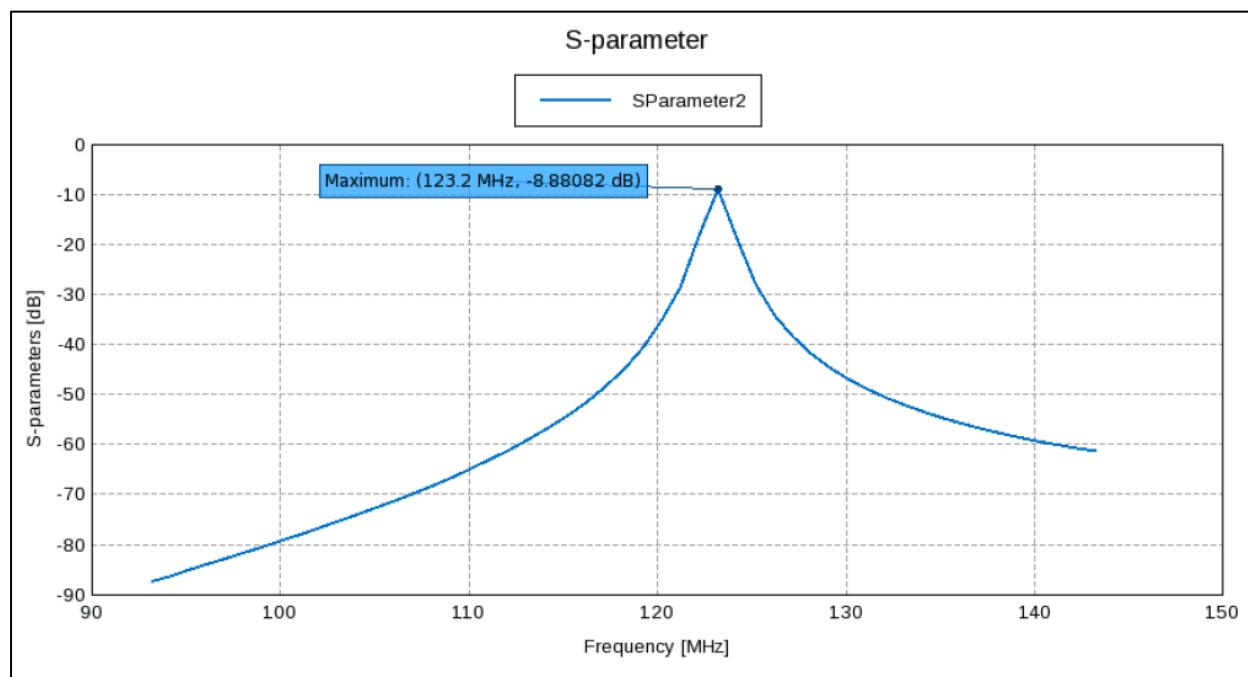

Figure 3.10- Frequency response of decoupling for a two rectangular loops array.

The third configuration composed of four rectangular loops provided higher magnetic field intensity around the loops (Figure 3.11). The frequency response (Figure 3.12) of each individual

channel provided an amplitude varying from -7.68db to -17.86 dB for a resonant frequency of 123.3MHz. The interaction between the channels was higher, compared to the previous configuration. The decoupling level (Figure 3.13) between neighboring and non-neighboring channels ranged from -15dB to -7dB. An important coupling occurred between channel 1 and 2 illustrate in the S_{31} measurement in Figure 3.13.
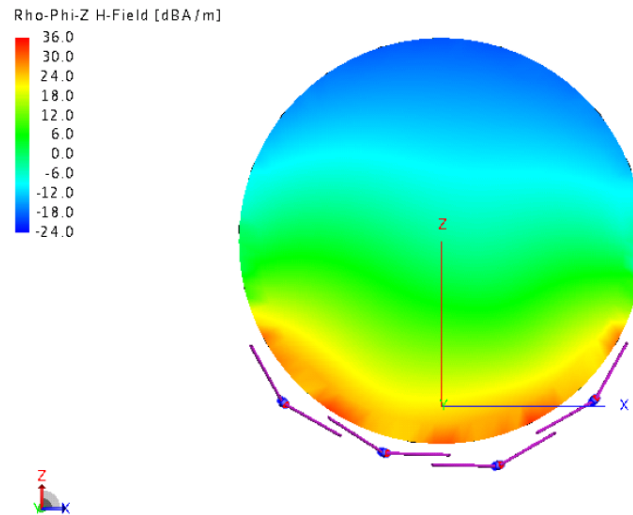

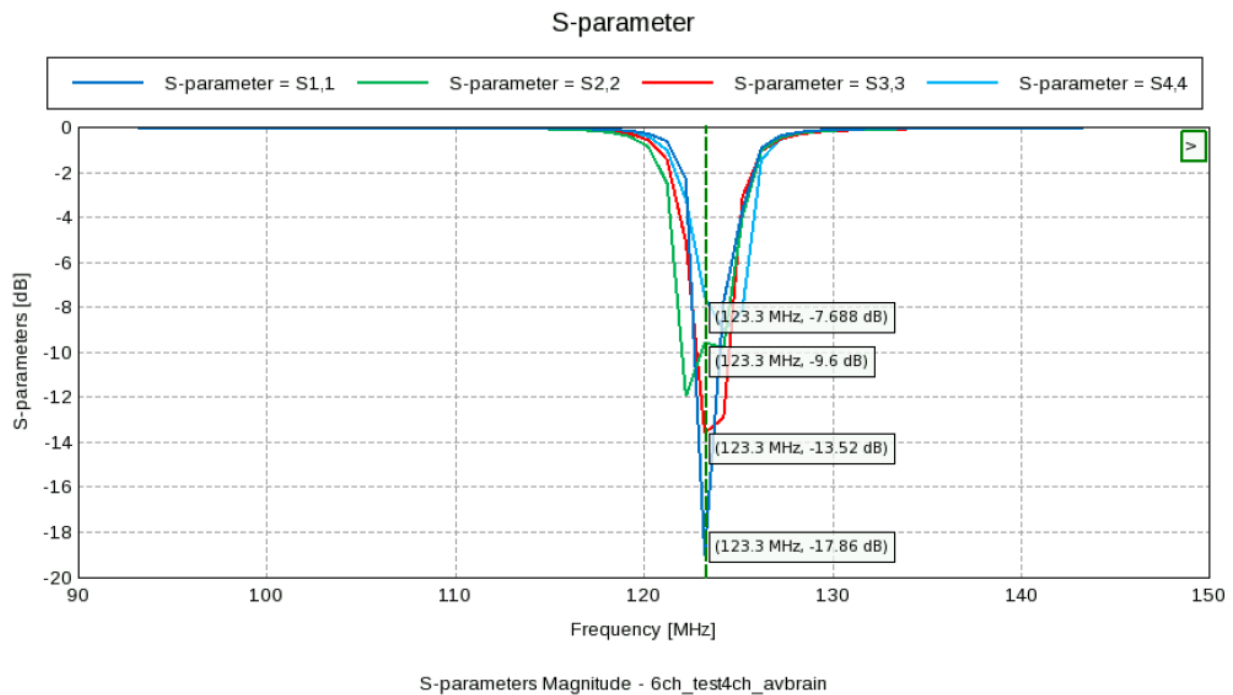Figure 3.11- Magnetic field intensity profile for a four rectangular loops array.

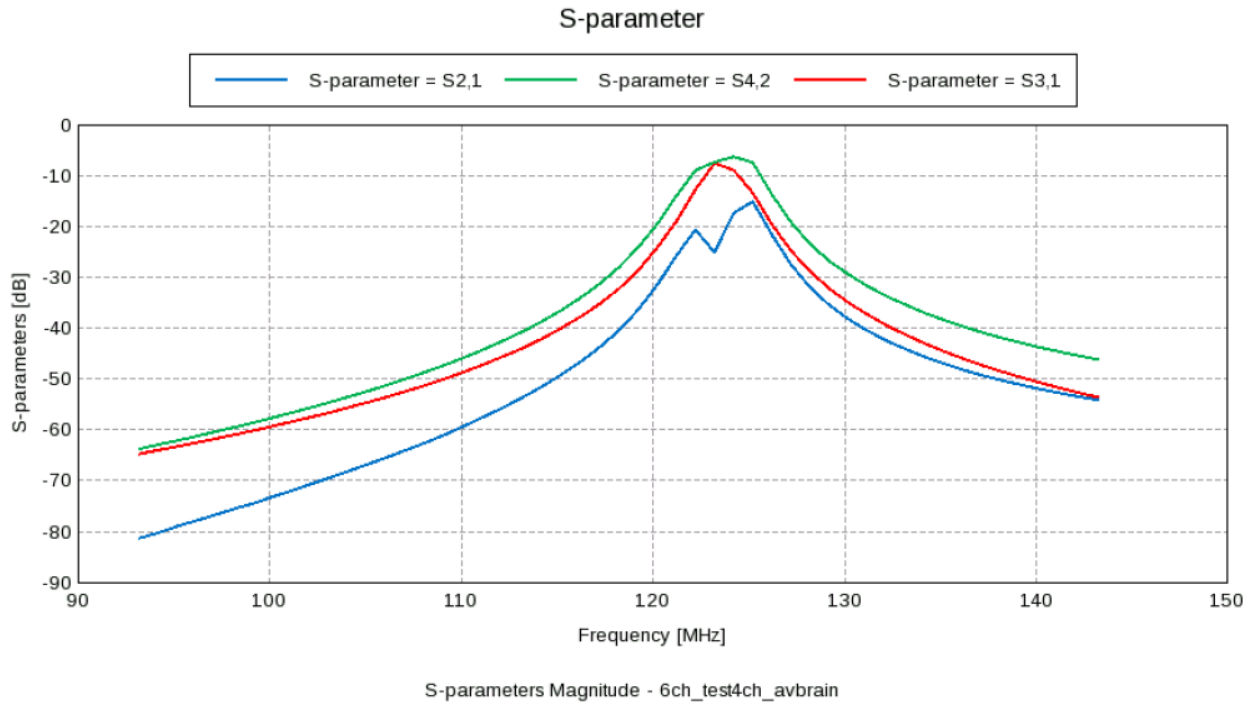Figure 3.12- Frequency response for a four rectangular loops array.

Figure 3.13- Frequency response of decoupling for a four rectangular loops array.

The last configuration had six rectangular loop carefully overlapped to reduce the inductive coupling. The magnetic field intensity profile (Figure 3.14) shows a wider distribution than the previous configurations. The frequency response (Figure 3.15) of the individual channel resulted in amplitudes from -8.48dB to -33.16dB. The coupling between channels illustrates a poor S_{21} measurement for channels 1-2 and 1-3 (Figure 3.16). The field distribution was perturbed due to the coupling between the presented channels.
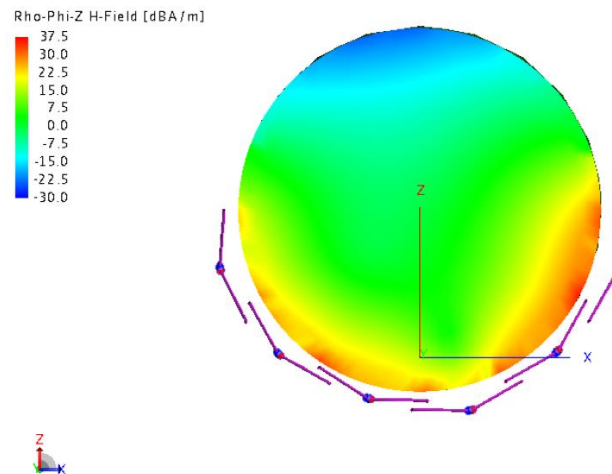

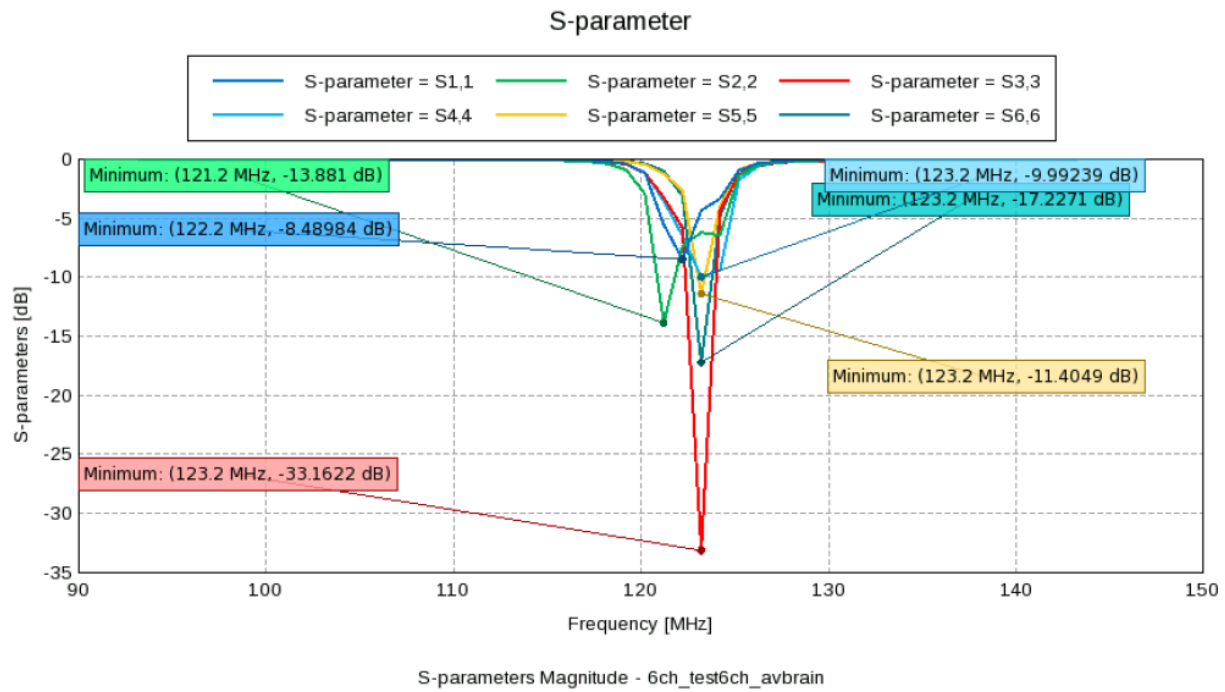Figure 3.14- Magnetic field intensity profile for a six rectangular loops array.

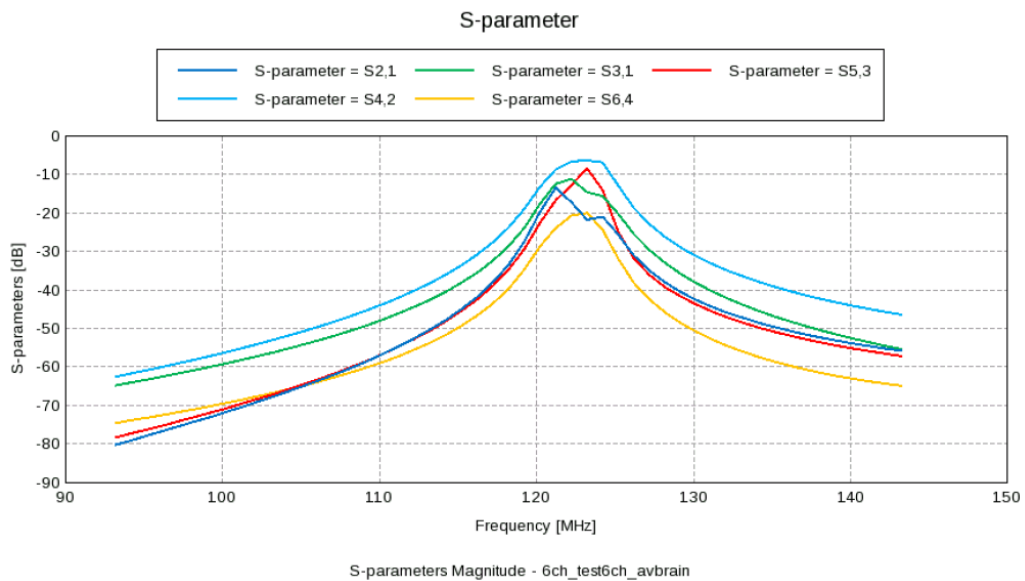Figure 3.15- Frequency response for a six rectangular loops array.

Figure 3.16- Frequency response of decoupling for a six rectangular loops array.

3.2 Bench measurements

3.2.1 Coil assembly

The coil was assembled including the coil housing (Figure 3.17) and the required electronics (Figure 3.18).
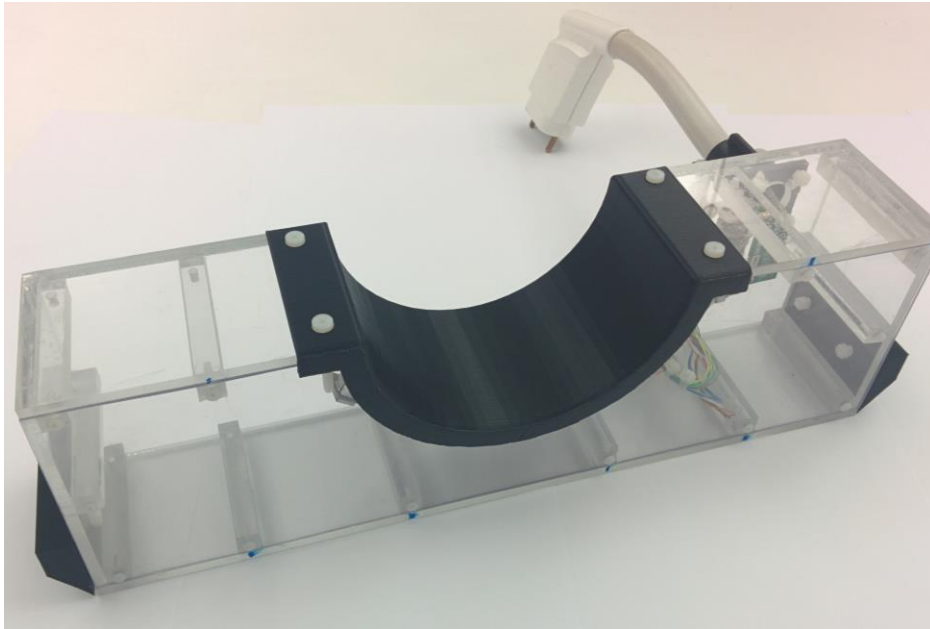

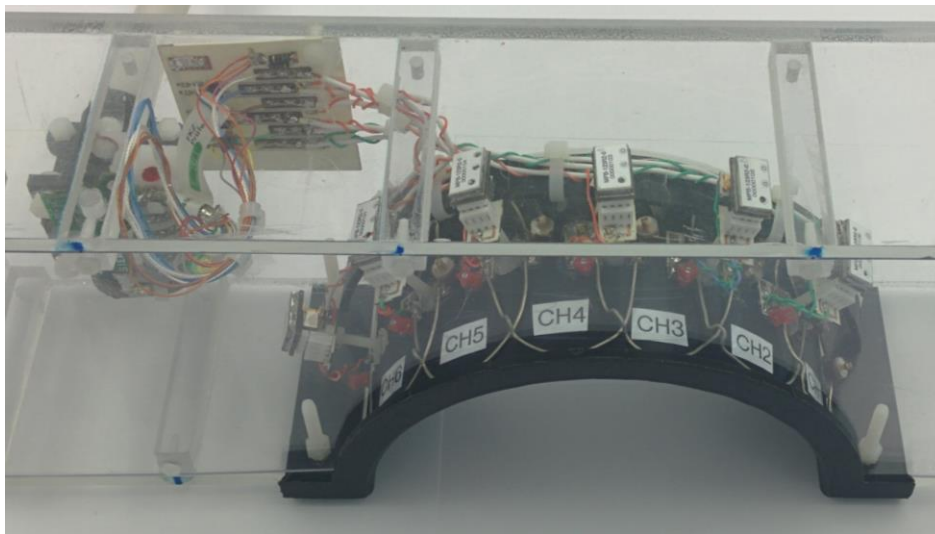
Figure 3.17- Top view of the coil assembly.

Figure 3.18- Zoomed view of the coil electronics.

3.2.2 Tuning

The resonant frequency of each loop of the 6-channel neck array was adjusted to the Larmor frequency imposed by the MRI scanner manufacturer (123.2MHz). The illustrated results had the following parameters:

- Center frequency: 123.2MHz;

- Spanning: 100MHz;

- Intermediate frequency bandwidth (IF BW): 30kHz;

- Reference level: -50dB;

- Vertical axis scale: 10dB.

All channels were tuned to the required frequency. The amplitude measured with the double loop probe of the frequency response was -22.78dB for channel 1 (Figure 3.19), -21.28dB for channel 2 (Figure 3.20), -22.04dB for channel 3 (Figure 3.21), -25.13dB for channel 4 (Figure 3.22), -31.75dB for channel 5 (Figure 3.23) and -24.91dB for channel 6 (Figure 3.24)
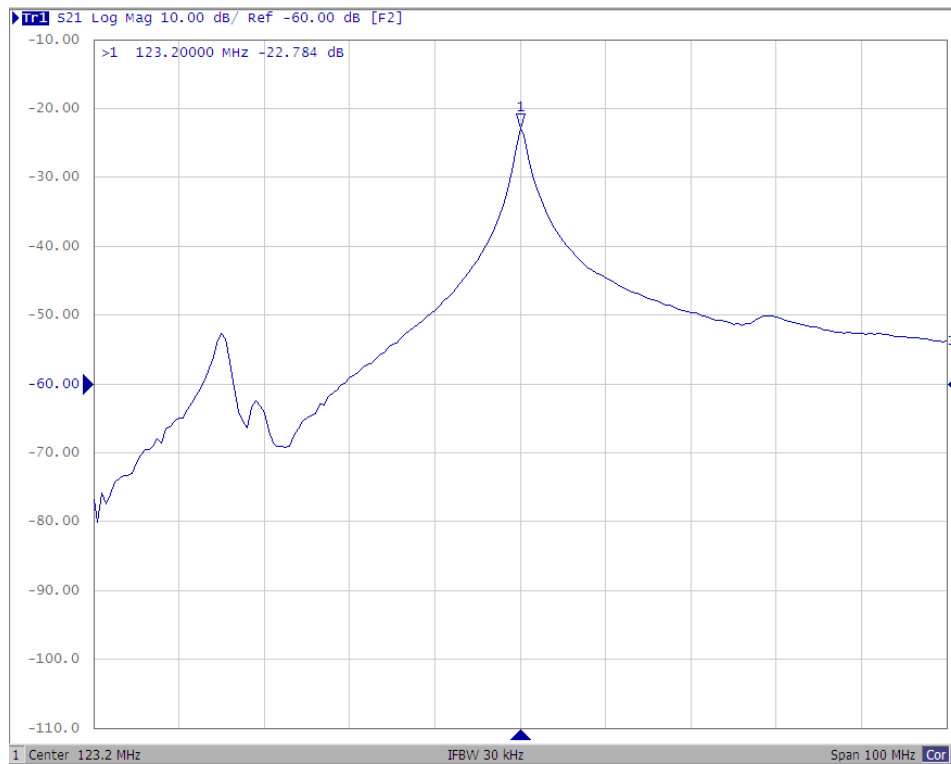

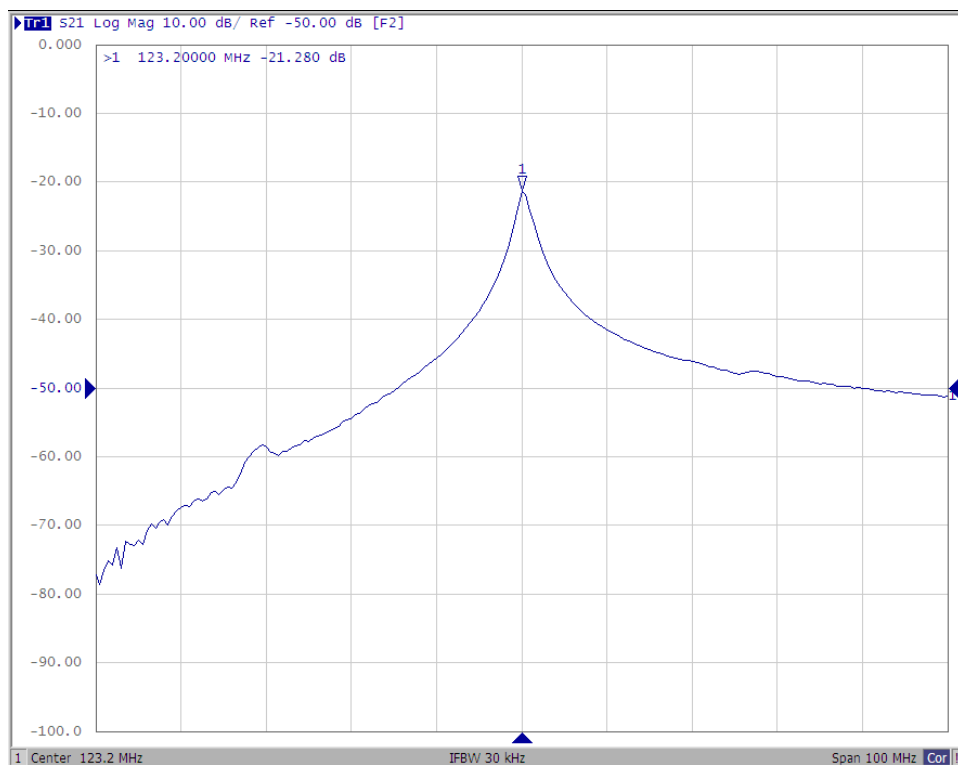Figure 3.19- Resonant frequency of channel 1.

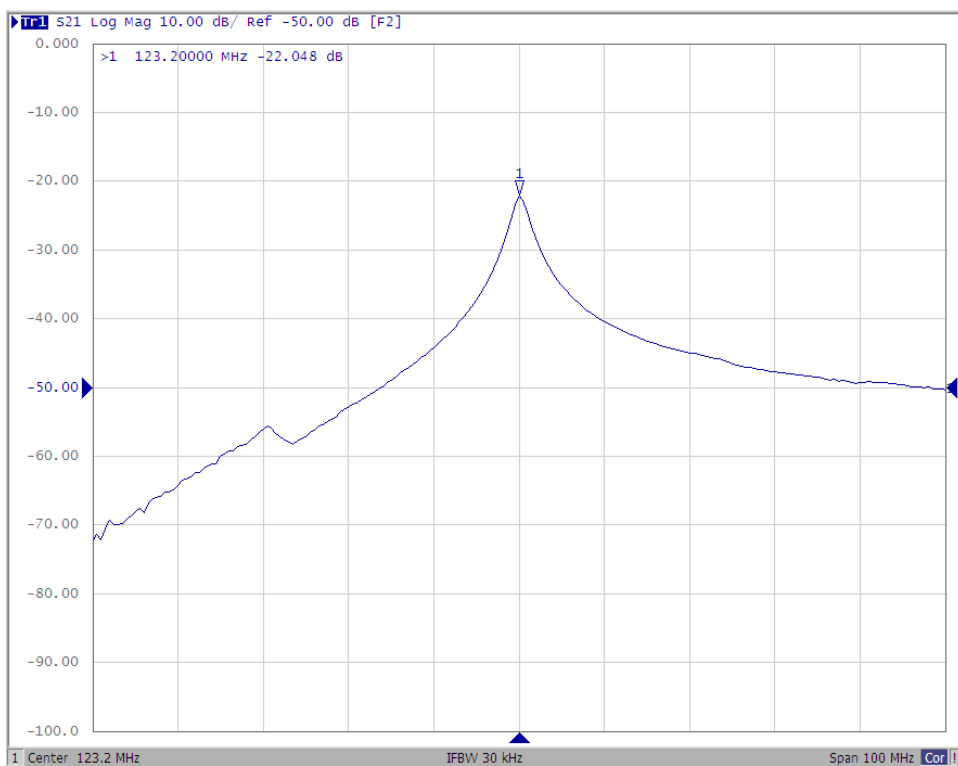Figure 3.20- Resonant frequency of channel 2.

Figure 3.21- Resonant frequency of channel 3.
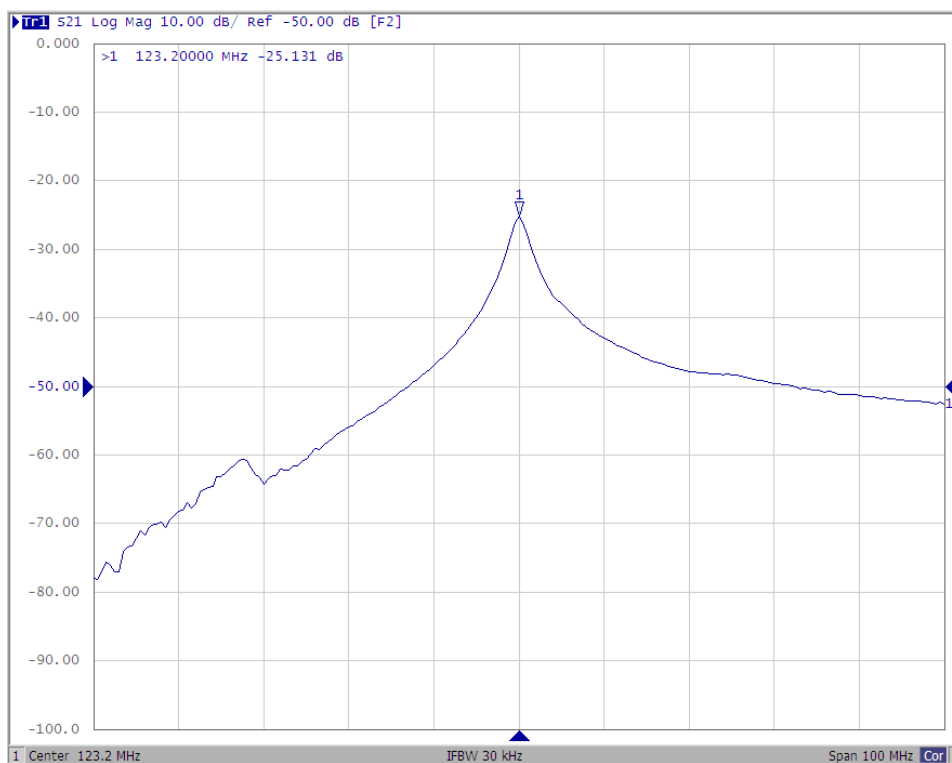
Figure 3.22- Resonant frequency of channel 4.
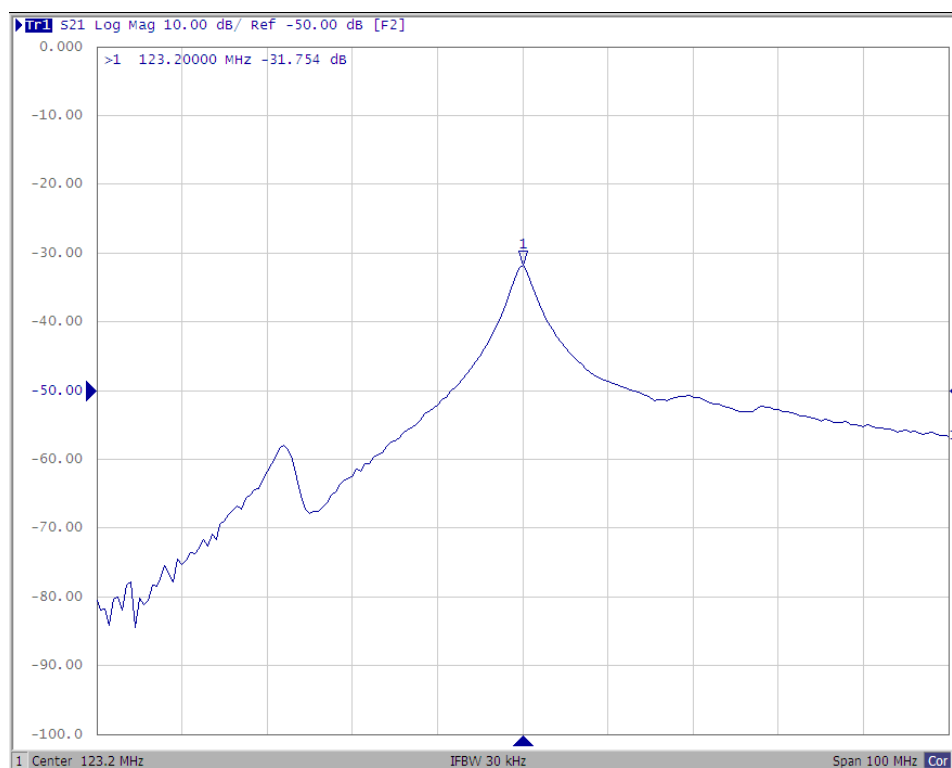
Figure 3.23- Resonant frequency of channel 5.
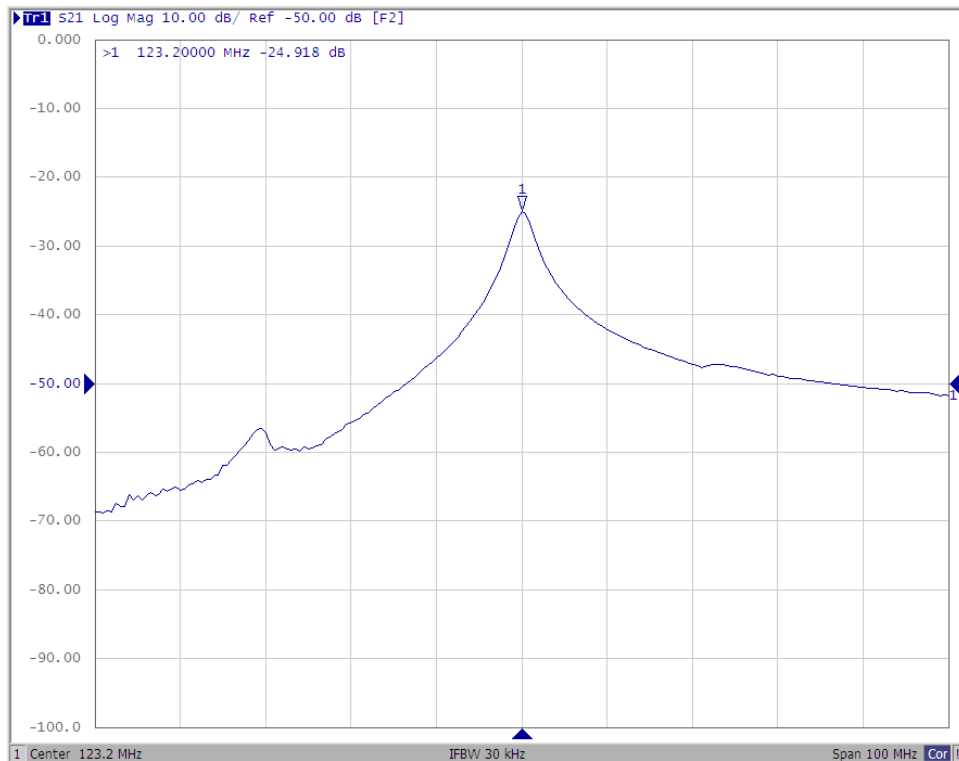
Figure 3.24- Resonant frequency of channel 6.

3.2.3 Q ratio

The Q ratio was measured for a single loop by measuring the resonant frequency response for the two loading conditions. The Q factor for unloaded conditions had a maximum at 123.2MHz of 363.13dB. The Q factor for loaded conditions was 76.458dB. The Q ratio was calculated to 4.74.

The illustrated results had the following parameters:

- Center frequency: 123.2MHz;

- Spanning: 100MHz;

- Intermediate frequency bandwidth (IF BW): 30kHz;

- Reference level: -60dB;

- Vertical axis scale: 10dB.

Figure 3.25- Q ratio. (a) Loaded. (b) Unloaded.

3.2.4 Active detuning

The illustrated results had the following parameters:

- Center frequency: 123.2MHz;

- Spanning: 100MHz;

- Intermediate frequency bandwidth (IF BW): 30kHz;

- Reference level: -50dB;

- Vertical axis scale: 10dB.

The calculated active detuning difference between the two phases of the PIN diode forward biased – reversed biased was: 54.03dB for channel 1 (Figure 3.26), 47.31dB for channel 2 (Figure 3.27), 44.69dB for channel 3 (Figure 3.28), 41.89dB for channel 4 (Figure 3.29), 40.28dB for channel 5 (Figure 3.30), 46.79dB for channel 6 (Figure 3.31). The average active detuning level was 45.83dB.

Figure 3.26- Active detuning of channel 1 - 54.03dB.
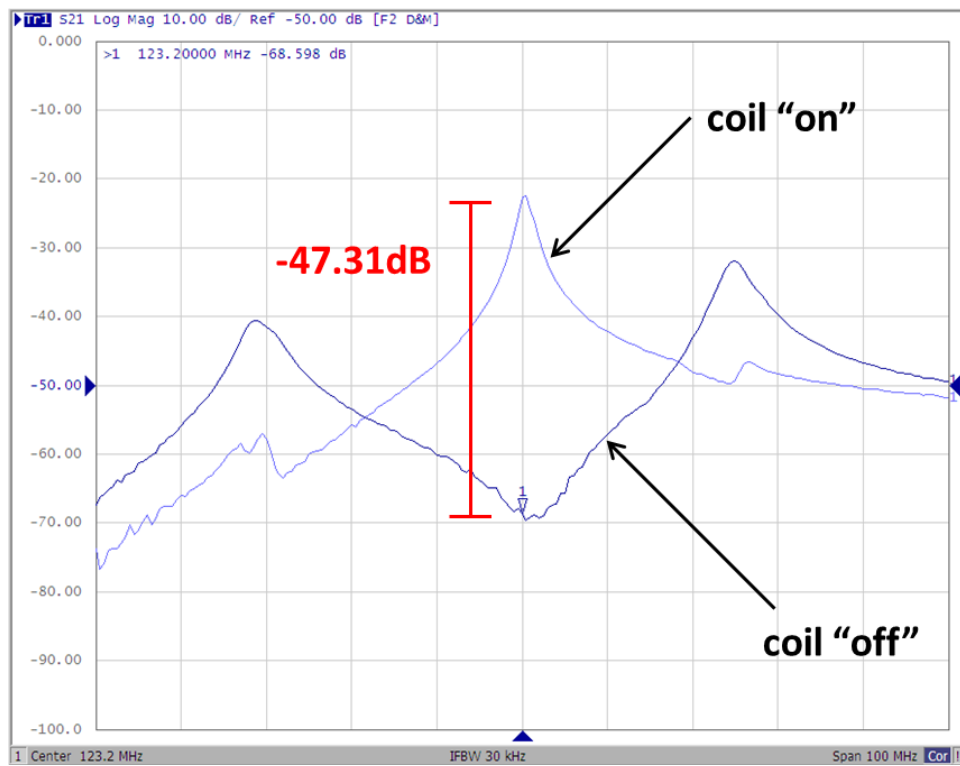
Figure 3.27- Active detuning of channel 2 - 47.31dB.
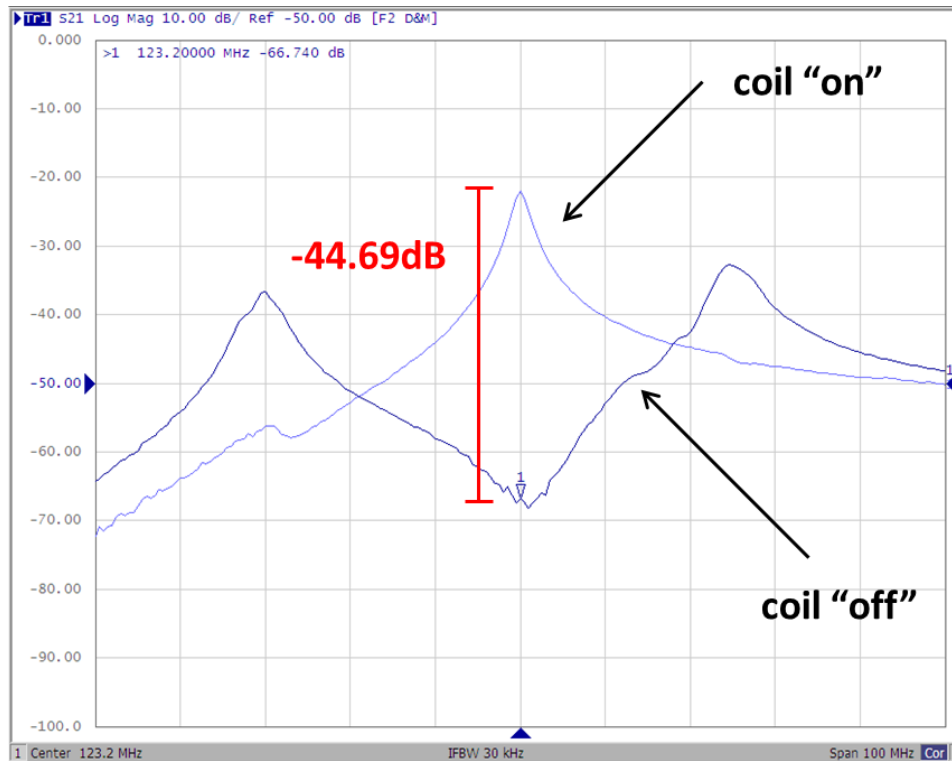
Figure 3.28- Active detuning of channel 3 - 44.69dB.
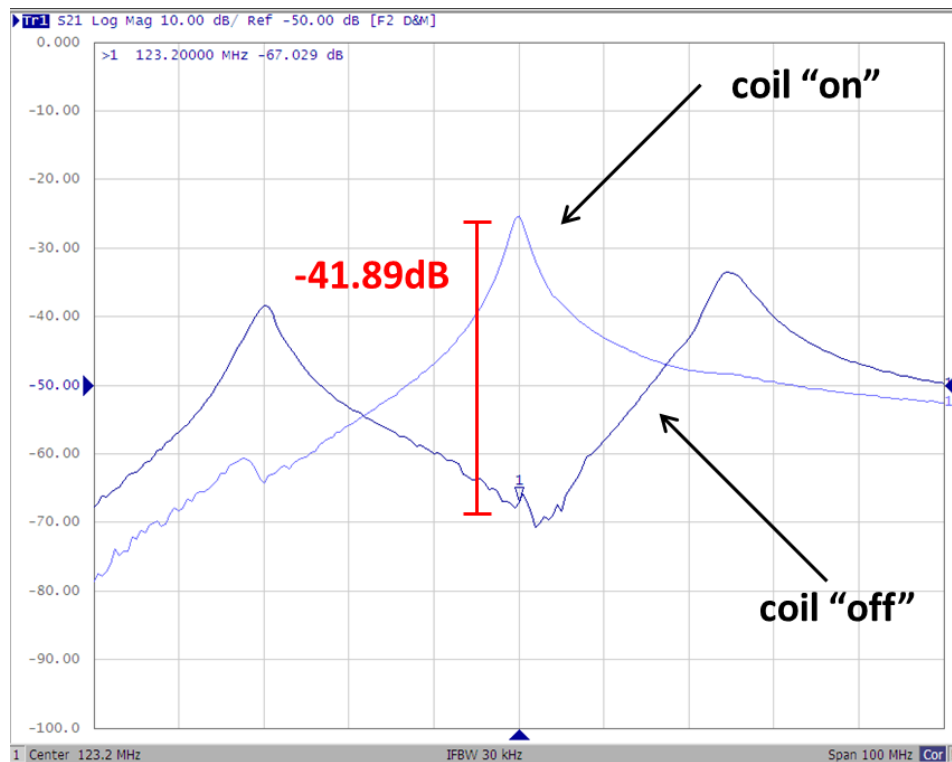
Figure 3.29- Active detuning of channel 4 - 41.89dB.
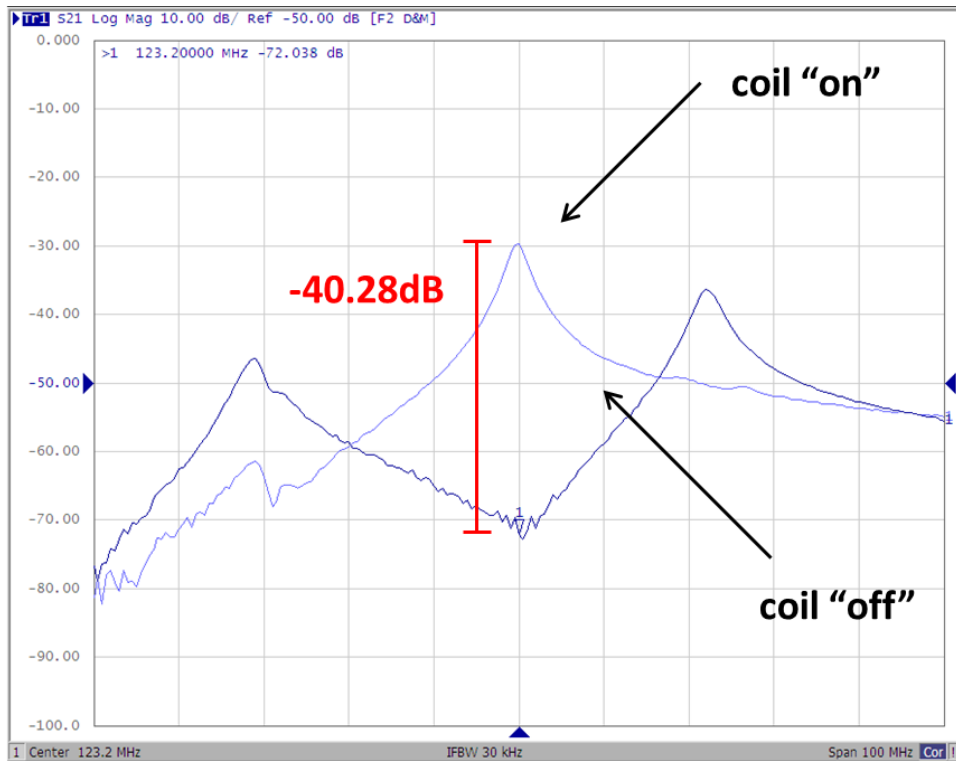
Figure 3.30- Active detuning of channel 5 - 40.28dB.
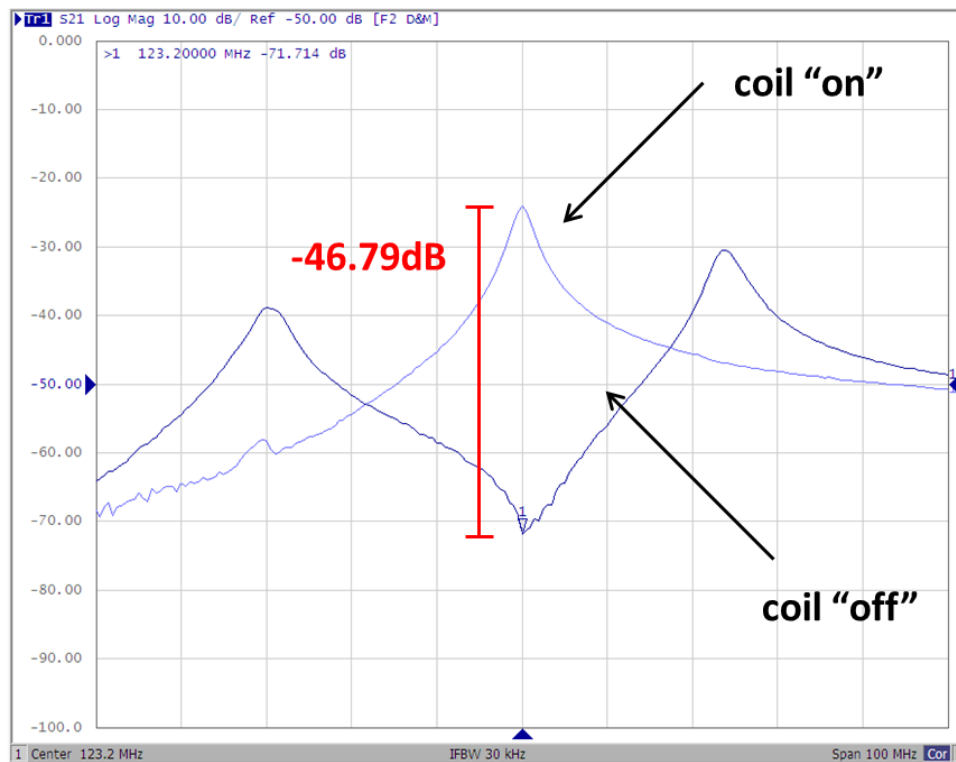
Figure 3.31- Active detuning of channel 6 - 46.79dB.

3.2.5 Geometrical decoupling

The illustrated results had the following parameters:

- Center frequency: 123.2MHz;

- Spanning: 100MHz;

- Intermediate frequency bandwidth (IF BW): 30kHz;

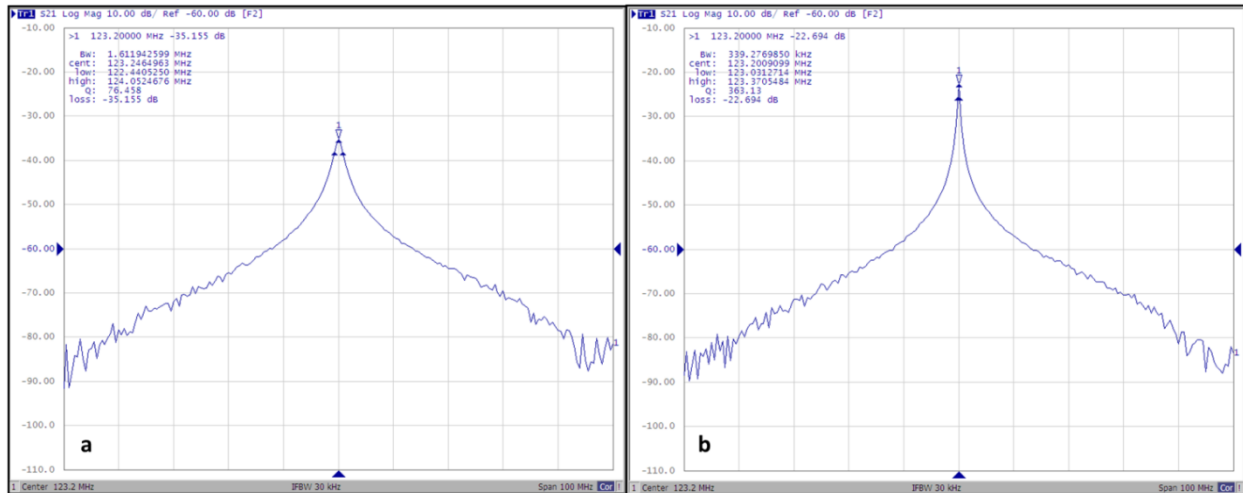- Reference level: -40dB;

- Vertical axis scale : 10dB.

The assessment of a pair of two neighboring channels consisted of a S_{21} measurement. Each channel was connected to a different port.

The geometrical decoupling level between two neighboring loop was: 13.36dB for CH 1-2 (Figure 3.32), 13.80dB for CH 2-3 (Figure 3.33), 14.55dB for CH 3-4 (Figure 3.34), 14.10dB for CH 4-5 (Figure 3.35) and 14.58dB for CH 5-6 (Figure 3.36). The average inductive decoupling was calculated to 14.1dB.
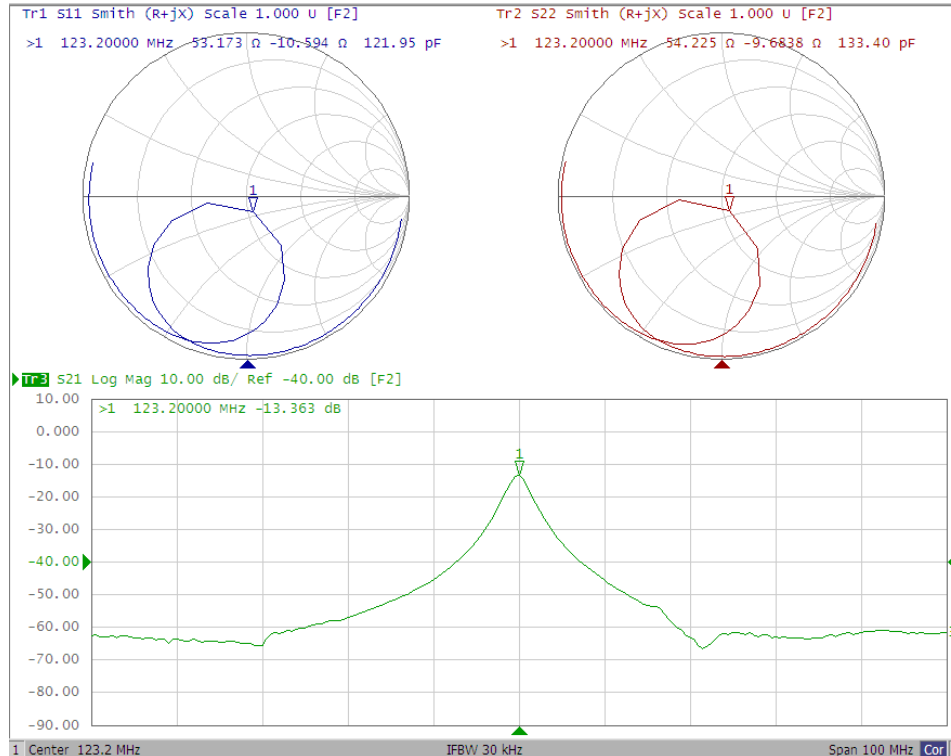
Figure 3.32- Inductive decoupling between CH 1-2.
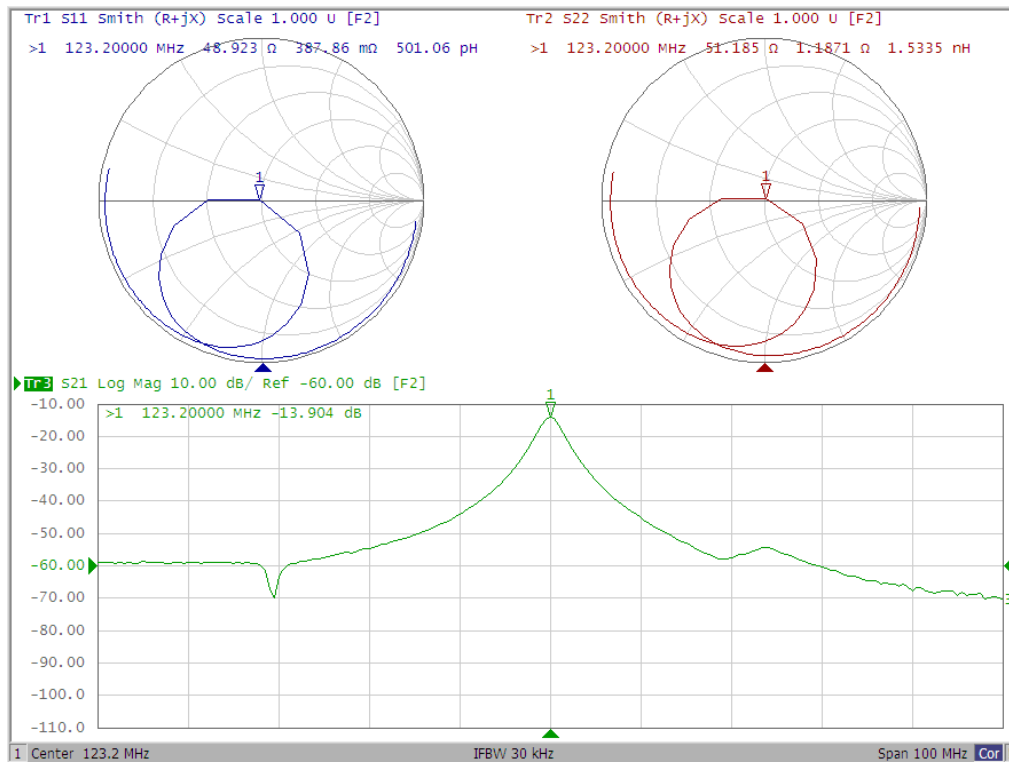
Figure 3.33- Inductive decoupling between CH 2-3.
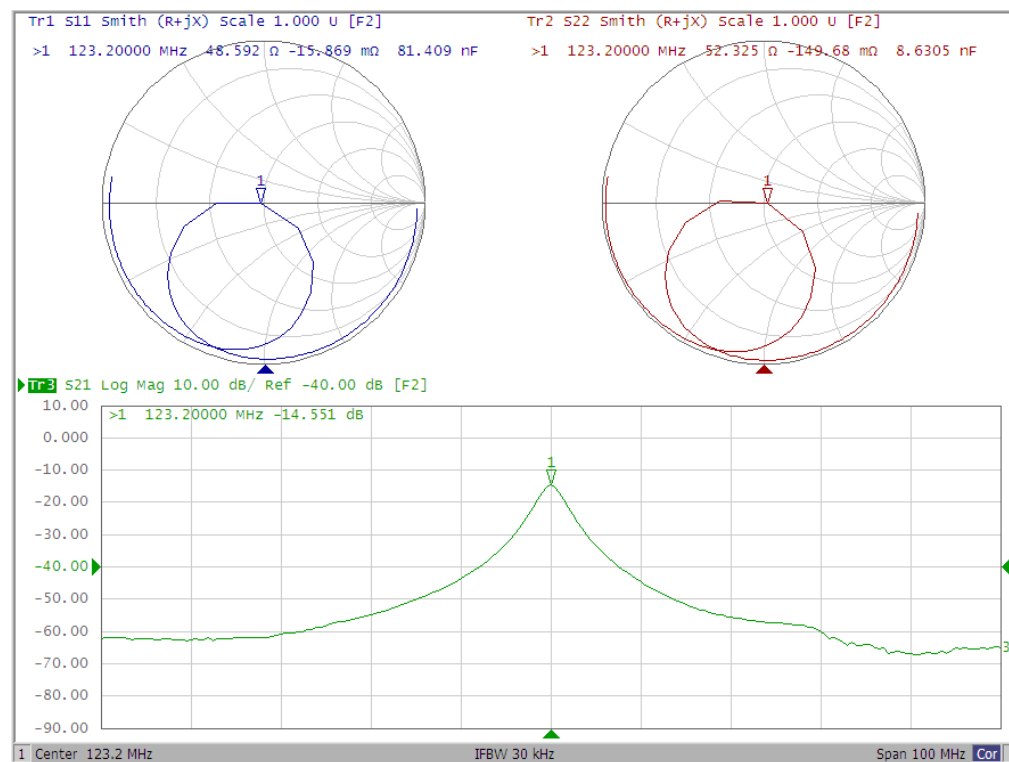
Figure 3.34- Inductive decoupling between CH 3-4.
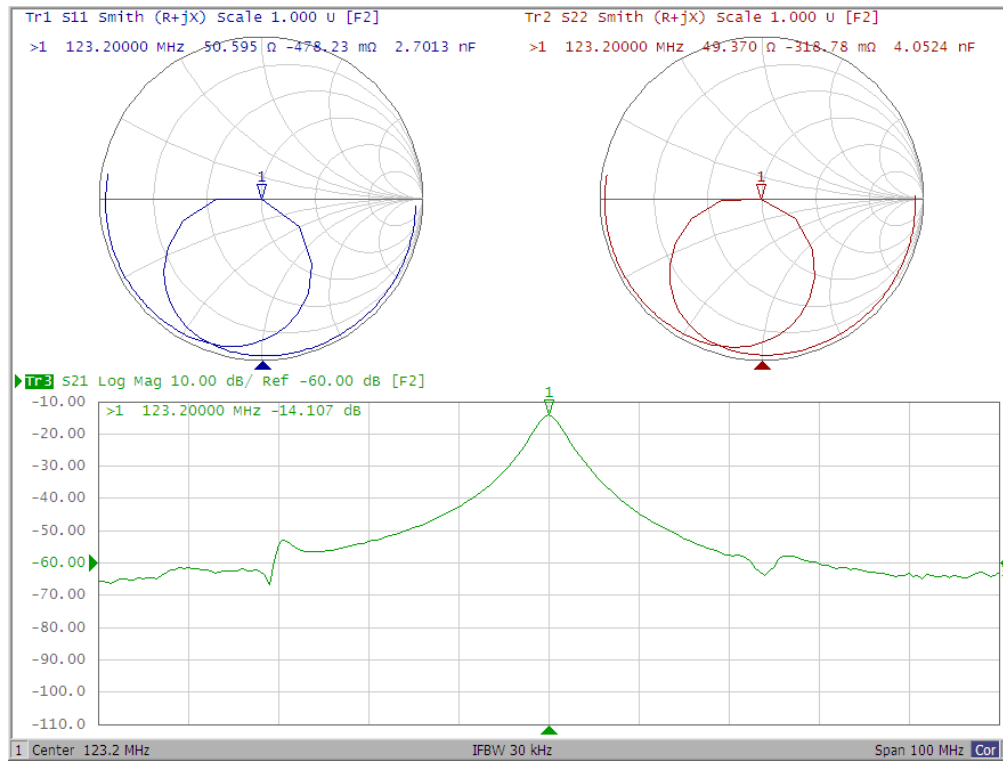
Figure 3.35- Inductive decoupling between CH 4-5.
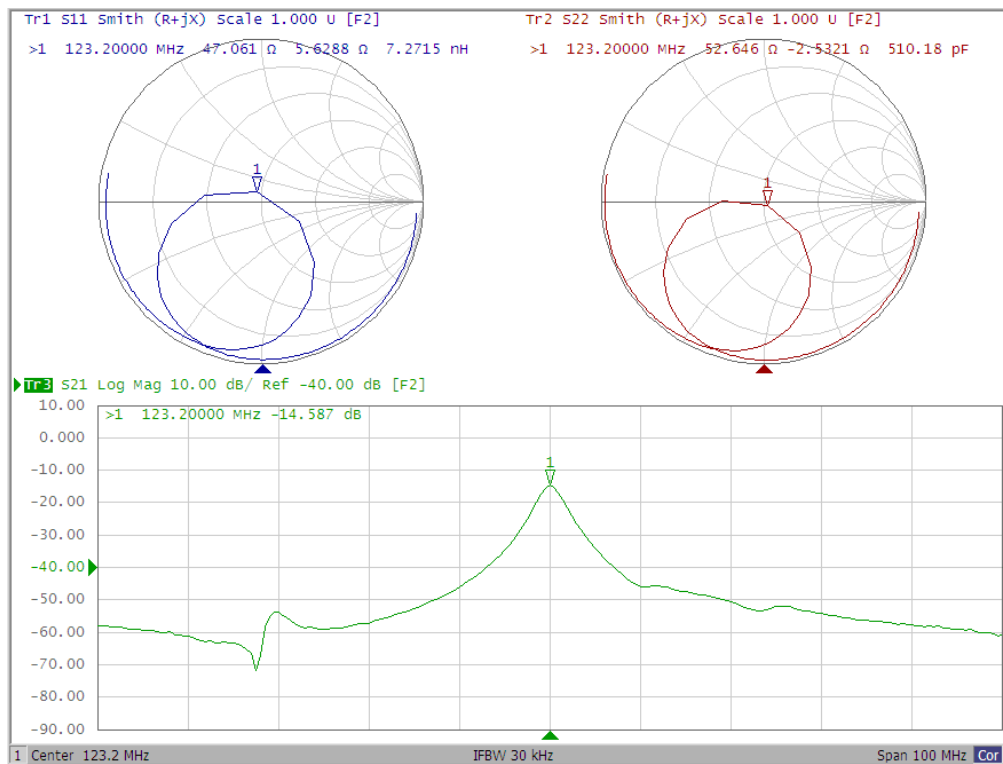
Figure 3.36- Inductive decoupling between CH 5-6.

3.2.6 Preamplifier decoupling

The illustrated results had the following parameters:

- Center frequency: 123.2MHz;

- Spanning: 100MHz;

- Intermediate frequency bandwidth (IF BW): 30kHz;

- Reference level: -50dB;

- Vertical axis scale: 10dB.

The calculated preamplifier decoupling level between the two impedance matching conditions was: 45.9dB for channel 1 (Figure 3.37), 33.71dB for channel 2 (Figure 3.38), 27.30dB for channel 3 (Figure 3.39), 39.97dB for channel 4 (Figure 3.40), 38.02dB for channel 5 (Figure 3.41), 35.47dB for channel 6 (Figure 3.42). The average preamplifier decoupling level was 36.73dB.
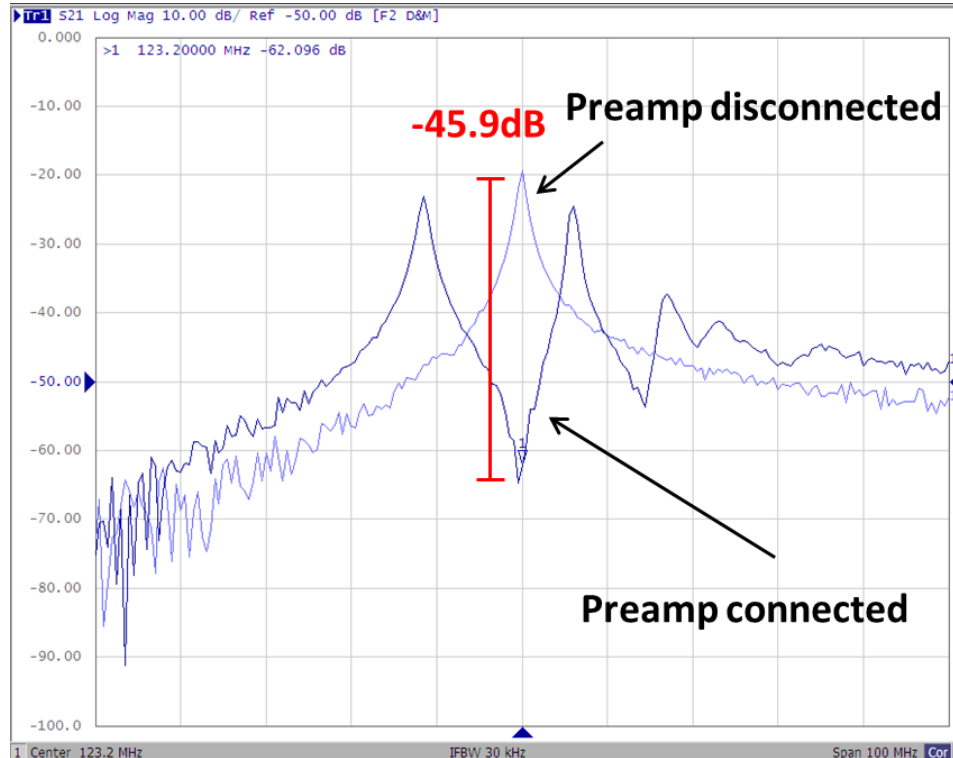
Figure 3.37- Preamplifier decoupling of channel 1 - 45.9dB.
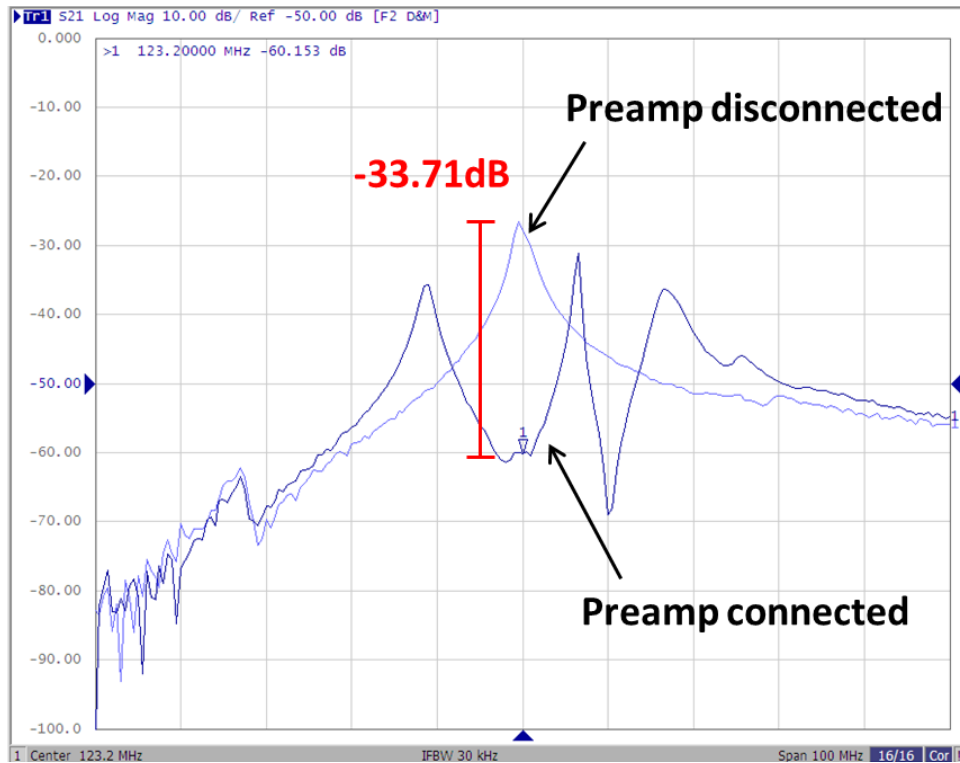
Figure 3.38- Preamplifier decoupling of channel 2 - 33.71dB.
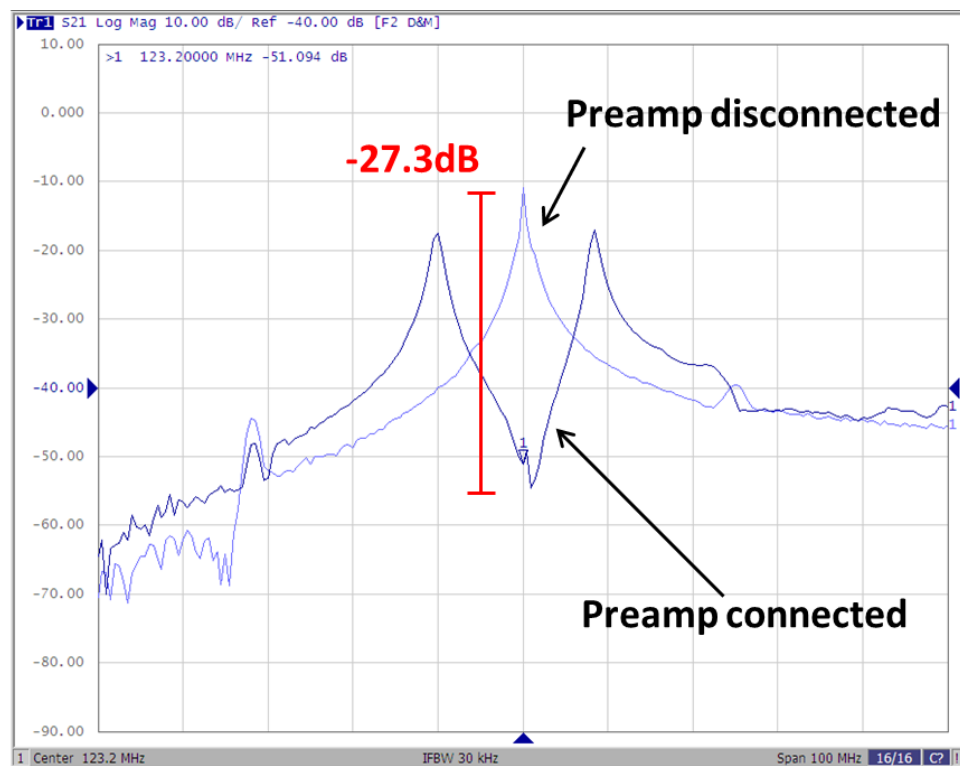
Figure 3.39- Preamplifier decoupling of channel 3 - 27.3dB.
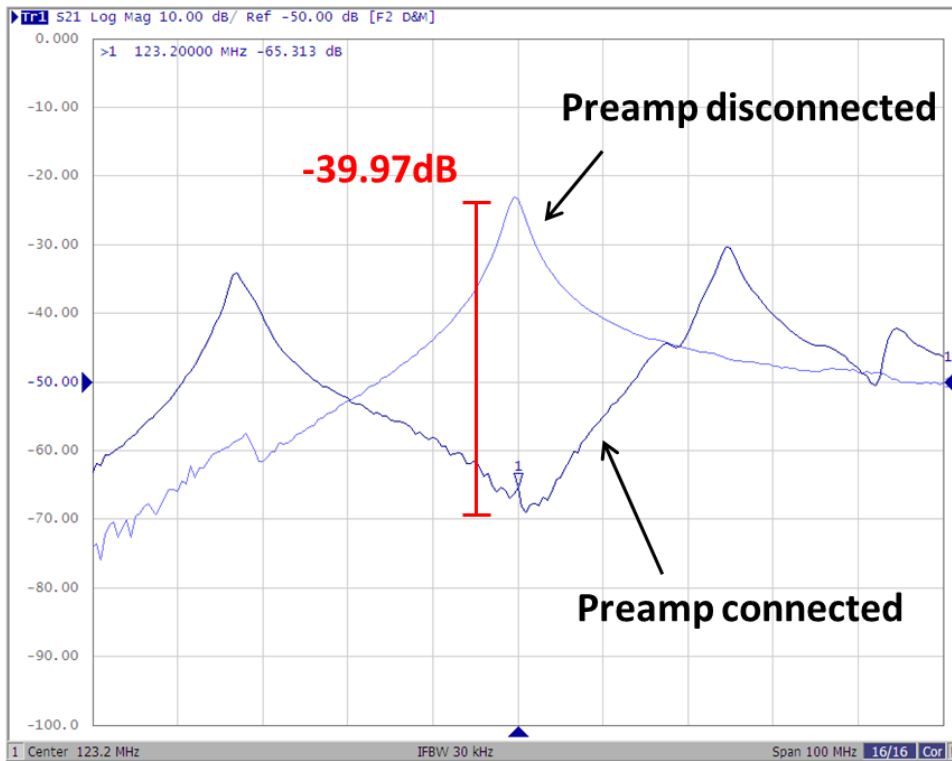
Figure 3.40- Preamplifier decoupling of channel 4 - 39.97dB.
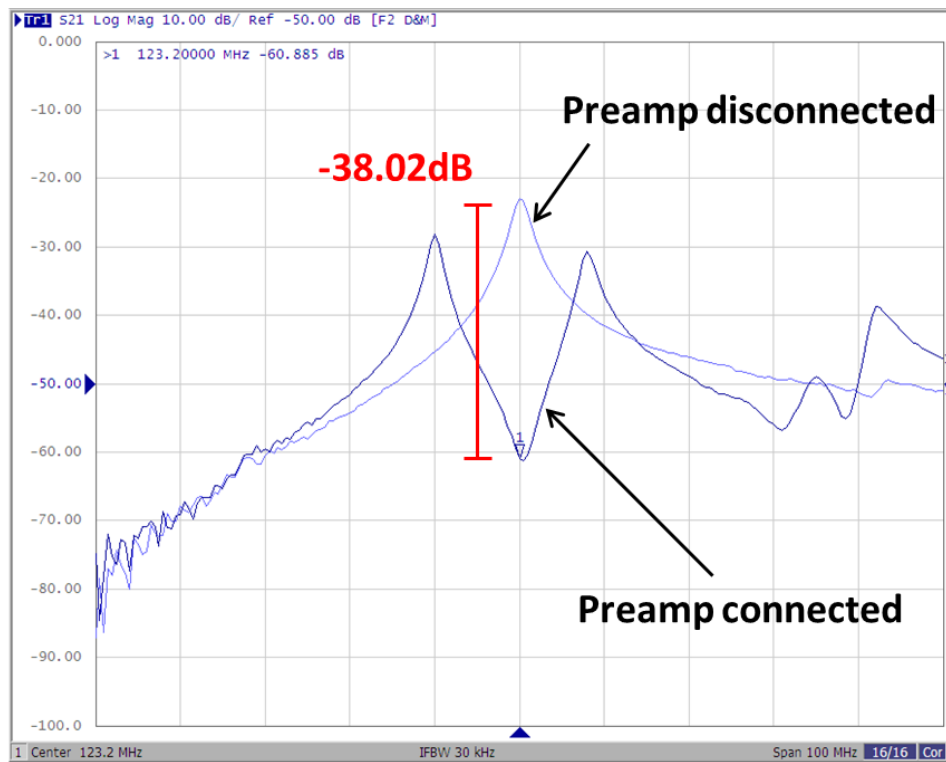
Figure 3.41- Preamplifier decoupling of channel 5 - 38.02dB.
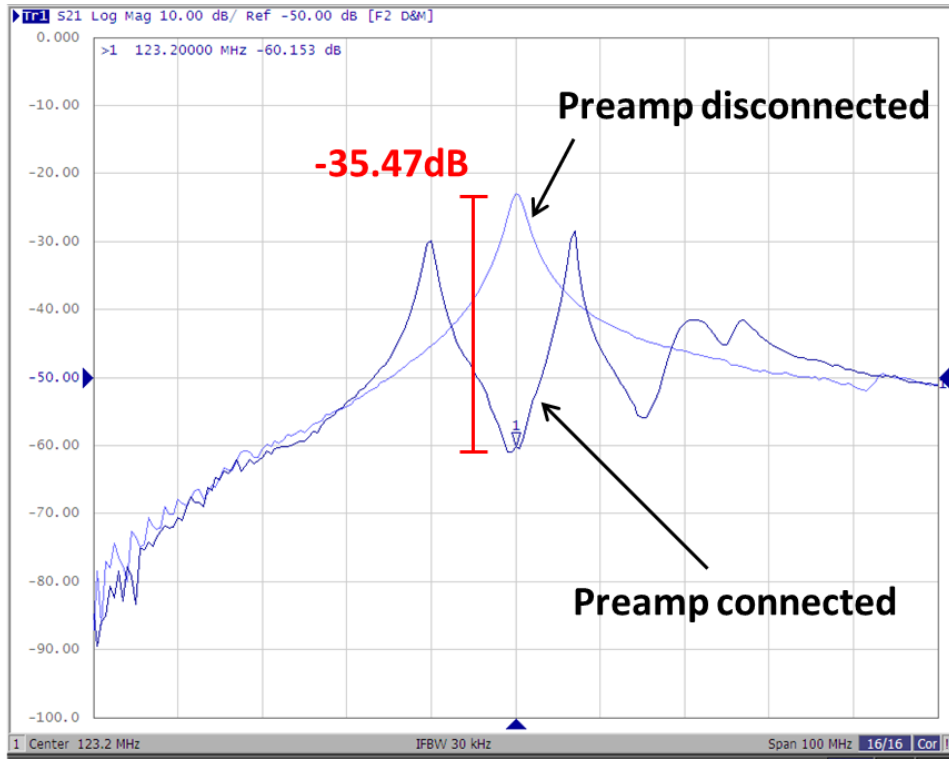
Figure 3.42- Preamplifier decoupling of channel 6 - 35.47dB.

3.3 MRI measurements

3.3.1 Phantom validation

An initial characterization of the coil performances on the coil in the MRI was made using a phantom. The SNR maps were computed for both custom built coil and the commercial coil. Furthermore, the SNR was compared in the ROI (6.6x9.4cm, 62.6cm^2) obtaining an average value of 42.64 for the custom built coil higher than 36.62 for the commercial one. The commercial coil offers a wider field distribution, while the custom built one has a better penetration.
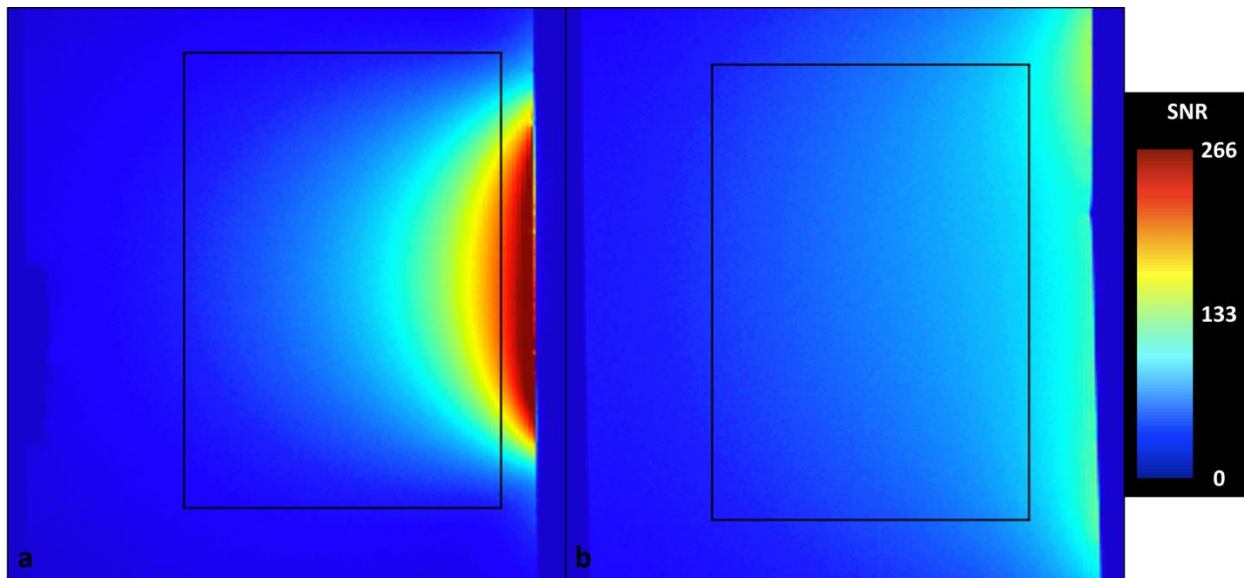
Figure 3.43- SNR maps of the water phantom obtained using the custom-built coil (a) and the commercial coil (b).

Moreover, the noise covariance matrix was computed for the custom built coil. The noise coupling between the elements are within the recommended limits (<0.5), having an average covariance of 0.18. The maximum coupling level was 0.4.
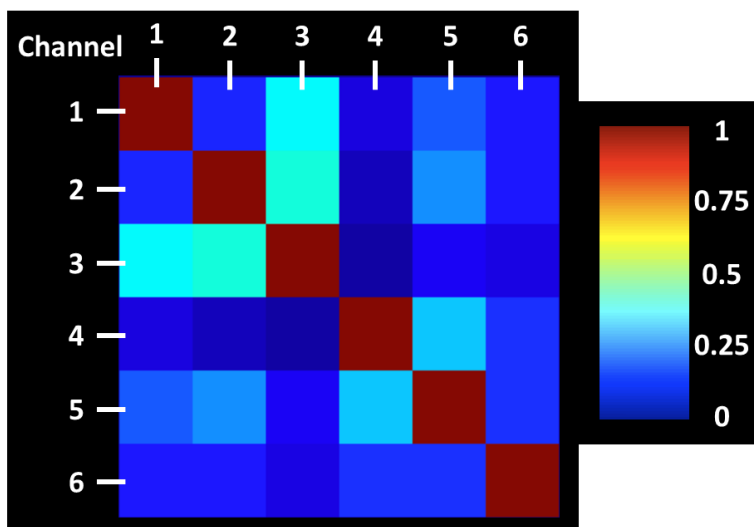
Figure 3.44- Noise covariance matrix.

3.3.2 Human subject validation

Similar to the water phantom validation, an initial set of initial coil performance was performed on an adult human subject. The SNR maps were acquired and compared for a ROI centered at C4 vertebral level of the spinal cord. For an area of $3.6cm^2$, the 6-channel neck coil offered an average SNR of 21.08, while the commercial coil offered lower performances of only 11.81.
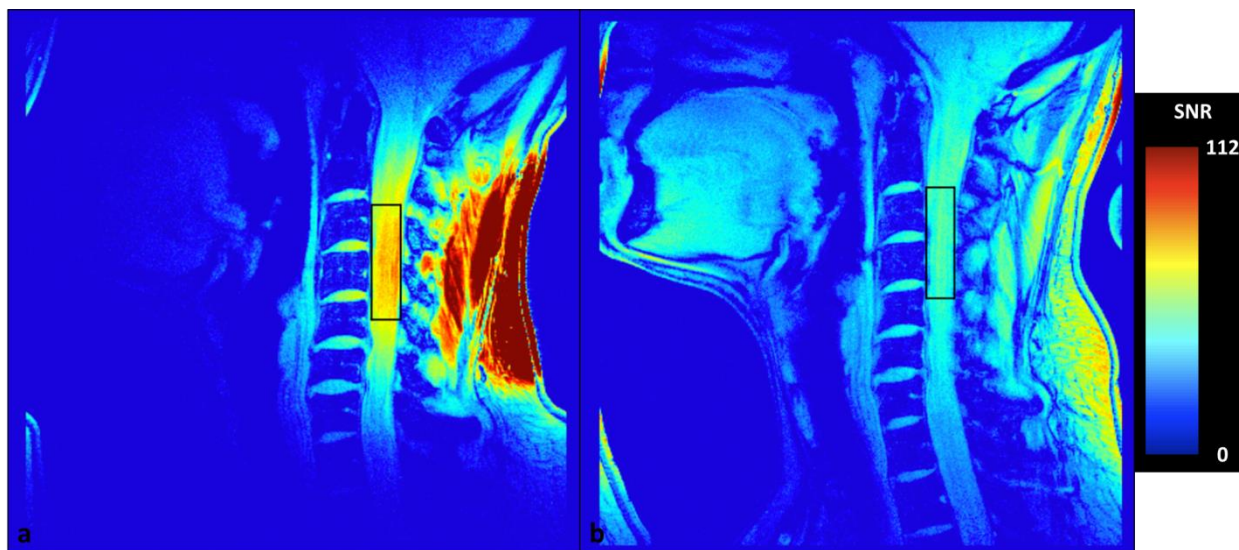
Figure 3.45- SNR map of the human subject phantom obtained using the custom-built coil (a) and the commercial coil (b).

3.3.3 FLASH images

The imaging tests performed *in vivo* MRI allowed to obtain images using FLASH sequence. The acquisition parameters detailed in the methods and materials section of this thesis.
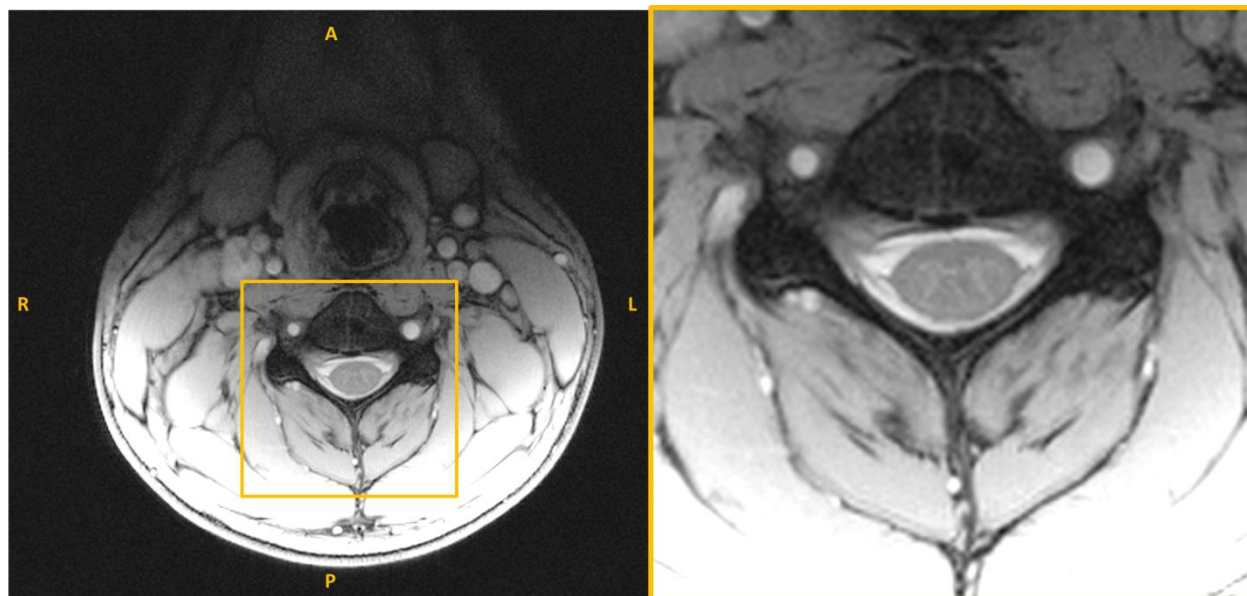
Figure 3.46- FLASH image of the spinal cord obtained using the custom built coil with acceleration 2.
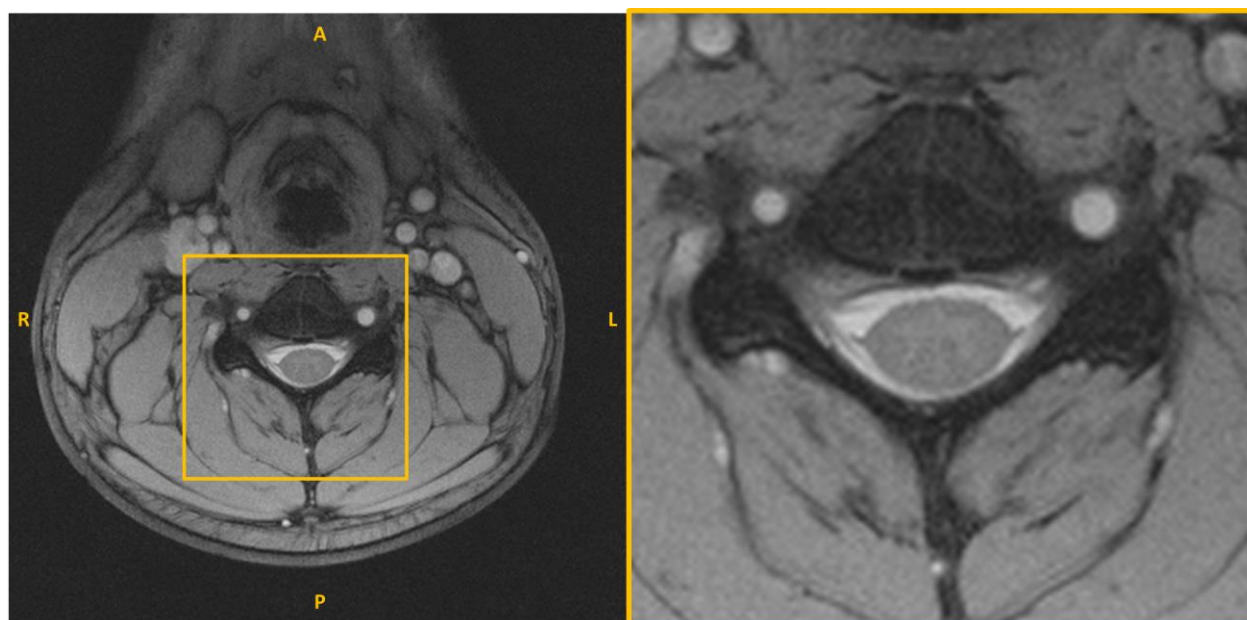
Figure 3.47- FLASH image of the spinal cord obtained using the commercial coil with acceleration 2.

A second set of images was acquired to illustrate the acceleration performances offered by the custom built coil. The acquisition parameters were detailed in the methods and materials section of this thesis.
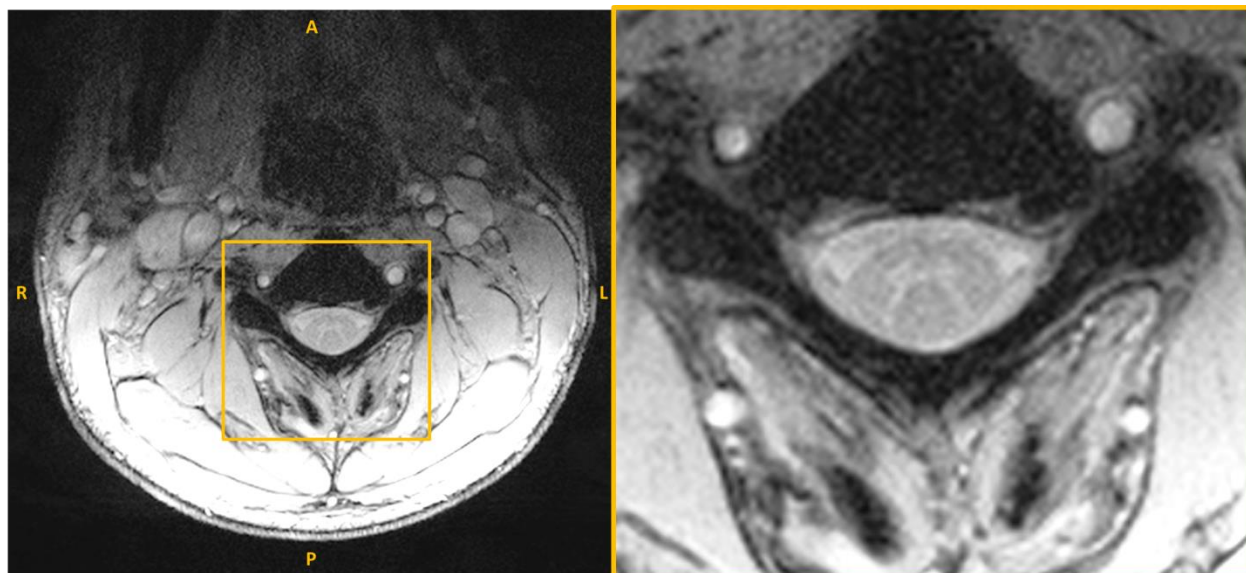
Figure 3.48- FLASH image of the spinal cord obtained using the custom built coil with acceleration 3.
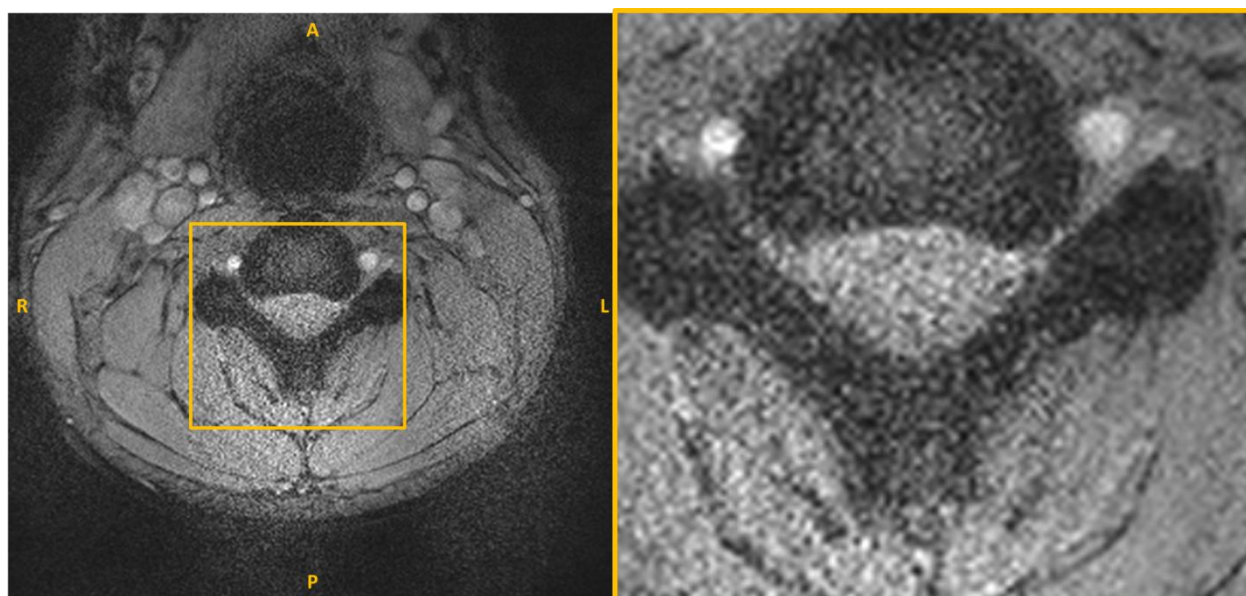
Figure 3.49- FLASH image of the spinal cord obtained using the commercial coil with acceleration 3.

Dynamic spinal cord imaging

Another set of cine images were acquired to evaluate the movement of the spinal cord during a cardiac cycle. The acquisition parameters were detailed in the methods and materials section of this thesis. The video is available at the following address:

 https://www.dropbox.com/s/dxfs3kngx7h34d4/Dev_Sc_Cine_ax.mov?dl=0
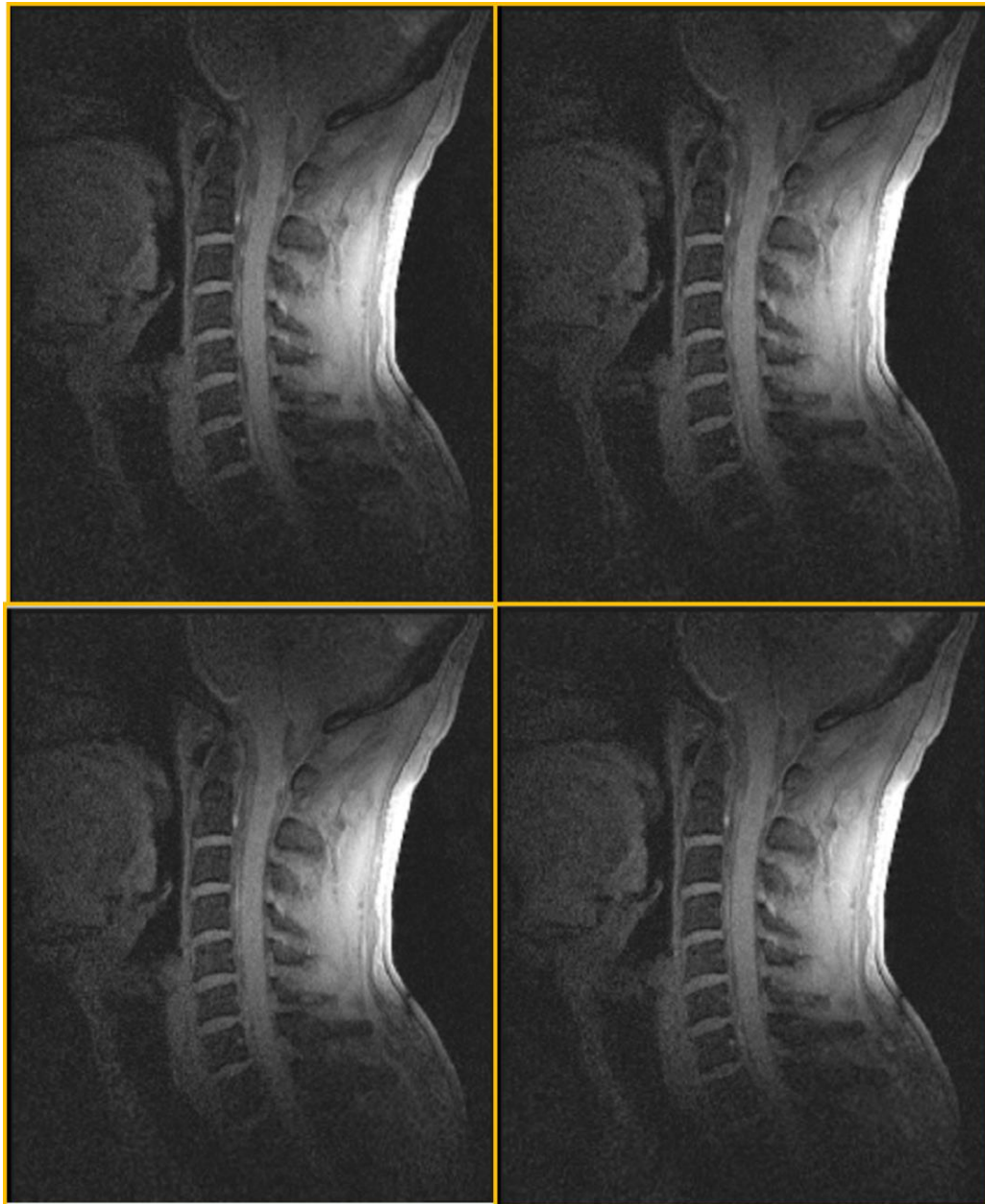
Figure 3.50- Cine images of the spinal cord obtained using the custom built coil.

CHAPTER 4   DISCUSSION

In this thesis is presented the design, construction and characterization of a highly sensitive   6-channel receive-only arrays coil for highly accelerated cervical imaging of the spinal cord at 3T. The characterization of the coil was made using electromagnetic simulations for evaluating the magnetic field sensitivity profile and the theoretical SNR. Furthermore, the coil performance was evaluated on the bench regarding the tuning frequency, impedance matching, active detuning, inductive decoupling and preamplifier decoupling. Finally, the coil was validated on a human subject by computing SNR maps and noise covariance matrix.

The developed electromagnetic simulations framework offered similar results to the ones obtained using FEKO or MRI images. The simulation framework has a user-friendly interface, offering a large degree of freedom of parameter definition. It offers fast characterization of various coil geometries, while computation time is dependent on the precision degree in the spatial volume. Despite the fact that the framework offered good results, a series of limitations have to be outlined. One of the most important limitations is that the magnetic field computation does not consider the wave propagation phenomenon. The simplified method of computation is accepted for low field application, due to the corresponding resonant frequency (Wright & Wald, 1997). In addition, the steady current used for computing the generated magnetic field is a simplified situation of current distribution in a conductor. The skin effect contribution to the resultant current distribution is ignored. Moreover, the inductive coupling between adjacent loops is ignored, ideal preamplifier decoupling being considered.

The simulated configurations were inspired from the commercial designs for coils dedicated for the cervical region of the spinal cord. From the B1 field sensitivity profile, configuration with 2 channels offered the best magnetic field penetration at the level 50mm (Figure 3.2). The most important aspect of an RF coil is the provided SNR in the ROI. Further simulations were focused on the assessment of SNR of the proposed configurations. Consequently, even though the 2-channel configuration offered the best field penetration, the 6-channel configuration was chosen due to the fact it provided higher SNR in the ROI (Figure 3.4).

The electromagnetic simulation framework was validated using similar configurations in FEKO. The MATLAB scripts underestimated the electromagnetic field intensity in average with 9% compared to the FEKO results. The developed electromagnetic simulations were preferred over FEKO simulations due to difficulty of decoupling adjacent loops. Due to the fact that the FEKO

simulations are more complex, current distribution, inductive coupling and wave propagation phenomenon are taken into account.

The mechanical design was focused on offering a suitable fixation on the patient table and a high degree of comfort for the patient. Even though the neck former is smaller than the neck former found in other commercial coils, it was large enough to accommodate a diverse population. The thickness of the coil housing was selected in order to offer strength to the whole structure and to support the patient. The coil housing was well integrated with the patient table and the scanner plug interface. A series of mechanical tests were performed to determine the optimal length for the connection cable.

The electronic circuit design was initially simulated on PSPICE and ADS using an accurate model of a loop. The values obtained for the discrete electronic components were similar for the two electronic design programs. Moreover, the components used in the implementation of the 6-channel coil array had the impedance obtained through simulations. Using surface mounted components and small size preamplifiers, the size of PCBs was reduced. The frequency response obtained from simulations was validated by bench measurement. Due to the geometrical arrangement of the loops, the preamplifier positioning becomes more challenging. The positioning of the preamplifiers has impact on the overall SNR at the optimal noise figure and preamplifier decoupling. Considering all the previous presented aspects, the degree of freedom of preamplifier positioning is limited by the optimal cable routing. Therefore, the preamplifiers were placed in the middle of the loop at a distance of 2cm from the coil former. The output coaxial cable of each channel needs to be carefully routed not to pass near the other's preamplifier input in order to avoid feedback loops. The preamplifier needs to have an adequate mechanical fixation to avoid faulty contacts. Moreover, the DC wires used for PIN diode controlling need to be well fixed and twisted around the output coaxial cables to avoid the Lorentz forces caused by high B_0 fields and high gradients.

The geometrical decoupling between neighboring loops was a challenging stage in building and assembling the 6-channel neck coil. In order to facilitate the adjustability of the overlapping between elements, the loop had bend bridges allowing the crossing of the wires. The geometrical decoupling was carefully adjusted. The average decoupling level was within the performance targets defined at the beginning of the project.

The proposed active detuning and preamplifier decoupling response was lower for bench measurement than for the electronic circuit simulations. This aspect is justified by the fact that the electronic circuit simulation does not model all the losses within the circuit. In addition, some measurements obtained on the bench illustrate the coupling between adjacent elements; especially the elements located in the middle of the array are the most affected. The output preamplifier signals prove that there is no crosstalk between various channels.

The use of water phantom is required when performing all the bench measurements, in order to simulate the loading conditions of the human subject. The water phantom mimicked the average proprieties of human tissue.

The initial validation of the 6-channel receive-only coil in the MRI was made using the water phantom. The custom-built coil was compared to the commercially available coil from the SNR point of view. The computed SNR maps illustrate that the commercial coil offers a larger FOV, but the penetration is not very deep. On the other hand, the custom built coil had a reduced FOV, but a better penetration in the ROI. The SNR obtained using the custom built coil was 30% higher than for the commercial coil. Analyzing the noise covariance matrix, we can conclude that the noise covariance between adjacent elements of the built coil is lower than 0.4.

Human subjects were scanned once the coil was validated with the water phantom. According to the positioning of the patient on the table, the ROI was centered on the C4 vertebral level of the spinal cord. The gradient echo sequences are widely used in the clinical and research applications. A qualitative comparison between the custom built coil and the commercial coil was based on the computation of SNR maps. Apart from the dynamic contrast of the image, the SNR is an important characteristic of medical images. Fine anatomic structures can be depicted if the level of SNR is adequate. The computed SNR map in sagittal plane for the 6-channel neck coil array provided almost two times more SNR than the commercial one in an area of $3.6cm^2$.

In addition, a second set of data was acquired for the acceleration capabilities assessment. An initial test was made using an acceleration of 2 for FLASH imaging. The 6-channel coil array offered good contrast of the spinal cord in axial cut for a plane centered on the C4 level. The magnetic field profile of the custom built coil is not homogeneous, being much brighter in the posterior region. The reduced voxel dimensions (0.5x0.5x5mm) and the higher SNR provided by the custom coil enabled the differentiation between different structures of the spinal cord (white

matter, grey matter, cerebrospinal fluid). In comparison, the magnetic field profile of the commercial coil was homogeneous within the entire FOV.

The second evaluation of the acceleration capabilities was performed using a FLASH sequence with an acceleration of 3. As explained in a previous section (literature review) the acceleration factor of an RF coil depends on its geometry and on the number of available channels. The commercial coil has 4 physical channels which are combined in 2 channels on the scanner interface. On the other hand, the custom built coil has 6 independent channels, which can be used to achieve higher acceleration without an important impact on the image quality. Comparing the images of the C4 vertebral level of the spinal cord in axial plane acquired with the two coils, the custom built coil offers better results. The images obtained using commercial coils illustrate reconstruction artifacts due to high degree of under-sampling of the k-space.

The last set of data obtained using the dynamic imaging sequence illustrates the movement of the spinal cord between different stages of a cardiac cycle. The six-channel neck coil array was used due to its high SNR in the spinal cord. The analysis of the image set with the cardiac cycle illustrates that the spinal cord moves within the vertebral cavity. The contrast of the image facilitates the depiction of the spinal cord and the cerebrospinal fluid.

CHAPTER 5   CONCLUSION AND RECOMMENDATIONS

The current project was focused on the design and construction of a six channel coil array for the imaging of the cervical region of the human spinal cord at 3T. The geometry of the coils and their positioning around the ROI was determined using electromagnetic simulations. The electromagnetic simulation code is available online: https://github.com/neuropoly/coil_simulation

The proposed coil offers an average improvement in SNR by a factor of 2, which enables higher spatial resolution. Therefore, the depiction of small pathologies such as small lesions in multiple sclerosis or the movement of the spinal cord is enhanced. Moreover, the optimized geometry enables to use aggressive acceleration factors (e.g., 3) and therefore reduce acquisition time significantly.

Future perspectives involve high resolution anatomical imaging (0.3mm in-plane), fMRI, DTI and spectroscopy studies for characterizing the metabolism of different tissues present in the spinal cord and lower brain sections. The electromagnetic simulations framework can be used to determine a higher density coil array for a better coverage of the spinal cord from the lower brain level to thoracic or lumbar level of the spinal cord.

BIBLIOGRAPHY

Ackerman, J. J. H., Grove, T. H., Wong, G. G., Gadian, D. G., & Radda, G. K. (1980). Mapping of metabolites in whole animals by 31P NMR using surface coils. *Nature, 283*(5743), 167-170.

Advanced MRI section, L., NINDS, National Institutes of Health. (2015). Dielectric phantom recipe generator. from https://amri.ninds.nih.gov/cgi-bin/phantomrecipe

Anke Henning, W. K., Alexander Fuchs, Alexander Raaijmakers, Johanna J. Bluemink, Erin L. MacMillan, Cornelius A.T. van den Berg, Peter Luijten, Peter Boesiger, Dennis W.J. Klomp. (2012). *1H MRS in the human spinal cord at 7T using a combined RF shimming and travelling wave transmit approach.* Paper presented at the Proceedings International Society for Magnetic Resonance in Medicine 20.

Ballinger, J. R. (1996). Spin Echo Sequence. from http://www.mritutor.org/mritutor/spinecho.htm

Bing, W., Chunsheng, W., Krug, R., Kelley, D. A., Duan, X., Yong, P., . . . Xiaoliang, Z. (2010). 7T Human Spine Imaging Arrays With Adjustable Inductive Decoupling. *Biomedical Engineering, IEEE Transactions on, 57*(2), 397-403. doi: 10.1109/TBME.2009.2030170

Bodurka, J., Ledden, P., & Bandettini, P. (2008). *SENSE optimized sixteen element receive array for cervical spinal cord imaging at 3T.* Paper presented at the Proceedings of the 16th Annual Meeting of ISMRM, Toronto, Canada.

Cohen-Adad, J. (2014). *Cours GBM3318 - Principe d'imagerie biomédicale*. Montréal, Canada: École Polytechnique de Montréal.

Cohen-Adad, J., Mareyam, A., Keil, B., Polimeni, J. R., & Wald, L. L. (2011a). 32-Channel RF coil optimized for brain and cervical spinal cord at 3 T. *Magnetic Resonance in Medicine, 66*(4), 1198-1208. doi: 10.1002/mrm.22906

Cohen-Adad, J., Mareyam, A., Keil, B., Polimeni, J. R., & Wald, L. L. (2011b). 32-channel RF coil optimized for brain and cervical spinal cord at 3 T. *Magn Reson Med, 66*(4), 1198-1208. doi: 10.1002/mrm.22906

Cohen-Adad, J., & Wheeler-Kingshott, C. (2014). *Quantitative MRI of the spinal cord*: Academic Press.

Constantinides, C. D., Westgate, C. R., O'Dell, W. G., Zerhouni, E. A., & McVeigh, E. R. (1995). A Phased Array Coil for Human Cardiac Imaging. *Magn Reson Med, 34*(1), 92-98.

Damadian, R. V. (1972). USA 3789832 Patent No.

De Zanche, N., Massner, J. A., Leussler, C., & Pruessmann, K. P. (2008). Modular design of receiver coil arrays. *NMR Biomed, 21*(6), 644-654. doi: 10.1002/nbm.1237

Duan, Q., Duyn, J. H., Gudino, N., de Zwart, J. A., van Gelderen, P., Sodickson, D. K., & Brown, R. (2014). Characterization of a dielectric phantom for high-field magnetic resonance imaging applications. *Medical Physics, 41*(10), 102303. doi: doi:http://dx.doi.org/10.1118/1.4895823

Edelstein, W. A., Glover, G. H., Hardy, C. J., & Redington, R. W. (1986). The intrinsic signal-to-noise ratio in NMR imaging. *Magnetic Resonance in Medicine, 3*(4), 604-618. doi: 10.1002/mrm.1910030413

Ellis, B. (2006). Electronic Circuits, Fundamentals and Applications. *Soldering & Surface Mount Technology, 18*(4).

F. Wiesinger, N. D. Z., K. P. Pruessmann. (2005). *Approaching Ultimate SNR with Finite Coil Arrays.* Paper presented at the Proceedings International Society for Magnetic Resonance in Medicine 13.

Fujita, H. (2007). New Horizons in MR Technology: RF Coil Designs and Trends. *Magnetic Resonance in Medical Sciences, 6*(1), 29-42. doi: 10.2463/mrms.6.29

Gray, H., Goss, C. M., & Alvarado, D. M. (1973). *Anatomy of the human body*: Lea & Febiger Philadelphia.

Griswold, M. A., Jakob, P. M., Heidemann, R. M., Nittka, M., Jellus, V., Wang, J., . . . Haase, A. (2002). Generalized autocalibrating partially parallel acquisitions (GRAPPA). *Magnetic Resonance in Medicine, 47*(6), 1202-1210.

Griswold, M. A., Jakob, P. M., Nittka, M., Goldfarb, J. W., & Haase, A. (2000). Partially parallel imaging with localized sensitivities (PILS). *Magnetic Resonance in Medicine, 44*(4), 602-609.

Hagmann, P., Jonasson, L., Maeder, P., Thiran, J.-P., Wedeen, V. J., & Meuli, R. (2006). Understanding Diffusion MR Imaging Techniques: From Scalar Diffusion-weighted Imaging to Diffusion Tensor Imaging and Beyond 1. *Radiographics, 26*(suppl_1), S205-S223.

Hayes, C. E., Dietz, M. J., King, B. F., & Ehman, R. L. (1992). Pelvic imaging with phased-array coils: Quantitative assessment of signal-to-noise ratio improvement. *Journal of Magnetic Resonance Imaging, 2*(3), 321-326. doi: 10.1002/jmri.1880020312

Hayes, C. E., Hattes, N., & Roemer, P. B. (1991). Volume imaging with MR phased arrays. *Magnetic Resonance in Medicine, 18*(2), 309-319. doi: 10.1002/mrm.1910180206

Hayes, C. E., Mathis, C. M., & Yuan, C. (1996). Surface coil phased arrays for high-resolution imaging of the carotid arteries. *Journal of Magnetic Resonance Imaging, 6*(1), 109-112. doi: 10.1002/jmri.1880060121

Hoult, D., & Kolansky, G. (2010). *A magnetic-field-tolerant low-noise SiGe pre-amplifier and T/R switch.* Paper presented at the Proceedings of the 18th Annual Meeting of ISMRM.

Hoult, D. I. (2000). The principle of reciprocity in signal strength calculations—A mathematical guide. *Concepts in Magnetic Resonance, 12*(4), 173-187. doi: 10.1002/1099-0534(2000)12:4<173::AID-CMR1>3.0.CO;2-Q

Hoult, D. I., & Richards, R. E. (1976). The signal-to-noise ratio of the nuclear magnetic resonance experiment. *J Magn Reson, 24*(1), 71-85. doi: doi:10.1016/0022-2364(76)90233-X

Hoult, D. I., & Richards, R. E. (2011). The signal-to-noise ratio of the nuclear magnetic resonance experiment. *J Magn Reson, 213*(2), 329-343. doi: http://dx.doi.org/10.1016/j.jmr.2011.09.018

Jianmin, W., Reykowski, A., & Dickas, J. (1995). Calculation of the signal-to-noise ratio for simple surface coils and arrays of coils [magnetic resonance imaging]. *Biomedical Engineering, IEEE Transactions on, 42*(9), 908-917. doi: 10.1109/10.412657

Keil, B. (2013). *Construction of receive arrays: Weekend Educational Course.* Paper presented at the Int. Society Magnetic Resonance Medicine 21, Salt Lake City, Utah, USA.

Keil, B., Alagappan, V., Mareyam, A., McNab, J. A., Fujimoto, K., Tountcheva, V., . . . Wald, L. L. (2011). Size-optimized 32-channel brain arrays for 3 T pediatric imaging. *Magnetic Resonance in Medicine, 66*(6), 1777-1787. doi: 10.1002/mrm.22961

Keil, B., Biber, S., Rehner, R., Tountcheva, V., Wohlfarth, K., Hoecht, P., . . . Wald, L. (2011). *A 64-channel array coil for 3T head/neck/C-spine imaging.* Paper presented at the Proc. Intl. Soc. Mag. Reson. Med.

Keil, B., Blau, J. N., Biber, S., Hoecht, P., Tountcheva, V., Setsompop, K., . . . Wald, L. L. (2013). A 64-channel 3T array coil for accelerated brain MRI. *Magnetic Resonance in Medicine, 70*(1), 248-258. doi: 10.1002/mrm.24427

Keil, B., & Wald, L. L. (2013). Massively Parallel MRI Detector Arrays. *Journal of magnetic resonance (San Diego, Calif. : 1997), 229*, 75-89. doi: 10.1016/j.jmr.2013.02.001

Keil, B., Wiggins, G. C., Triantafyllou, C., Wald, L. L., Meise, F. M., Schreiber, L. M., . . . Heverhagen, J. T. (2011). A 20-channel receive-only mouse array coil for a 3 T clinical MRI system. *Magnetic Resonance in Medicine, 66*(2), 582-593. doi: 10.1002/mrm.22791

Kellman, P., & McVeigh, E. R. (2005). Image reconstruction in SNR units: A general method for SNR measurement†. *Magnetic Resonance in Medicine, 54*(6), 1439-1447. doi: 10.1002/mrm.20713

Kraff, O., Bitz, A. K., Kruszona, S., Orzada, S., Schaefer, L. C., Theysohn, J. M., . . . Quick, H. H. (2009). An eight-channel phased array RF coil for spine MR imaging at 7 T. *Investigative radiology, 44*(11), 734-740.

Kumar, A., & Bottomley, P. A. (2006). Optimizing the intrinsic signal-to-noise ratio of MRI strip detectors. *Magnetic Resonance in Medicine, 56*(1), 157-166. doi: 10.1002/mrm.20915

Kumar, A., Edelstein, W. A., & Bottomley, P. A. (2009). Noise figure limits for circular loop MR coils. *Magnetic Resonance in Medicine, 61*(5), 1201-1209. doi: 10.1002/mrm.21948

Kyle M. Gilbert, & Menon, R. S. (2015). *Construction of receive arrays: a four channel rat coil for 9.4T.* Paper presented at the Int. Society Magnetic Resonance Medicine 23, Toronto,Canada.

Lagore, R., Roberts, B., Fallone, B., & De Zanche, N. (2011). *Comparison of three preamplifier technologies: variation of input impedance and noise figure with B0 field strength.* Paper presented at the Proceedings of the 19th Annual Meeting of ISMRM.

Lehner, G. (2008). *Electromagnetic Field Theory for Engineers and Physicists.* Berlin; London: Springer Berlin Heidelberg.

Mispelter, J., Lupu, M., & Briguet, A. (2006). *NMR probeheads for biophysical and biomedical experiments : theoretical principles & practical guidelines.* London: Imperial College Press ;.

Neiman, M. S. (1943). The Principle of Reciprocity in Antenna Theory. *Proceedings of the IRE, 31*(12), 666-671. doi: 10.1109/JRPROC.1943.233683

Nguyen, A. K. D., Simard-Meilleur, A. A., Berthiaume, C., Godbout, R., & Mottron, L. (2012). Head Circumference in Canadian Male Adults: Development of a Normalized Chart. *International Journal of Morphology, 30*, 1474-1480.

Ocali, O., & Atalar, E. (1998). Ultimate intrinsic signal-to-noise ratio in MRI. *Magnetic Resonance in Medicine, 39*(3), 462-473. doi: 10.1002/mrm.1910390317

Ohliger, M. A., Grant, A. K., & Sodickson, D. K. (2003). Ultimate intrinsic signal-to-noise ratio for parallel MRI: Electromagnetic field considerations. *Magnetic Resonance in Medicine, 50*(5), 1018-1030.

Ohliger, M. A., & Sodickson, D. K. (2006). An introduction to coil array design for parallel MRI. *NMR in Biomedicine, 19*(3), 300-315. doi: 10.1002/nbm.1046

Possanzini, C., & Boutelje, M. (2008). *Influence of magnetic field on preamplifiers using GaAs FET technology.* Paper presented at the Proceedings of the 16th Annual Meeting of ISMRM, Toronto, Canada.

Pozar, D. M. (2009). *Microwave engineering*: John Wiley & Sons.

Prince, J. L., & Links, J. M. (2006). *Medical imaging signals and systems*. Upper Saddle River, N.J.: Pearson Prentice Hall.

Pruessmann, K. P., Weiger, M., Scheidegger, M. B., & Boesiger, P. (1999). SENSE: sensitivity encoding for fast MRI. *Magnetic Resonance in Medicine, 42*(5), 952-962.

Reykowski, A., Hemmerlein, M., & Fischer, H. (2005). *16 Channel Head/Neck Matrix Coils for 3 Tesla.* Paper presented at the Proceedings of the thirteenth annual meeting of the ISMRM. Miami.

Riccardo Lattanzi, P., Ryan Brown, P., & Kaveh Vahedipour, P. (2015). *G16.4427 - Practical Magnetic Resonance Imaging I*: Center for Advanced Imaging Innovation and Research.

Roemer, P. B., Edelstein, W. A., Hayes, C. E., Souza, S. P., & Mueller, O. M. (1990). The NMR phased array. *Magnetic Resonance in Medicine, 16*(2), 192-225. doi: 10.1002/mrm.1910160203

Schoenberg, S. O., Dietrich, O., & Reiser, M. (2007). *Parallel imaging in clinical MR applications*. Berlin ; New York: Springer.

Sherrow, V. (2007). Medical imaging (pp. 127). New York: Marshall Cavendish Benchmark.

Sigmund, E. E., Suero, G. A., Hu, C., McGorty, K., Sodickson, D. K., Wiggins, G. C., & Helpern, J. A. (2012). High-resolution human cervical spinal cord imaging at 7 T. *NMR in Biomedicine, 25*(7), 891-899. doi: 10.1002/nbm.1809

Smythe, W. R., & Smythe, W. R. (1950). *Static and dynamic electricity* (Vol. 3): McGraw-Hill New York.

Sodickson, D. K., & Manning, W. J. (1997). Simultaneous acquisition of spatial harmonics (SMASH): Fast imaging with radiofrequency coil arrays. *Magnetic Resonance in Medicine, 38*(4), 591-603. doi: 10.1002/mrm.1910380414

Wald, L. L., Carvajal, L., Moyher, S. E., Nelson, S. J., Grant, P. E., Barkovich, A. J., & Vigneron, D. B. (1995). Phased array detectors and an automated intensity-correction algorithm for high-resolution MR imaging of the human brain. *Magn Reson Med, 34*(3), 433-439.

Weishaupt, D., Kochli, V. D., & Marincek, B. (2006). *How does MRI work? : an introduction to the physics and function of magnetic resonance imaging* (2nd ed.). Berlin ; New York: Springer.

Wiesinger, F., Boesiger, P., & Pruessmann, K. P. (2004). Electrodynamics and ultimate SNR in parallel MR imaging. *Magnetic Resonance in Medicine, 52*(2), 376-390. doi: 10.1002/mrm.20183

Wiggins, G. C., Triantafyllou, C., Potthast, A., Reykowski, A., Nittka, M., & Wald, L. L. (2006). 32-channel 3 Tesla receive-only phased-array head coil with soccer-ball element geometry. *Magnetic Resonance in Medicine, 56*(1), 216-223. doi: 10.1002/mrm.20925

Wright, S. M., & Wald, L. L. (1997). Theory and application of array coils in MR spectroscopy. *NMR in Biomedicine, 10*(8), 394-410. doi: 10.1002/(SICI)1099-1492(199712)10:8<394::AID-NBM494>3.0.CO;2-0

Zhao, W., Cohen-Adad, J., Polimeni, J. R., Keil, B., Guerin, B., Setsompop, K., . . . Wald, L. L. (2014). Nineteen-channel receive array and four-channel transmit array coil for cervical spinal cord imaging at 7T. *Magnetic Resonance in Medicine, 72*(1), 291-300. doi: 10.1002/mrm.24911